MSc Thesis

Extending the velocity range of Robotic Volumetric PIV

Design and application of a multi-Δt approach

E. Saredi

Aerodynamics

Faculty of Aerospace Engineering

TU Delft

Delft University of Technology

Extending the velocity range of Robotic Volumetric PIV

Design and application of a multi Δt approach

Master of Science Thesis

For obtaining the degree of Master of Science in Aerospace Engineering
at Delft University of Technology

E. Saredi

May 18,2018

TU Delft Delft University of Technology

DELFT UNIVERSITY OF TECHNOLOGY
DEPARTMENT OF AERODYNAMICS

The undersigned hereby certify that they have read and recommend to the Faculty of Aerospace Engineering for acceptance for the thesis entitled **"Extending the velocity range of Robotic Volumetric PIV"** by **E. Saredi** in fulfillment of the requirements for the degree of **Master of Science**.

Supervisors:

Dr. Andrea Sciacchitano

Prof. Dr. Fulvio Scarano

Dr.Ir. Bas van Oudheusden

Dr. Daniele Ragni

An electronic version of this thesis is available at `https://repository.tudelft.nl/`.
The front page image is taken and modified from:
http://www.osmvalue.com/wp-content/uploads/2016/10/competizione.jpg.

PREFACE

After one year, my thesis project has finally come to an end. I am aware that this achievement would not have been reached without the help and the support of some of the people I crossed the path with, and for this reason, I really would like to thank them.

First of all, I would like to thank my daily supervisor *Dr. Andrea Sciacchitano*. I will never forget the guidance he provided me, the availability whenever I needed and the patience for my constant delay to every meeting. *Prof. Fulvio Scarano* is the second person I really have to thank. His enthusiasm, his long-term vision and his experience have been a source of inspiration for me. *Jan Schneiders* has been another excellent example for me during this year. The discussions with him have always been really constructive. Several of the best ideas, in my debatable point of view, came during or just after meetings with these mentioned people.

This project would not have seen the light without the collaboration and support of the company where I made the internship during my master, RENAULT SPORT RACING F1. I would like to thank them for the opportunity and for the trust they gave me. My most profound gratitude goes to *Dr. Robbie Stevens*, my supervisor and my mentor when I was there. I will not forget the support you gave me during those days, days in which I really learnt a lot, both on a professional side and from a personal perspective.

As every experimentalist knows, here I am giving myself the name of "experimentalist", a bit too much probably, any good experiment is never achieved without a good team working. For this reason, I really have to thank the people of the Aerodynamics department who helped me during these months: *Frits Donker Duyvis*, *Peter Duyndam*, *Dennis Bruikman*, *Nico van Beek* and *Colette Russo*.

An excellent thanks must go to *Daniele (Giggi)*, *Luigi (Giggi)* for their help during my entire master thesis. I learnt a lot from them, and I will always look at them as an example that has to be followed. But only one thing, Luigi (Giggi), please don't use anymore the "coppola", you are still young.

At this point, it is impossible not to thank as well the "Basement Inhabitants" that made this long period definitely not boring: *Arun*, *Blanquita* and all the others.

Another important mention has to be done for the friends I met in Delft, for the moment they gave me and for their patience for my delays. *Nanna*, *Cami*, *Davide*, *Fe*, *Fede*, *Mitrottino*, *Gre*, *Lu*, *Luchetto*, *Teone*, *Oltino*, *Rego*, *Giulia*, *Umbe*, *Ans* and *Tommy*. Tutti loro hanno sicuramente contribuito a questo traguardo, rendendo indimenticabile la mia esperienza in Olanda, missione tutt'altro che facile.

Among them, I excluded two guys that made my permanence in Delft even more special because they merit specific mention. *Baudinho* and *Perrons*, I will never forget our "conquilinanza", the dinners (not prepared by me) together, the nights spent talking about the robot that steals work to humans or trying to understand how to become billionaires. Thank you again. I also must mention that thanks to the year passed together, I met *Bea*, that bore and supported me in the last months, and hopefully for a long time.

But if my life has been centred mainly in Delft in the last three years, I cannot avoid to the mention and thank the people in Italy that were always present at my return: *Carletta*, *Favucchio*, *G*, *Garlux*, *Giulia*, *Leonida*, *Oras*, *Sguozzolo* and *Vitti*.

Last but not least, I owe a special thanks to the old two people that I usually call my parents. Without their support, patience and trust, this achievement would not have been possible.

Finally, I dedicate this work to the man you showed me what dignity and seriousness are, *Giovanni*. Even if too late, this is for you.

E. Saredi
Delft, May 2018

ABSTRACT

Car industry and motorsport development nowadays strongly rely on wind tunnel testing. As the literature survey shows, in order to fully understand the characteristics of the flow around a car, large-scale and volumetric flow field measurements are required. For its features, PIV can be pointed as a useful technique for automotive wind tunnels. However, its use in an automotive wind tunnel is strongly conditioned by the industrial environment itself, which requires particular efforts for what concerns safety and economic aspects.

The advent of Robotic Volumetric PIV has permitted the measurement of time-averaged properties of large-scale complex aerodynamic flows by the combination of coaxial volumetric velocimetry and robotics. Firstly, the use of Helium Filled Soap Bubbles as seeding permits to enlarge the measurement volume due to their higher scattering capability. Furthermore, the compactness of the coaxial velocimetry probe together with the robotic actuation allows to measure large-scale volumes, partitioning the entire volume and reconstructing the time-averaged flow filed from multiple PIV acquisitions. Since its presentation, Robotic Volumetric PIV has been used to investigate low velocities flows, with free-stream values ranging between 2 m/s and 14 m/s. More specifically, 15 m/s can be considered the largest velocity that can be analysed with the state-of-the-art of the system due to its hardware limitations in the maximum acquisition frequency. For this reason, to meet the requirements in terms of flow velocities proper of industrial environments, the range of analysable velocities has to be extended.

To address the identified requirement of high-speed volumetric measurements, a new acquisition technique has been designed and proposed. Even if a standard double-pulse strategy can measure high-speed flows due to the short time that can elapse between the two subsequent pulses, in order to increase the accuracy of the final results, a two-Δt method is proposed. Firstly, a predictor is built using a Double-Pulse, Double-Frame acquisition with a short pulse separation time Δt_1. Afterwards, the predictor is used to allow the stretching of the second pulse separation time Δt_2 without encountering errors given by the false pairing that would be present due to the longer displacement of the particles.

To test the performance of the new method, the near wake of a 50% replica of the Ahmed body with a 25° slant angle has been studied through an experimental campaign in the Open Jet Facility (OJF) of TU Delft. Firstly, a measurement at 12 m/s has been performed in order to be able to assess the performances of the proposed method w.r.t. the time-resolved acquisition strategy and the DP standard -DF approach. Afterwards, an airspeed of 20 m/s has been considered, in order to demonstrate the capability of the new technique of extending the velocity range of Robotic

Volumetric PIV.

The conducted measurements demonstrate the possibility of extending the velocity range of the Robotic Voluemtric PIV system with the proposed method. However, this is achieved at the expense of a lower accuracy, due to the lack of temporal information, and a longer measurement time, given by the necessity of multiple acquisitions.

CONTENTS

List of Figures

NOMENCLATURE

Acronyms

CFD Computational Fluid Dynamics

CMOS Complementary Metal–Oxide–Semiconductor

CVV Coaxial Volumetric Velocimetry

DP-DF Double-Pulse, Double-Frame

DVR Dynamic Spatial Range

DVR Dynamic Velocity Range

EA Ensemble-Average

FOV Field of View

FSU Fluid Supply Unit

HFSB Helium Filled Soap Bubbles

IPR Iterative Particle Reconstruction

LDA Laser Doppler Anemometry

NN Nearest-Neighbor

OJF Open Jet Facility

PD Particle Detection

PIV Particle Image Velocimetry

PP Particle Pairing

PTU Programmable Time Unit

PTV Particle Tracking Velocimetry

SAC	Sliding Average Correlation
STB	Shake the Box
TR	Time-Resolved
VAWT	Vertical Axis Wind Turbine

Symbols

β	Tomographic aperture	[°]
$\Delta_{p_{max}}$	STB maximum allowed particle shift	[vox]
Δ_{px}	Sensor pitch	[μm]
Δt	Pulse separation time	[s]
Δt^*	DVR gain	[-]
δ_u	Maximum absolute error	[m/s]
ΔX	Displacement in the image plane	[m]
Δ_x	Edge length of the EA volume	[m]
Δ_x	Particle displacement in real space	[m]
ε_Δ	STB allowed triangulation error	[px]
ε_u	Relative velocity uncertainty	[m/s]
ε_x	Relative position uncertainty	[m]
$\varepsilon_{\overline{u}}$	Uncertainty on the average velocity	[m/s]
λ	Light wavelight	[m]
μ	Dynamic viscosity	[kg/($s \cdot m$)]
μ_{max}	Peak friction coefficient of a tyre	[kg/($s \cdot m$)]
ν	Cinematic viscosity	[m^2/s]
ω	Vorticity	[s^{-1}]
ω_x	Streamwise vorticity	[s^{-1}]
φ	Slant angle	[°]
ρ	Material density	[kg/m^3]

$\sigma_{\Delta x}$	Positioning uncertainty	[m]
σ_u	Velocity standard deviation	[m/s]
A_F	Seeding Rake frontal area	$[m^2]$
C_{HFSB}	HFSB seeding concentration	$[bubbles/cm^3]$
C_z	Aerodynamic downforce	[N]
d_p	Particle diameter	[mm]
d_τ	Image particle diameter	[px]
d_z	Reconstructed particle diameter	[m]
f	Camera acquisition frequency	[Hz]
f_{max}	Maximum acquisition frequency	[Hz]
f_ν	Characteristic vortices frequency	[Hz]
$f_\#$	F-stop number	[-]
g	Acceleration due to gravity	$[m/s^2]$
H	Reference length, height of the Ahmed body	[m]
k	Coverage factor	[-]
k_n	Weight used in EA	[-]
l_x	Characteristic dimension of the flow	[m]
M	Magnification factor	[-]
M	Mass associated with the tyre	[kg]
N	Number of samples	[-]
N_{bs}	Number of bubbles released per second	$[bubbles/s]$
N_w	Number of uncorelated samples	[-]
ppp	Particle per pixel	[-]
$\overline{r}$	Mean particle distance	[m]
Re	Reynolds number	[-]
St	Strouhal number	[-]

T	Acquisition period	[s]
$\overline{u}$	Mean of the velocity **u**	$[m/s]$
U_∞	Free-stream velocity	$[m/s]$
U_s	Slip velocity	[m/s]
$\dot{V}_s$	Particle volumetric flow rate	$[cm^3/s]$
$\overline{X}_{CT}$	Vector between XYZ_{Tool} and XYZ_{Cam}	[mm]

CHAPTER 1

INTRODUCTION

> Aerodynamics is for people who can't build engines.
>
> Enzo Ferrari

Enzo Ferrari, the founder of the homonymous F1 team and car manufacturer, pronounced these words in 1960, answering to the driver Paule Frére who was complaining about the low maximum speed of his 250TR in Les Mans circuit. Enzo Ferrari, at that time, did not know what would have happened seventeen years later, when Colin Chapman designed the Lotus 79. That car was the first F1 car dominating an F1 world championship through its aerodynamics, taking full advantage of the studies made by the team Lotus on the ground effect. From that moment on, aerodynamics became, and is still nowadays, one of the most important fields of development of race-cars, a fact also underlined by the number of literature written on the argument during the decades, such as Katz (1995), a book that never misses from the table of any Aerodynamicist in F1.

(a) (b)

Figure 1.1: (a) Lotus 79 (1977, Lotus)(b) RS17 (2017, Renault).

From the first developments done by Chapman, the race-car aerodynamics has developed deeply and the aerodynamic devices have changed profoundly as Fig.(1.1) shows. Here, the cited Lotus 79 and the RS17, model designed by Renault for the 2017 F1 championship, are illustrated. It is clear from the images that, along these fifty years, F1 cars have changed drastically. Nowadays they are bigger, heavier but, most importantly, faster. However, not only the cars themselves progressed but also the tools available to engineers changed profoundly. Computer-Aided Design (CAD) and Computational Fluid Dynamics (CFD) appeared, permitting the design of really complex geometries and the consecutive analysis of those in aerodynamic terms. However, despite the continuous growth in computational power, solving numerically and precisely such a complex flow field, as the one around a modern F1 car, is still not possible nowadays. For this reason, it is still vivid the necessity for quantitative experimental methods to determine the aerodynamic features of the flow around the car, to tune and guide the numerical models used in CFD.

Multiple different techniques have been developed to measure experimentally the flow, not only qualitative but also quantitative, during a wind tunnel test. Pitot tubes, laser-doppler velocimetry and hot wire can be cited as flow measurement techniques, however, nowadays Particle Image Velocimetry (PIV) is the technique that promises most.

Despite a quite complicate setup, usuall involving multiple cameras and a laser, the concept behind this technique is rather simple. In order to measure quantities related to air, first of all, it must be possible to "see" the air itself. Flags waving in the wind can be a first example of "looking" at the air, indeed their movement gives an indication of the direction of the wind to the observer. Following the same concept, in Particle Image Velocimetry, in order to make visible the motion of the fluid, a certain seeding is inserted into the flow. Illuminating and recording this motion permits to evaluate the flow velocity, from which all other quantities can be derived, such as vorticity and, lately, also pressure.

As F1 teams have followed the technological development, also PIV has advanced deeply over the years, evolving from planar to 3D time-resolved measurement. Its developments has been reported by Adrian (2005) for what concerns 2D PIV, and by Scarano (2013) for what concerns 3D tomographic PIV, appeared by the work of Elsinga et al. (2006). A review of fundamentals of particle image velocimetry is given in Chapter 2.

Due to its ability to measure the entire velocity field on a plane or in a volume and its non-intrusiveness, citing some of the advantages, in the last decade, several companies and most of the F1 teams have begun to equip their wind tunnel with the necessary tools to perform PIV measurements. However, planar and stereo PIV are preferred w.r.t. tomographic PIV, due to some known shortcomings of the latter (Cardano et al. (2008) and Jux (2017)). The most relevant of them can be summarised as:

- difficulty in handling complex geometry
- lengthy calibration procedure and needing of re-calibration
- limitation in the measurement domain
- long time required to process the data

All of them can be addressed by considering the option to use the Robotic Volumetric PIV system, presented by Schneiders (2017) and Jux (2017), formed by a coaxial velocimetry probe moved by a six-degrees of freedom robotic arm, coupled with the choice of HFSB as seeding and Shake-the-box as the tracking method. A more in-depth review of the system is presented in Chapter 2. However, another requirement appears if the system is to be used in an industrial environment or in F1 testing: the high speed at which aerodynamic tests are performed. Indeed, the maximum flow speed that can be analysed with STB algorithm depends on the maximum frequency of the cameras employed. Considering the system used by Jux (2017), which has been used also in this project, the maximum acquisition frequency of the cameras is $f_{max} = 750\ Hz$, that leads to a maximum resolvable flow velocity of about $U = 15m/s$, far lower than the 48 m/s usually used in a F1 wind tunnel for example.

This limitation inspired the research objective of the presented master thesis:

> *"evaluate the feasibility and design a method to increase the velocity range of application of the Robotic Volumetric PIV system"*

In order to achieve the prefixed goal, since the impossibility to use a time-resolved approach given the fixed maximum acquisition frequency, not considering any hardware modification, a multi-step method based on multiple double-pulse acquisitions at increasing pulse separation times Δt has been designed, implemented and applied. The proposed method is analysed more in-depth in Chapter 3, where it is also compared to a standard double-pulse approach. In order to assess the performances of the designed technique, an experiment on the near-wake flow of an Ahmed body has been carried out at Open Jet Facility at TU Delft, whose apparatus and procedures are discussed in Chapter 4. The choice of this specific test object is driven by its role as proof-of-concept in automotive industry, one of the possible field of application of the Robotic Volumetric PIV.

During the experimental campaign, the flow topology has been investigated at two different velocities, 12 m/s and 20 m/s. The former speed is selected to be able to compare the results obtained by the proposed method with the ones given by the standard acquisition and processing technique, consisting in applying STB to time-resolved data. The latter flow velocity, too high to be resolved with the standard technique, is chosen to prove the capability of the proposed method to enlarge the resolvable velocity range. The results are shown in Chapter 5. In order to highlight the need of a multi-step approach, results from a standard double-pulse acquisition strategy are also included. Finally, in Chapter 6 conclusions are drawn and limitations of the developed system with possible further future improvements are given.

CHAPTER 2

LITERATURE REVIEW

2.1 RACE CARS AERODYNAMICS

As stated in Chapter 1, after the advent of the Lotus 79, in F1 aerodynamics has gained a crucial role in the battle for the championship, role that has still nowadays. In this section, a brief introduction on the importance of aerodynamics for race cars is given.

In a car, even more in a racing car, the forces generated during braking, acceleration and cornering are created at the contact patch between the tires and the tarmac. The forces that the tire is able to transfer to the ground are directly proportional to the vertical forces applied to the tire itself and limited by a maximum friction coefficient. If, for example, cornering is considered, lateral forces at the contact patch have a crucial role in determining the maximum turning speed of the car. In this case, an increase of the vertical forces is translated directly into an increase in the maximum speed reachable avoiding the sliding. This leads to a decrease of lap time, the final aim of race car design. The straightforward method to increase the normal forces applied to the tires is to increase the weight of the car. However, this solution would not work because of the correspondent penalty in acceleration, that would nullify the beneficial effect. For this reason, aerodynamic downforce has been found to be really effective, due to its ability to increase the vertical forces without bringing a weight penalty for the car. In order to summarise all these considerations, the acceleration of a car can be illustrated by the following equation (Zhang et al., 2006):

$$a = g \cdot \mu_{max} + \frac{C_z \cdot \mu_{max}}{M} \tag{2.1}$$

where g is the acceleration due to gravity, μ_{max} is the peak coefficient of friction of the tire, M is the mass associated with that tire and C_z is the aerodynamic downforce. The potential of aerodynamics has been observed in the race car environment for the first time at the end of the 1960s, becoming definitely a game changer for the category.

Fig.(2.1a) shows the development of the one-lap time at Indianapolis Speedways along the last decades of the 20th century. If the continuous improvement until the 60s is given by the gradual enhancement in various technical aspects of race car design, the jump of 1972 has been attributed mainly to the appearance of the new usage of front and rear wings (Katz, 1986). As introduced

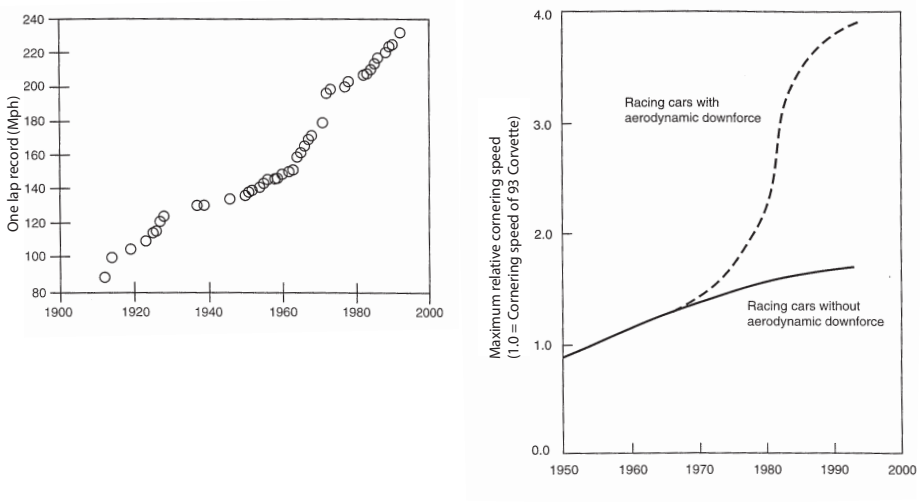

(a) (b)

Figure 2.1: (a) Variation of the measured single averaged speed in Indianapolis Speedway and (b) Maximum cornering speed development. Both reproduced from Katz (1995).

.

before, one of the beneficial effects of aerodynamic downforce is the increase in cornering speed. Fig.(2.1b) shows a graph presented by Katz (1995), where the maximum relative cornering speed of race cars is compared, taking as reference the 1993 Chevrolet Corvette. From the broken line, that represents the performances of the most advanced vehicle, such as F1 and Indi, it is possible to notice the huge increase in cornering capability given by the implementation of aerodynamic devices. The considered line becomes steeper around the end of the 70s, fact given by the introduction of the already mentioned ground effect. These results led to a contemporary increase of interest of both the academic and industrial word towards the effect of the aerodynamic devices on race cars. Due to the high competitiveness and secretiveness of the motorsport environment, the literature available is limited and the majority of the studies have been done in the academic world. An exception is a work presented by Wright (1982), director of the Team Lotus International, at the I.A.V.D. International Conference on the impact of aerodynamics on vehicle design, in which an assessment of the influence of aerodynamic developments on the Formula One racing cars design is done. On the theoretical side, the work done by Katz (1986) can be cited as one of the first work done on the subject, in which the author demonstrated that, through the panel method, a lifting race-car body can be transformed to one that produces downforce thanks to the addition of a front-wing and rear-wing. After taking advantage of the beneficial forces created by inverted wings, other devices have been developed, more and more with the intent of exploiting more complicated phenomena, such as the ground effect and the vortex interaction. For this reason, F1 cars geometries have become increasingly complicated and sophisticated, as shown by the comparison made in Fig.(1.1).

For what concerns the academic world, multiple studies have been performed to understand the role and the importance of different aerodynamic devices, such as the series of experiment done

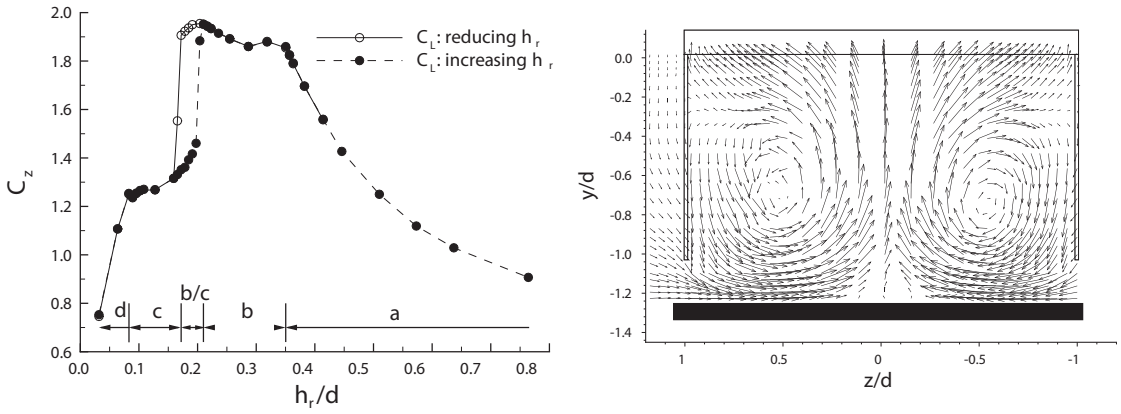

(a) (b)

Figure 2.2: (a) Downforce of a bluff body equipped with a diffuser at different ride height and (b) mean flow velocity measured with LDA in plane perpendicular to the free-stream. Both reproduced from Zhang et al. (2004).

.

by Ranzenbach and Barlow between 1994 and 1997, and done by Zhang et al. in the early 2000's (Zhang and Zerihan (2003a), Zhang and Zerihan (2003b), Zhang et al. (2004), Zhang and Zerihan (2004), Zhang et al. (2006)).

Zhang et al. (2004) is an example of a study done on the vortical structure behind a bluff body with a slant surface at the back, representing a simplification of a modern diffuser. This device, a slant surface at the inferior back of the car, permits to exploit the ground effect in order to increase downforce. Through wind tunnel test with $U_\infty = 20\ m/s$, performing balance and 2D LDA measurement, the behaviour of a diffuser in ground effect has been characterized at different ride height, as reported in Fig.(2.2a). The author underlines the connection between the vortical structures, found by 2D vorticity analysis, produced by the aerodynamic device ant its downforce production. Every stage presented in Fig.(2.2a) is characterized by a specific position and intensity of the vortices seeable in Fig.(2.2b).

Inverted multi-element wings are another device used for race car aerodynamics. Zhang and Zerihan (2004) investigates the aerodynamic behaviour of a double-element wing in ground effect with $U_\infty = 30\ m/s$ through balance and pressure measurements, with the usage of planar particle image velocimetry to investigate the vortical structure created at the tip of the wings.

Also in this case, it has been found a direct link between the strength of the vortical structures, measured with planar PIV, and the overall behaviour of the wing. When the tip vortex is stronger, the downforce produced a the tip increases, enhancing the aerodynamic behaviour of the wing.

As seen, several measurement techniques can be employed in order to enhance the understandings of race-car aerodynamics. Specifically, in the last decade, PIV has been started to be used more and more, as it can be seen in Zhang and Zerihan (2003a) and Issakhanian et al. (2010). However, it can be noted that the PIV measurements done are mainly limited to 2D, with the usage of planar or stereo PIV, due to limitations of the classic 3D PIV that will be introduced in the Sec.(2.3).

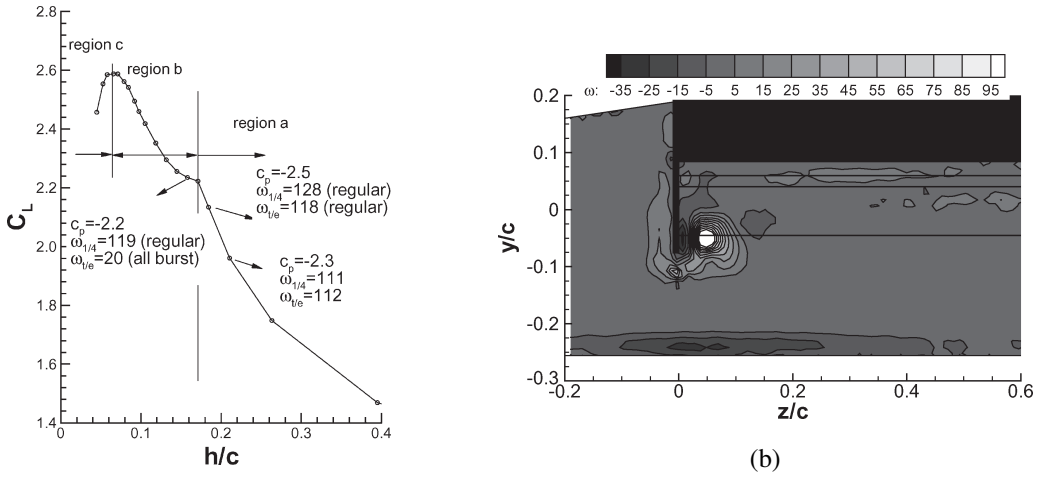

(a) (b)

Figure 2.3: (a) Downforce of a double-element wing in ground effect at different ride height and (b) mean vorticity measured at x/c = 0.672 with PIV in plane perpendicular to the free-stream. Both reproduced from Zhang et al. (2004).

.

2.2 AUTOMOTIVE AERODYNAMICS

Aerodynamics for race cars, F1 cars specifically, is mostly focused on the optimization of the car performance through a balance of downforce and drag production. For what concerns the automotive industry, contemporary to the appearance of aerodynamics in motorsport, due to the "*Oil Crisis*" of the '70s, researchers have started to focus on the reduction of consumption for transportation. If the studies of inverted wings were performed starting from the wing theory already known for aeronautical application, the aerodynamics of a bluff body in ground effect differs from what studied at that time. The first works done in the late '70s identified in the slant angle φ, the angle between the horizontal plane and the rear-window, as a key parameter for the drag determination of a road vehicle. One of the milestones in the study of road vehicle aerodynamics is the work published by Ahmed et al. (1984). They introduced a standard simplified model that is still nowadays considered a benchmark for road vehicle drag determination, the so-called "Ahmed reference body", shown in Fig.(2.4) and considered also as test object for the current project. As mentioned before, the most interesting feature is its slant angle at the rear. During the following decades, several different slant angles have been investigated. Two main flow pattern have been identified: two-dimensional flow for angles that are outside the range $12° < \varphi_{3D} < 30°$, and highly three-dimensional flow when the slant angle is in the mentioned range. When the slant angle is in the mentioned range, two counter-rotating vortices appear, driven by the low pressure on the slant given by flow separation. Due to the downwash created by the mentioned vortices, the separation on the slant is limited in length, creating a separation bubble. Due to the presence of these vortical structures, the highest drag is reached in the region of three-dimensional flow, with a peak around $\varphi = 25°$.

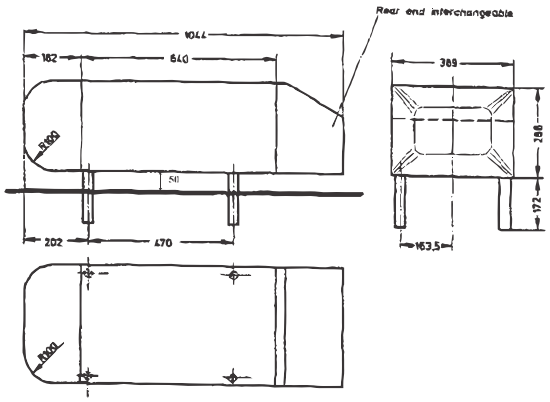

Figure 2.4: Geometry of the reference model introduced by Ahmed et al. (1984).

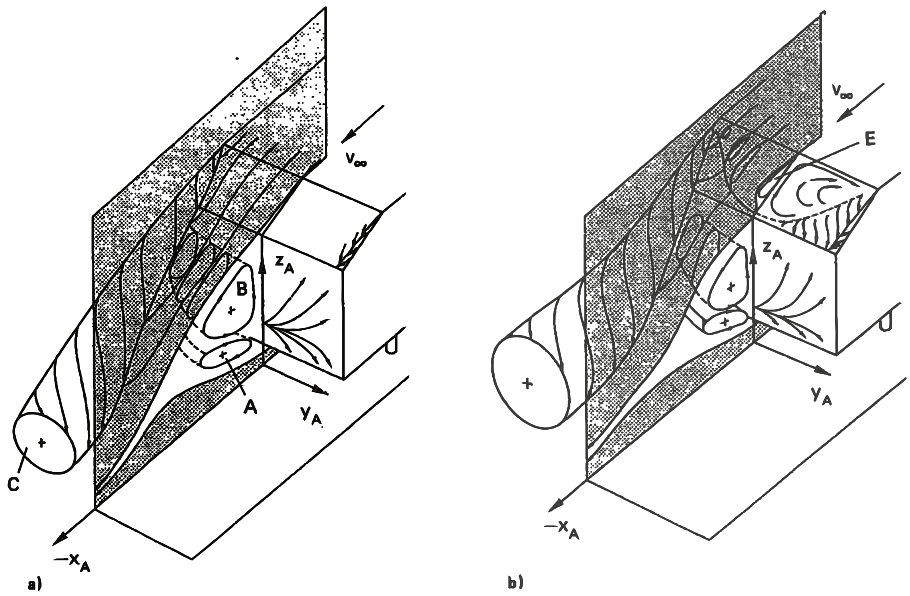

Figure 2.5: Vortex system for a fastback Ahmed body with: (a) low drag coefficient, (b) high drag coefficient with $\varphi = 30°$ (Ahmed et al.,1984).

Even if the shapes of modern cars are far more complicated than the one introduced by Ahmed, the Ahmed body is still nowadays considered as a proof-of-concept for new drag reduction technique. Furthermore, the high complexity of its near wake makes it perfect to test new measurement techniques.

As it can be noticed in the last two sections, three-dimensional flow and vortical structures are of main interest for what concerns automotive and motorsport aerodynamics. For this reason,

Robotic Volumetric PIV could be the proper tool to allow a better understanding of the mentioned phenomena. However, as testified by the examples found in literature, the velocities typical for wind tunnel testing for automotive and motorsport applications are in the range between 20 m/s and 50 m/s. This has been the main requirement that the technique presented in Chapter 3 had to satisfy.

2.3 Particle Image Velocimetry and its state-of-the-art

In this section, a brief summary of the history and developments of PIV is given. After a first insight on the working principle of this technique, some of its development milestones, such as the development from 2D to 3D or the appearance of the Robotic Volumetric PIV, are further discussed. The last paragraph discusses more in-depth the techniques available in the literature to enlarge the dynamic velocity range, explaining the reasons behind the decision of setting up this project.

2.3.1 2D Particle image velocimetry

PIV is nowadays a well-known flow measurement technique, not used anymore only in university for fundamental research, but also spread in the industrial environment (Jux, 2017). As stated in the introduction, its fundamental principle is to follow and measure the displacement of tracer particles inside the flow, from which the flow velocity can be calculated. Born in the 1980's as *laser speckle velocimetry* (LSV) by Meynart works, since 1984 the name *particle image velocimetry* has been introduced Adrian (1984) and used still nowadays. In the first decades, the development of PIV was centred on the 2D evaluation of the flow, giving as result the distribution of two velocity components on a plane (2D2C). Several improvements to the 2D technique have been introduced in the first years of the 1990's. Significative examples are the videographic recording, whose performances were asserted by Willert and Gharib (1991) and Westerweel (1993), and the appearance of the interline transfer cameras (Lourenco et al., 1994), hardware still used in the state-of-the-art of the technique. Fig.(2.6) shows a typical setup for a 2D PIV experiment. A laser beam is expanded through a

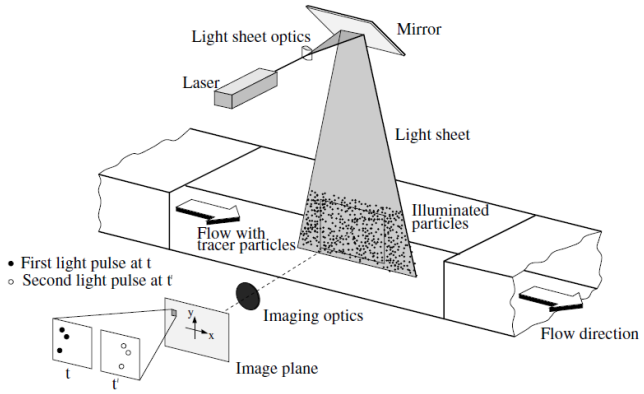

Figure 2.6: Skecth of generic planar PIV setup. Reproduced from Raffel (2007).

light sheet optics and illuminates a portion of a plane of the flow field. One or multiples cameras, respectively for planar or stereoscopic 2D PIV, record pairs of images with a time delay between each element of the pair equal to Δt. At this point, two different approaches can be used: the particle-based approach or the correlation-based approach. Considering the former, in order to evaluate the flow field, each particle is followed individually from one frame to the subsequent one. This technique is referred as Particle Tracking Velocimetry (PTV). On the other hand, correlation-based approach consists in the discretization of the image into interrogation windows and the subsequent cross-correlation between correspondent windows. This is commonly referred as Particle Image Velocimetry (PIV).

If the correlation-based approach is considered, the displacement of the particles is statistically determined through cross-correlation and the velocity in the real space is calculated by:

$$u = \frac{\Delta X}{M \Delta t} \tag{2.2}$$

$$v = \frac{\Delta Y}{M \Delta t} \tag{2.3}$$

where the capital letters are referred to the image plane and M is the magnification factor. As in all kind of measurement, it is possible to expect an error in the velocity determination. If the error related to Δt is considered negligible, the standard deviation of the velocity can be defined as:

$$\sigma_u = \frac{\sigma_{\Delta X}}{M \Delta t} \tag{2.4}$$

where the evaluation of $\sigma_{\Delta X}$ is not straightforward. Adrian (1991) hypothesized the following relation:

$$\sigma_{\Delta X} = c_\tau d_\tau \tag{2.5}$$

where c_τ is a constant depending on the system used and d_τ is the image particle diameter. It is important to underline two aspects of Eq.(2.5): first of all its 2D nature, since it takes into consideration only in-plane characteristics, as the particle diameter, secondly, it does not consider the systematic error introduced by specific phenomena, such as peak locking. After having defined the error of the measurement, in order to characterize a PIV system, it is useful to defined the *dynamic velocity range (DVR)*, a dimensionless number defined as:

$$DVR = \frac{u_{max}}{\sigma_u} \tag{2.6}$$

that represents the ratio between the maximum velocity to the minimum resolvable velocity. This number is useful to understand which scales are possible to be resolved by a specific PIV system, and it is required to be as high as possible. While in the first years of the development of the technique, the DVR was limited to ≈ 10, improvements in the hardware and in the software have increased it until ≈ 200 Adrian, 2005. As introduced before, if a camera is added to the setup, stereoscopic PIV (2D3C) becomes feasible, permitting to calculate also the out-of-plane component of the velocity. This technique is strongly reliable and nowadays represents the most used technique at the industry level, as shown by Jux (2017).

2.3.2 Volumetric PIV and development of 3D-PTV algorithms

From the beginning of the technique, the ability to measure 3D volumes has been considered one of the fundamental step necessary to be able to understand the topology of fully 3D coherent flow structures. Considering planar PIV, if the flow does not present particular symmetries, several planes would be necessary in order to characterize it, with all the difficulties associated with the movement of a PIV system. One of the first attempts to evaluate a 3D portion of the flow field was done by Brücker, who used a scanning system in order to move the laser plane and get slices of the flow field of a cylinder wake (Brücker, 1995). After the work done by Brücker, there have been other attempts to reach the ability of a 3D measurement, however, the most important breakthrough towards that direction has been done with the introduction of the tomographic PIV, done by Elsinga et al. (2006). Based on 3D object reconstruction, this technique brought many advantages compared to the existing planar PIV, overall in what concerns the vortex detection, the pressure reconstruction and the ability to evaluate the performance of the system and the error analysis Scarano (2013). Since its introduction, tomo-PIV has had a great success, as reported by Schanz et al. (2016), due to its processing robustness and thanks to the developments done in the calibration accuracy. However, from the beginning, it has been clear that some drawbacks were present in the method, such as the burden in terms of computational cost, due to the reconstruction of the entire volume for each snapshot. Furthermore, the presence of ghost particles can affect strongly the reconstruction of the particles in the measurement volume, especially when high particle image densities are considered. These drawbacks have been addressed through the advent of modern particle detection and tracking techniques, as explained in the following part of this chapter.

Already at the time of the advent of tomo-PIV, solutions in order to triangulate the single particles, instead of reconstructing the entire volume, were available. The particle position firstly is found in the image plane and, afterwards, a triangulation procedure is used to find a possible 3D position that matches the different image-plane position in all the cameras. After having found the coordinates of N particles in space in M different frames $\left\{x_i = (x_i^1, x_i^2, x_i^3) \in t_j, i = 1 \dots N, j = 1 \dots M\right\}$, a tracking procedure can be used in order to build up the particle trajectories. This procedure is defined as particle tracking velocimetry (PTV) and one of its advantages compared to tomo-PIV is the lower computational cost, treating only the single particles and not reconstructing the entire volume, keeping the velocity information at the particle position and not averaging it into a volume. Furthermore, this technique can theoretically offer a higher spatial resolution, since the information is kept at the particle position and not averaged in a volume. However, if for the detection step a standard triangulation is used, the maximum particle density allowed is limited to 0.005 ppp Maas et al. (1993) in order to reduce the ghost particle triangulated and maintain a good robustness of the method. For this reason, most experiments performed with 3D-PTV before the 2013 reported seeding density lower than 1‰, one order of magnitude lower than what reachable with the tomographic reconstruction technique Wieneke (2013). This limit has been overcome with the advent of the Iterative Particle Reconstruction[1] by Wieneke (2013), a hybrid algorithm based on the comparison between the recorded images and the projections evaluated from the particle distribution.

[1] hereafter referred to as IPR

Iterative particle reconstruction

Fig.(2.7) shows the flow chart of IPR method. Starting from the recorded images, an initial 3D-triangulation using the standard method is performed, in order to have a first guess of the possible 3D position of all the particles. Given the result of this first step, from the 3D particle distribution, 2D projection images are produced and compared to the initial recorded images. In this step, in order to project each 3D particle p, with coordinates (x_p, y_p, z_p) and intensity i_p, back on the image plane, the following equation is used:

$$I^i_{part}(X_i, Y_i, p) = ae^{-(bx'+cy')} \tag{2.7}$$

where

$$x' = (X_i - X_{ip})\cos(\alpha) + (Y_i - Y_{ip})\sin(\alpha) \tag{2.8}$$

$$y' = (X_i - X_{ip})\sin(\alpha) + (Y_i - Y_{ip})\cos(\alpha) \tag{2.9}$$

and the particle image center defined as:

$$(X_{ip}, Y_{ip}) = M_i(x_p, y_p, z_p) \tag{2.10}$$

where M_i and the OTF parameters (a, b, c) are free to vary both among cameras and in space. After having summed for each camera the intensity of all the particles projected, the residual image is calculated as follows:

$$I^i_{res}(X_i, Y_i) = I^i_{rec}(X_i, Y_i) - I^i_{proj}(X_i, Y_i) \tag{2.11}$$

After this operation, the position of each particle is refined adding its residual to the particle itself, finding a new particle position through the minimization of the difference between the new particle and the sum between the residual and the old particle. After the correction of the particle position, the particle intensity is as well refined, deleting particles whose intensity falls below a specific threshold, decided but the user.

At this point, all the operations can be repeated multiple times in order to increase the accuracy of the final particle position and intensity. Hereafter, the operation of projection and subtraction between residual and recorded images will be referred as outer loop, while the position and intensity optimization will be referred as the inner loop. Any combination of the outer and inner loop can be used. Increasing the number of loops, the accuracy of the final results increases as well, however aggravating the computational cost of the process.

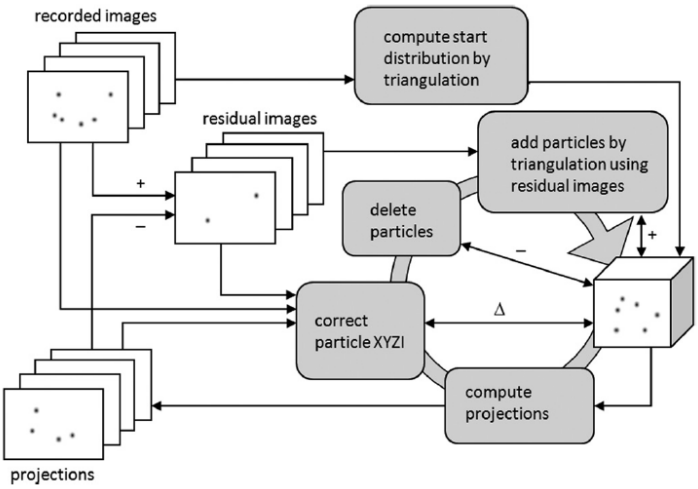

Figure 2.7: IPR working flow. Figure reproduced from Wieneke (2013).

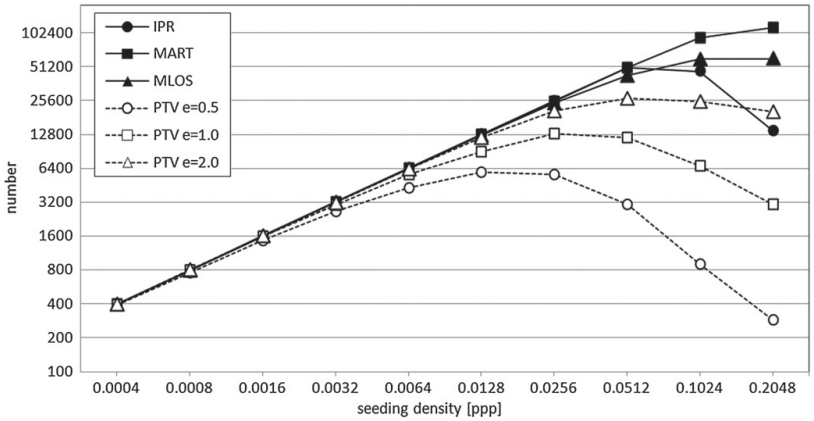

Figure 2.8: Comparison between 3D-PD, IPR and MART w.r.t the number of detected true particle. Reproduced from Wieneke, 2013

.

The main advantages of this technique are its ability to deal with seeding density up to 5% ppp, the limit at which even the tomographic reconstruction starts to fail, as shown by Fig.(2.9), and its higher accuracy in the considered ppp range. The output, for every single snapshot, of IPR algorithm is a list of N particles, where for each of the particle number, position in x, y, z and intensity are defined.

Shake the Box, Lagrangian particle tracking algorithm

After, the particle detection step, doable with IPR as introduced before, a tracking algorithm can be used in order to evaluate the flow field velocity. A list of tracking techniques can be found in

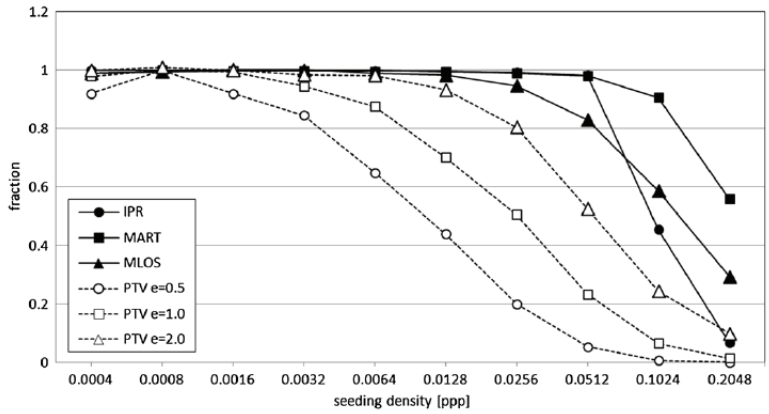

Figure 2.9: Comparison between 3D-PD, IPR and MART w.r.t the fraction of detected true particle. Reproduced from Wieneke, 2013

.

the work done by Pereira et al. (2006). Most of these methods are already beneficial in terms of computational cost w.r.t. the tomographic reconstruction, however, every single time-step is treated individually, neglecting the possibility to use the temporal information in case of time-resolved measurement. For these kinds of measurement, a reliable and highly efficient tracking algorithm has been introduced by Schanz et al. (2016), called Shake the Box [2]. Nowadays this method is considered the state-of-the-art of the technique and it has been used as the benchmark for the measurement done in the present work.
STB algorithm can be subdivided into three different phases:

- Initialization
- Convergence
- Converged state

The first phase is the *Initialization*. At the beginning of the processing, no track information is given. For this reason, a standard PTV approach, for example, IPR with a subsequent nearest neighbour tracking algorithm, is used in the first n_{init} time-steps in order to create the first group of trajectories. Only trajectories formed by at least n_{init} are taken into consideration and validate through a top-hat filter on the velocity and the acceleration. In the *Convergence* phase, the information given by the first tracks formed during the previous phase is used to predict the particle position at for the next time-step. After having predicted the new position, an image matching technique is used to correct the position itself. The intensity of each particle is then corrected and new particles that entered in the field of view are individuated from the residual images. At every time-step, new tracks are searched, using the existing neighbour tracks as a predictor, calculated through a Gaussian-weighted average. The main advantage of this procedure is that proceeding in the time-steps, the reconstruction becomes easier since more and more valid tracks are used to create the

[2]Hereafter referred as STB

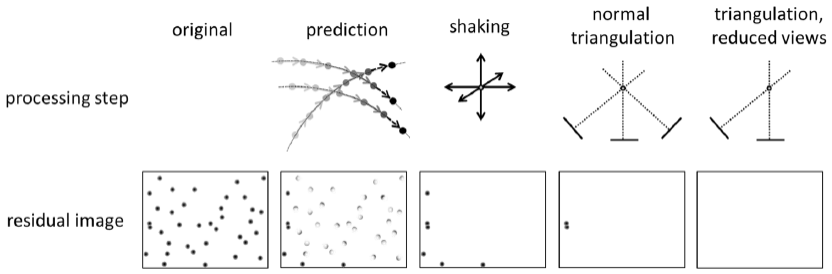

Fig. 1 Schematic description of the Shake-The-Box procedure for one time-step in the converged state by illustrating the effects of the different computation steps on the residual image of one single camera (out of multiple)

Figure 2.10: Working scheme of STB algorithm in the convergence fase. Reproduced from Schanz et al. (2016).

predictor. Finally, when the number of tracks does not change significantly between time-steps, the *Converged state* is reached. The operations done in this phase do not change w.r.t. of the previous one and are represented in Fig.(2.10).
The advent of STB has introduced so an efficient and robust way to analyze time-resolved data with a lower computational cost w.r.t. tomographic PIV. However, for any high-speed system, there will be a maximum velocity at which the algorithm works. In fact, considering the first step of the procedure, so the initialization phase, since it uses a classical tracking method based on the nearest neighbour, it is necessary that the following condition is fulfilled:

$$u \cdot \Delta t << \overline{r} \tag{2.12}$$

where u is the flow velocity, Δt the distant in time between two consecutive snapshots and $\overline{r}$ the mean particle distance. If Eq.(2.12) is not satisfied, spurious tracks could be formed and affect the entire successive calculations. Furthermore, another limitation is given by the minimum length of the tracks, n_{min}: in order to be tracked successfully any particle has to be recorded at least n_{min} times before leaving the field of view. These limits are further discussed in Chapter3, where the reasons behind this project are explained and the main outcome is presented.

2.4 Large scale PIV: HFSB and Robotic Volumetric PIV

The previous sections dealt with the some of the most important milestones of the PIV development in the last decades. The advent of STB introduced a highly efficient and robust method for analyzing time-resolved PIV dataset. However, some other developments must be cited before dealing with the main topic of this project.

2.4.1 Helium filled soap bubbles

As reported by Scarano et al. (2015), tomographic-PIV has not spread among the industrial wind tunnels in the decade after its appearance. The main limitations that made this occurred can be summarized in its computational cost and in the limited extent of the measurement domain achievable due to the limited pulse energy that is given by the illumination source. If the advent of STB

overcame the first issue, a first improvement for what concern the dimension of the measurement volume has been given by the appearance of the HFSB (Scarano et al. (2015)). Due to their diameter of approximately $300\mu m$, about two order of magnitude larger than the one of the standard seeding used, it has been possible an increase of the scattered light amount of approximately $10^4 \div 10^5$ (Schneiders (2017)), permitting a consecutive notably expansion of the measurement volume without necessitating of a more powerful light source system. If the increase in diameter improves the scattering properties of the particles, it can affect their ability to follow the flow correctly. In PIV, one of the main requirement for the choice of the seeding is that it must be able to follow accurately the flow and, furthermore, it must respond to any change in the flow within a time smaller than the time scales that have to be studied. If small spherical particles are considered in conditions in which viscous forces are predominant w.r.t. the inertial ones, it is common to evaluate their ability to respond to flow changes considering the so-called slip velocity or velocity lag (Raffel (2007)):

$$U_s = d_p^2 \frac{\left(\rho_p - \rho_f\right)}{18\mu} \frac{dU}{dt} \tag{2.13}$$

where d_p is the particle diameter, ρ_p and ρ_f the densities of particles and fluid, respectively, and μ is the dynamic viscosity. It is clear that, in order to try to maintain the same slip velocity, if d_p is increased, the particle density ρ_p must be decreased. This is the reason behind the choice of mixing air and helium to fill the bubbles, aiming to reach a neutral buoyancy of the HFSB w.r.t. air. Scarano et al. (2015) measured the response time τ_p of the HFSB, estimated to be approximately 10 μs. For these reasons, HFSB has been considered a suitable seeding for large-scale wind tunnel experiment (Scarano et al. (2015)). One of the main characteristics of their usage is the limited concentration achievable with respect to the one usually reached with the standard fog, as reported by Caridi et al. (2016). At the beginning of their usage in wind tunnel, considering, for example, the experiment done by Caridi et al. (2016), the bubbles were produced and accumulate in a reservoir and afterwards, with the help of a piston, injected in the flow through nozzles of an aerodynamic rake. To demonstrate the capability of the HFSB, in the mentioned work, the tip of a VAWT has been investigated. The setup of the experiment is shown in Fig.(2.11a), where all the main components are indicated. Fig.(2.11b) shows iso-surfaces of vorticity obtained by the usage of HFSB coupled with STB and VIC+, a novel data processing technique introduced by Schneiders, 2017.

Bringing the production of the bubbles directly on the aerodynamic rake has been the subsequent step, as seen in Caridi et al. (2017). Due to this development, it is possible to assume a more uniform concentration of bubbles in the seeded domain. However, it must be remarked that, even with this kind of technology, the concentration achievable with HFSB is at least one order of magnitude lower than the one achievable with the standard aerosol fog. This limitation can be bypassed by accumulating bubbles in the volume before running the measurement, as done for example by Spoelstra et al. (2018). However, filling up the volume with bubbles is usually not possible, overall if multiple measurements have to be taken. On the other hand, if the lower concentration can be seen as a negative feature for classical PIV, it further justifies the choice of using PTV algorithms, such as STB, as processing technique. If the main interest of the experiment is to evaluate averaged flow quantities, a possible solution w.r.t. the low concentration of HFSB is to extend temporally the measurement, as proposed by Kähler et al. (2012). In fact, acquiring more data, it is possible to in-

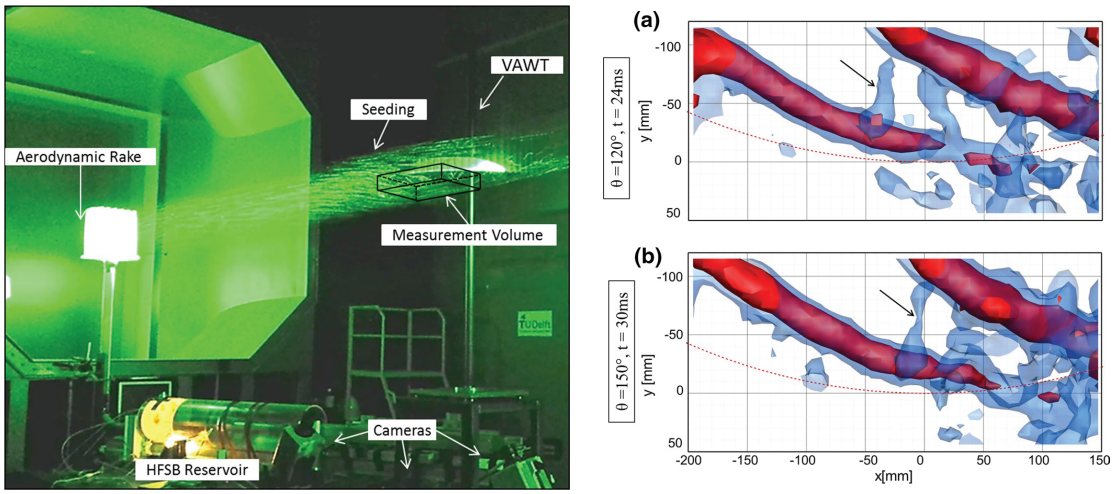

(a) (b)

Figure 2.11: (a) Setup of experiment performed by Caridi et al. (2016) on a volume of 40 × 20 × 15 cm^3 investigating the tip vortex of a VAWT (b) Instantaneous iso-surfaces of vorticity magnitude of tip vortex, obtained by the application of VIC+ data processing. Both reproduced from Caridi et al. (2016).

.

crease the spatial resolution of PTV results, up to the physical limit given by the particles diameter, that for the HFSB is in average 300 μs.

2.4.2 Robotic Volumetric PIV

As introduced before, two factors can be addressed as the main limitations that prevented 3D TOMO-PIV to spread in an industry environment: the limited dimension of the measurement domain and the high requirements in terms of optical access. The introduction of the HFSB, as explained before, has mitigated the first problem, but the very recent advent of the Robotic Volumetric PIV (Jux (2017) and Schneiders (2017)) seems to have opened the possibility to measure averaged quantities in a volume theoretically unlimited in dimensions. The Robotic PIV system is formed by two main component. The first is a CCV probe that contains Four LaVision MiniShaker S CMOS imagers (831 × 631 pixels at 471 fps, 10 bits), with an optical fibre, whose end is positioned between the cameras to achieve coaxial imaging and illumination, able to transmit the laser power. The laser light that comes from the end of the fibre is conically expanded through a spherical lens at the source. Moreover, a micro-lens is positioned at the end of the fibre itself in order to obtain an additional expansion. The coaxial configuration is achieved thanks also to the reduction of the tomographic aperture β by an order of magnitude w.r.t. one suggested for an optimal tomographic reconstruction, as shown in Fig.(2.12).

Considering Fig.(2.12), the final measurement volume is represented by the area underlined by the dotted red line, sensibly bigger than the one obtainable by a traditional tomographic setup. On the other hand, if the low tomographic angle increases the volume measured, it also affects the

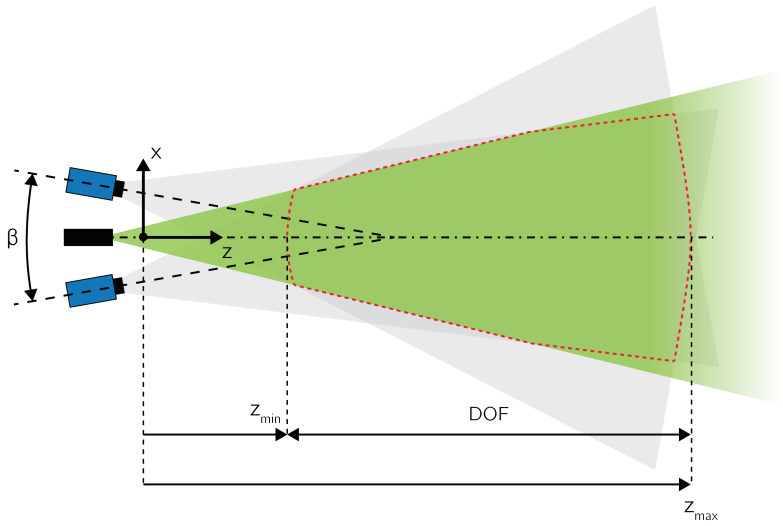

Figure 2.12: Schematic description of working principles of CVV. The volume underlined by the red dotted line represents the measurement volume, where the camera fields of view and the volume illuminated by the expanded laser light intersect. Figure reproduced from Giaquinta (2018).

accuracy of the tomographic reconstruction or 3D particle detection. As shown by Scarano (2013), the shape of the reconstructed particle increases if β reduces.

This leads to an increase of the particle positional uncertainty along the coaxial direction by one order of magnitude w.r.t. the one in the two other directions, as discussed more in detail in Sec.(3.2). If time-resolved data are acquired, the increase of the uncertainty in the velocity measurement given by the lower tomographic aperture can be alleviated by sampling the same particle at multiples times and computing its trajectory by multi-framing techniques, as STB (Schneiders (2017)).

The position and the orientation of the probe are controlled by the second main component, a robotic arm. The robotic arm considered for this project is the same used by Jux (2017) and Schneiders (2017), an Universal Robots UR5. It is a six-degrees of freedom robotic arm, able to move within a spherical region of radius $r = 850\ mm$, whose characteristics will be further described in Sec.(4.4.3).

One of the first experiments performed with the mentioned system is the work done by Schneiders (2017). Here, the flow around a sphere with a 10 cm diameter with $U_\infty = 2.5\ m/s$ has been studied using the Robotic Volumetric PIV in an open-jet low-speed wind tunnel at TU Delft. Fig.(2.13a) shows the results obtained by Schneiders (2017). The author reports a good correspondence between experimental data and potential flow. Furthermore, considering region away from the sphere, the author measured the uncertainty on the instantaneous velocity to be approximately 1% for the streamwise component and 8% for the coaxial component. This discrepancy will be motivated in Chapter 3.

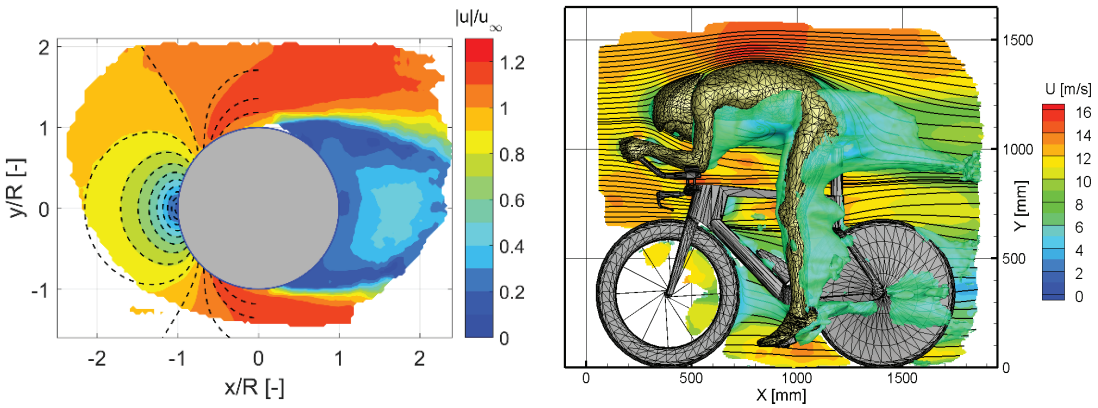

(a) (b)

Figure 2.13: (a) Time-averaged velocimety measurement of the flow around a sphere. Data acquired with the Volumetric Robotic PIV system. Figure replicated from Schneiders (2017). (b) Time-averaged flow field around the cyclist visualized by a contour of streamwise velocity in the center plane (green isosurface at u = 7 m/s). Figure reproduced from Jux (2017).

.

After the relative simple experiment of the sphere, Jux (2017) proved the capability of the Robotic Volumetric PIV analysing the near-surface flow around a full-scale model of a cyclist. In a time-span of two days, 200 measurements have been performed permitting the complete mapping of both sides of the cyclist. Fig.(2.13b) shows one of the results presented by Jux. This work demonstrated the ability of Robotic PIV to measure accurately mean flow in volumes with dimensions that were impossible to be achieved before. The measurement done by Jux have been performed with a free-stream velocity $U_\infty = 14m/s$, close to the maximum velocity at which STB can be used given the maximum frequency of *MiniShaker* cameras.

2.5 Increase of the dynamic velocity range

As introduced before, PIV is a technique able to measure velocities experimentally recording multiple images of illuminated tracers introduced in the flow and illuminated by laser light. In order to evaluate its performance it is useful to introduce parameters that give an indication about its measurement spatial resolution and the velocity resolution and accuracy, respectively the *dynamic spatial range* [3] and *dynamic velocity range* [4]:

$$DSR = \frac{l_x}{\Delta x_{p,max}} \tag{2.14}$$

$$DVR = \frac{u_{max}}{\sigma_u} \tag{2.15}$$

where l_x a characteristic dimension of the flow, $\Delta x_{p,max}$ is the maximum real particle displacement and σ_u is the minimum resolvable velocity. The standard deviation of the velocity σ_u can be expressed as:

$$\sigma_u = \frac{\sigma_{\Delta X}}{M\Delta t} \tag{2.16}$$

leading to the following definition of DVR:

$$DVR = \frac{u_{max}}{\sigma_{\Delta X}} M\Delta t \tag{2.17}$$

The technological development, both in hardware and software, has permitted to increase the DVR over the years, reaching for a conventional 2D PIV system values between 200 and 300 (Sciacchitano (2014)). However, if a high-speed PIV system is considered, the DVR reduces, typically in the range of $50 - 100$.

Looking at Eq.(2.17), it can be noticed that two different strategies can be adopted in order to increase the DVR. Firstly, it is clear that an increase of Δt would be directly beneficial for the DVR, increasing consequently the accuracy of the results.

However, an infinite stretching of the time-step Δt is not possible, since results given by both the statistical approach, PIV, and the Lagrangian particle tracking, PTV, can suffer from, respectively, loss of correlation and poor particle pairing due to excessive particle displacement between two consecutive frames. The maximum Δt permitted depends on multiple factors, such as maximum velocity and magnification factor.

Over the years, several different techniques have been developed in order to increase DVR, both extending the maximum and reducing the minimum measurable particle displacement (Persoons (2015)). One of the first examples can be identified in the idea of using multiple exposures to improve auto-correlation accuracy in photographic PIV (Adrian (1991)). After some years, Fincham and Delerce (2000) introduced the idea of performing measurement acquiring three images at times $[t, t+\delta t, t+2\delta t]$, using the result of a first correlation between the first two, as a predictor in order to find a first guess for the position of the particles in the third image. Comparing this method with the

[3] Hereafter referred as DSR

[4] Hereafter referred as DVR

standard double-pulse PIV, the DVR was increased thanks to the increment of the time-separation between the first image and the third. However, in order to perform acquisitions following this method, a system with an acquisition frequency of $f = 1/\delta t$ would be required; otherwise, multiple groups of cameras could be used, increasing the complexity of the system.

The idea of increasing the dynamic velocity range through the use of multiple exposures has been further improved by Hain and Kähler (2007) who proposed the so-called *Multiframe* method. One first correlation between two images symmetrically collocated around the n^{th} frames is performed in order to produce a velocity field with standard accuracy, obtaining a displacement of ΔX_1 at each grid point. Afterwards, the best Δt is chosen considering the calculated flow field, aiming to have a constant displacement at each grid point of 10 px, and the corresponding pair of images $n \pm m$ is evaluated, where $m = 10/\Delta X_1$.

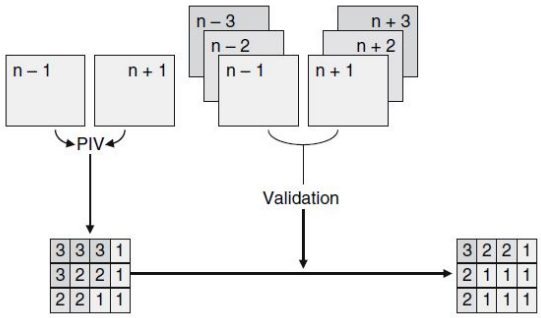

Figure 2.14: Schematic procedure of multiframe PIV. Reproduced from [Hain and Kähler, 2007].

It must be underlined that even for this method, time-resolved images have to be acquired, limiting the speed of the flow analysable due to frequency cameras limitation. Considering the double-frame imaging, Persoons and O'Donovan (2010) proposed the Multiple Pulse Separation technique. This method consists in the acquisition of double-frame images with N different increasing pulse separation times. This permit to evaluate particle displacement with an increasing Δt, improving the DVR as already demonstrated. However, in order to not encounter out-of-plane or out-of-window issues, an optimal pulse separation is chosen maximizing, locally, the weighted peak ratio Q', given by:

$$Q' = Q\left(1 - \frac{\sigma_{\Delta X}}{\Delta X}\right) \tag{2.18}$$

It must be underlined that this technique requires processing all the image pairs obtaining with increasing pulse separation, leading to an increase in computational costs. Furthermore, none of the information obtained by the correlation with a lower pulse separation is used in order to enhance the correlation at longer pulse separations.

If Eq.(2.17) is considered, another method to increase the DVR is to diminishing the uncertainty $\sigma_{\Delta X}$ on the displacement determination. Another option to increase the accuracy of the velocity determination is performing an ensemble averaging of the correlation map obtained through the cross-correlation of multiple pairs of a sequence (Meinhart et al. (2000)). From this approach, Scarano

et al. (2010) derived a method called sliding average correlation[5], which is based on the idea of averaging correlation maps that come from pairs of subsequent images. However, a necessary condition in order to have SAC working is a sufficiently high acquisition rate compared to the highest characteristic frequency of the flow that is to be studied. A new recent algorithm has been proposed by Sciacchitano et al. (2012) and it is called multi-frame pyramid correlation, that combines the idea of extending the observation time of multiple frame PIV and the ensemble correlation of SAC.

[5]Hereafter referred as SAC

CHAPTER 3

Robotic Volumetric PIV at high Re: multi-Δt DP technique

In the previous chapter, after having underlined the importance of aerodynamic testing in the automotive motorsport industry, the state-of-the-art of PIV has been identified. More in details, Robotic Volumetric PIV has been introduced, and its ability to measure large volume has been highlighted. However, the novelty features and advantages of the presented system come with a limitation on the maximum resolvable velocity, given by the maximum camera acquisition frequency.

In Sec.3.1, the mentioned limitations are analysed and available solutions found in the literature are given. In Sec.(3.2) the effect of the low aperture characteristic of the coaxial approach is discussed, characteristic that is the main reason that led to the design and the implementation of the multi-Δt technique, described in Sec.(3.3). Finally, the criterion behind the choice of the multiple Δt is discussed in Sec.(3.4).

3.1 Multi-pulse, multi-frame 3D-PTV

In Chapter 2, the Robotic PIV system has been presented as the state-of-the-art for volumetric PIV measurements. The CVV hardware, coupled with the processing technique STB, has been demonstrated to be an efficient system to perform volumetric flow field measurements at industrial scales.

Focusing on the algorithm side, as introduced in the last chapter, STB relies on 3D *particle detection* by IPR of a sequence of time-resolved recordings as starting point. After having built up tracks in all the domain, *particle prediction* is used to decrease the computational cost and to increase the accuracy of the particle reconstruction at subsequent time-steps. Indeed, when the convergence phase is reached, only a refinement of the predicted particle position is required, the so-called shaking. This procedure permits to avoid a entirely IPR reconstruction of the entire domain at each time-step, speeding up largely the process.

Another feature of STB is its ability to remove erroneous tracks created by ghost particles, enhancing the accuracy of the results. Due to their nature, it is unlikely that they follow long trajectories coherently and this permits the algorithm to identify and delete them (Novara et al., 2016). This effect increases with the number of iterations, provided that the particle density does not reach levels for which the initialisation with IPR fails, as demonstrated by Schanz et al. (2016).

If the velocity is estimated by the analysis of multiple frames, as done by STB, it is possible to achieve a reduction of the error on the velocity measurement compared to a standard double pulse system (Lynch and Scarano, 2013; Schanz et al., 2016). If the velocity is computed from a track formed by k samples, two different factors contribute to the reduction of the mentioned error. Firstly, looking at Eq.(2.17), it is clear that an increase in the overall time separation, that becomes $(k-1)\Delta t$, leads to a rise in accuracy. Secondly, the random error on the particle position at each sample is averaged, reducing the total error of a factor $\sqrt{k}$. The combination of these two effects leads to an error reduction that scales with $k^{-\frac{3}{2}}$, as already derived by Lynch and Scarano (2013) analysing data with cross-correlation. The expression that can be used in order to evaluate the relative velocity uncertainty becomes:

$$\varepsilon_{u_{MP}} = \frac{c_\alpha \varepsilon_x}{k\sqrt{k}\Delta x} \tag{3.1}$$

where c_α is a coefficient that depends on the track regularization technique used and Δx is the particle displacement between each sample. If a second order polynomial track regularization is used, Schneiders and Sciacchitano (2017) indicate the value of c_α to be approximately 3.5. The above expression permits to compare the relative velocity uncertainty obtained with a double pulse system that measures a particle displacement of Δx, given by the expression:

$$\varepsilon_{u_{DP}} = \frac{\sqrt{2}\,\varepsilon_x}{\Delta x} \tag{3.2}$$

with the one obtained by a multi-frame analysis of k samples, where the total integral displacement is again Δx. If the particle position uncertainty ε_x is supposed constant between the two acquisitions, the uncertainty $\varepsilon_{u_{MP}}$ scales with a factor $\sqrt{\frac{2}{k}}$ with respect to the one evaluated by Eq.(3.2).

These are the reasons behind the increasing interest in STB algorithm in the latest years. However, the possibility of using this algorithm for high-speed flows is limited by hardware characteristics, mainly by the maximum acquisition frequency. According to Novara et al. (2016) time-resolved sequences suitable to be analysed with STB are obtainable only for flows typically slower than 10 m/s.

For this reason, the usage of different acquiring strategies to cope with high-speed flows becomes necessary. The first possible solution is to adopt a double-pulse, double-frame[1] approach. Fig.(3.1) shows a comparison between data obtainable by TR and DP-DF acquisition strategies.

While for TR acquisitions, camera and laser frequencies are equal, obtaining a sequence of snapshots with relative time interval approximately of the order of milliseconds, for the DP-DF strategy, two pulses in rapid succession are recorded on different frames, where Δt can be of the order of μs. After T, of the order of a few milliseconds, another pair of pulses is recorded. It must be remarked that, due to the long interval between the couples of pulses, usually it is not possible to link pairs obtained at different time-steps.

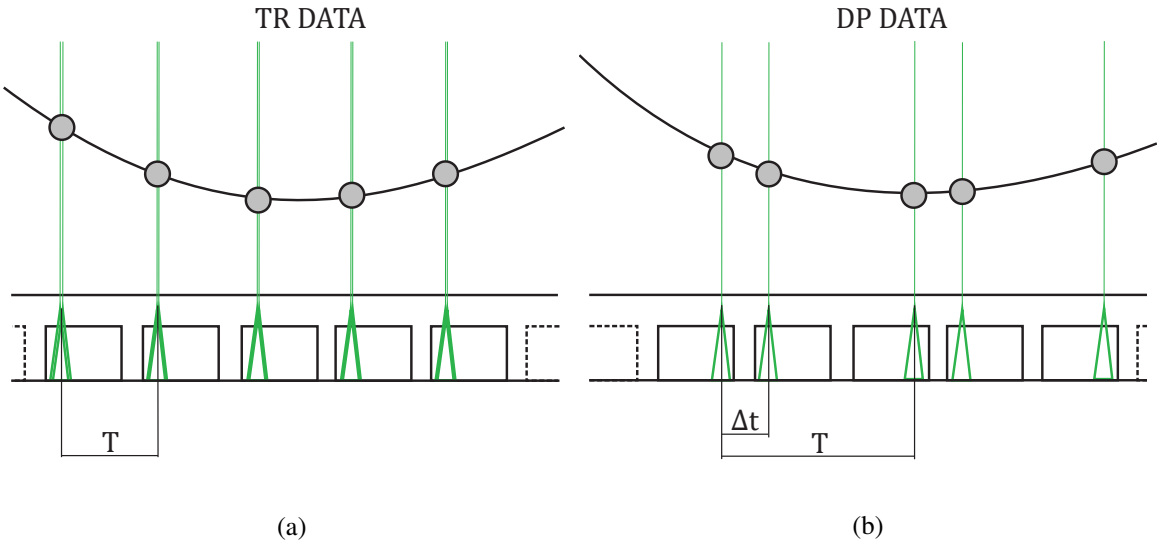

Figure 3.1: Comparison between data obtained by TR(a) and DP-DF (3.1b) acquisitions.

An example of an application of the DP-DF strategy to 3D flow investigation is the work done by Cornic et al. (2014). In this work, after a sparse tomographic reconstruction, particles are matched between frames to evaluate the velocity field with an algorithm that compares the possible 3D matches with the 2D motion in each camera.

In order to increase the measurement dynamic range, limited for DP-DF strategies, as explained in the next section, multi-pulses approaches have been developed. Examples of multi-pulses approaches are presented in the works done by Schroder et al. (2013) and Lynch and Scarano (2014). In both of them, multiple imaging and illumination systems have been used simultaneously, while different strategies to separate imaged particles from subsequent pulses have been considered. In

[1]Hereafter referred as DP-DF approach

Lynch and Scarano (2014), for example, in order to perform this task, the usage of three independent tomographic systems, with a minimum number of nine cameras, is presented. If an industrial application is considered, the high number of cameras becomes a bottleneck, due to the needed long calibration processes and the large optical access required. In order to reduce the number of cameras needed, a possible solution is the adoption of polarised illumination, as proposed by Schroder et al. (2013), at the cost of a higher complexity of the system.

Furthermore, both mentioned works are based on tomographic reconstruction and cross-correlation analysis, with the computational burden associated with them.

As seen before, STB, 3D-PTV algorithm, can produce great results in terms of accuracy and computational cost (Schanz et al., 2016; Schröder et al., 2015). For this reason, recently, the possibility to apply STB to multi-pulses data have been investigated and presented by Novara et al. (2016). In order to cope with the lack of a long sequence of TR particles positions, the algorithm has been adapted by adding an iterative process for the tracking phase, during which *tracks candidates* are built and classified w.r.t. their average deviation from a first-degree polynomial fit. The data analysed with this algorithm are produced by a system that consists of two different imaging systems, each of them acquiring in DP mode. Besides, with two light sources polarised along directions that differ by 90° are used to illuminate the seeding. In order to avoid multi-exposed images, the cameras are equipped with polarising filters rotated by 90°. The entire system is schematically represented in Fig.(3.2), where different colours represent different polarisation. The results shown by Novara et al. (2016) are encouraging and demonstrate the ability of the presented system to cope with high Reynolds number at particle concentration similar to the one characteristic of Tomo-PIV, ppp = 5%.

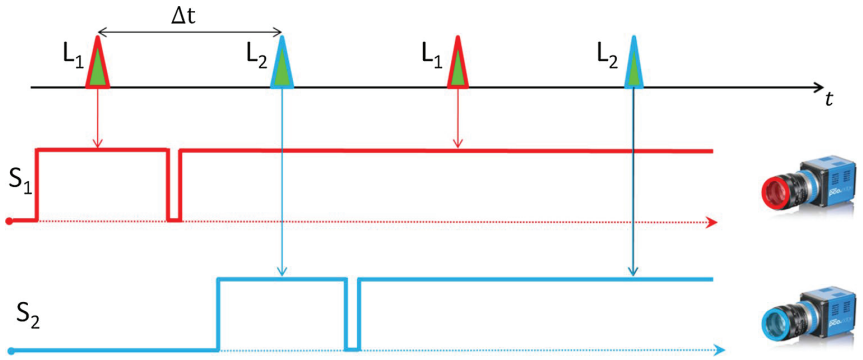

Figure 3.2: Acquisition strategy presented by Novara et al. (2016).

Even if the complexity of the setup proposed by Novara et al. (2016) is reduced compared with the one used by Lynch and Scarano (2014), two distinct imaging and illumination systems are required. As introduced before, for industrial applications, requirements in terms of complexity, measurement volumes and optical access are usually more strict than the ones characteristic of the research environment. For this reason, it has been considered an advancement the idea of coupling the simplicity of the setup, peculiarity of the Robotic PIV system, with an acquiring and processing strategy able to cope with flow velocities typical of industrial applications.

3.2 Robotic Volumetric PIV: DP-DF measurement and coaxial error

As seen in the previous sections, to cope with high flow velocities, standard PTV algorithms are limited by the state-of-the-art of the hardware, more precisely, by the maximum acquisition frequency achievable. For this reason, several multi-pulses techniques have been developed, able to cope with high speed flows, at the price of losing the ability to use temporal information as done for TR data. However, all the strategies evaluated in the last section have in common the high setup complexity, a factor that makes them not particularly suitable for industrial applications.

If the experiment done by Jux (2017), using the Robotic PIV system, is considered, a free-stream velocity U_∞ = 14 m/s was analysed with an acquisition frequency f = 748 Hz, maximum frequency achievable by the state-of-the-art of the Robotic PIV system. In that case, the particle displacement in the free-stream varies from 78 px, at 20 cm from the cameras, to 25 px, at 60 cm from the cameras, with the former closer to the limit of 80 px. This has been the starting point of this project.

As first step, the possibility of coupling a DP-DF acquiring strategy with the Robotic PIV system has been evaluated. Since the beginning, possible advantages and disadvantages of this methodology were clear. The ability to cope with high velocity flows is obtained at the cost of a lower achievable DVR. However, the most critical issue is given by the uncertainty along the coaxial direction, proper of the Robotic PIV, that would affect a single DP-DF measurement dramatically, as it is shown in this section.

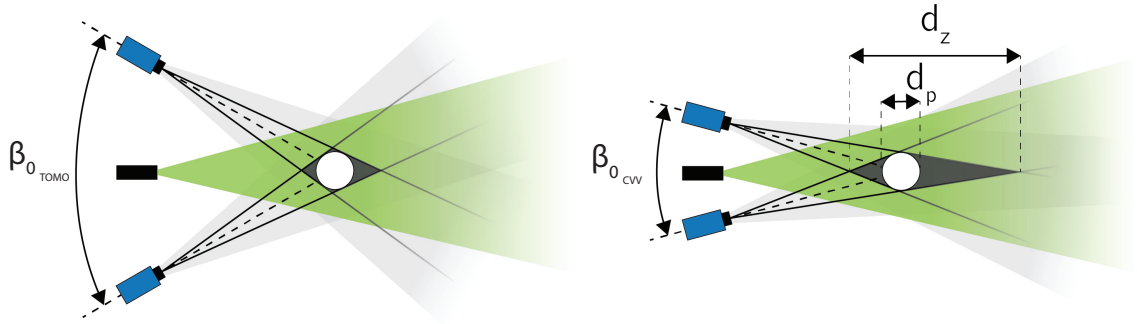

(a) (b)

Figure 3.3: In-depth uncertainty introduced by the low tomographic aperture β. True particle depicetd in white, reconstructed particle shown in black. Figure reproduced from Giaquinta (2018).

If a particle is imaged at the center of the sensor by two systems with different tomographic aperture, the situation depicted by Fig.(3.3) is obtained. If a simple geometry analysis is performed, it is possible to relate the reconstructed particle diameter d_z with the true particle diameter d_p through the equation:

$$\frac{d_p}{d_z} \approx \sin(\frac{\beta}{2}) \tag{3.3}$$

that leads to the fact that the reconstructed particle diameter can be calculate approximately as:

$$d_z \approx \frac{2}{\beta} \cdot d_p \tag{3.4}$$

for $\beta \ll 1$ rad.

For what concern the determination of d_p, since the optical magnification varies between 0.1 and 0.02, the image particle size is diffraction dominated, with a value that is rather constant along the measurement domain. In condition similar to the ones of the tests performed during this project, the diffraction limit is higher than the distance between glares points, so that the particle image size can be approximated by the function:

$$d_\tau = 2.44 \ \lambda \ (1 + M) \ f_\# \tag{3.5}$$

From Eq.(3.5), if $f_\# = 8$, an image particle diameter equal to $d_\tau = 10.38 \ \mu m$ is obtained. Knowing that the sensor pitch is equal to 4.8 μm, $d_\tau^* = 2.16 \ px$, that, after the reprojection in the real space, becomes $d_{p_{reproj}} \approx 1 \ mm$.

Furthermore, as described by Adrian (1991), it is possible to estimate the order of magnitude of the uncertainty on the particle position according to:

$$\varepsilon_x = c_\tau d_\tau = 0.1 \ mm \tag{3.6}$$

where c is a parameter depending on the system used and d_τ is the image particle diameter. Consequently to Eq.(3.4), the uncertainty on the particle detection along the in-depth direction is dependent on the tomographic aperture, according to the equation:

$$\varepsilon_z = \frac{2}{\beta} \cdot \varepsilon_x \tag{3.7}$$

that leads to a value equal to:

$$\varepsilon_z = 2.86 \ mm \tag{3.8}$$

if $c_\tau = 0.1$ and $\beta = 4°$.

Moreover, if regions further from the cameras are considered, the in-depth accuracy also decreases due to the smaller aperture between the lines of sight, as demonstrated and measured by Schneiders (2017). Furthermore, ε_z is not constant along the in-plane directions, decreasing with the increase of the distance from the z-axis of the cameras, as shown by Schneiders (2017). Usually, if TR data are acquired and analysed with STB, the negative effect brought by this uncertainty is mitigated by the use of temporal information, that permits a fitting through positions obtained at subsequent time-steps.

On the contrary, for DP-DF acquisitions, due to the magnitude of T, no temporal information is available and at each time-step the particle pairing affected by ε_z, as shown by Fig.(3.4).

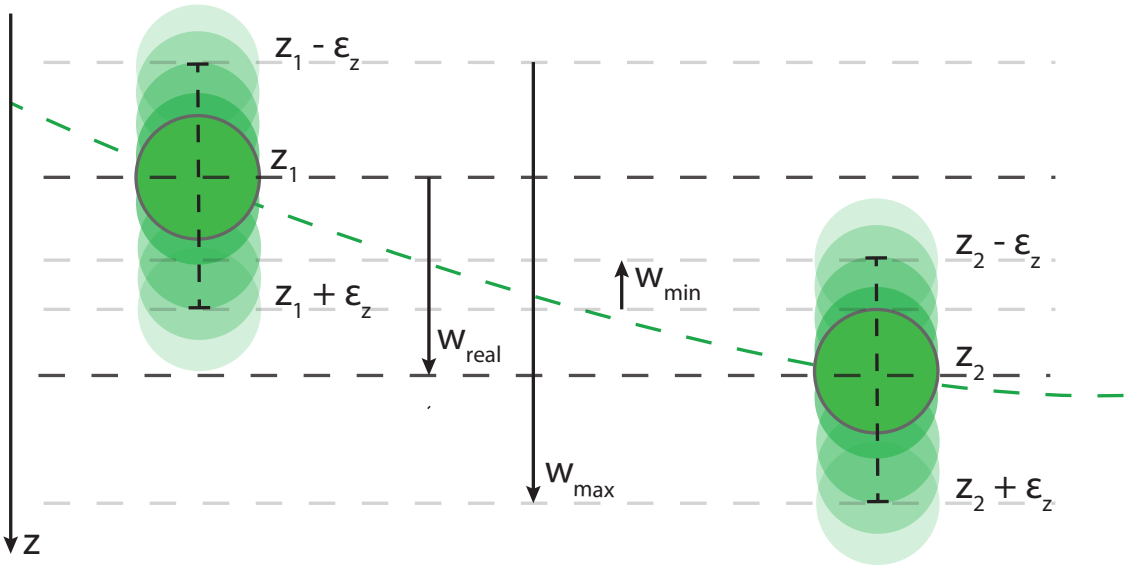

Figure 3.4: Uncertainty on velocity evaluation from DP-DF acquisition by Robotic PIV.

If particles detected with a in-depth uncertainty equal to ε_z are paired across a time-step equal to Δt, the measured in-depth velocity w_{meas} varies in the interval:

$$\frac{(z_2 - \varepsilon_z) - (z_1 + \varepsilon_z)}{\Delta t} \leq w_{meas} \leq \frac{(z_2 + \varepsilon_z) - (z_1 - \varepsilon_z)}{\Delta t} \tag{3.9}$$

that leads to:

$$w_{true} - \delta_w \leq w_{meas} \leq w_{true} + \delta_w \tag{3.10}$$

where $w_{true} = \frac{(z_2 - z_1)}{\Delta t}$ is the true value of the velocity and $\delta_w = \frac{2\varepsilon_z}{\Delta t}$ is the maximum absolute error on the velocity determination. From the uncertainty on the particle position estimation along the in-depth direction ε_z, it is possible to evaluate the relative measurement uncertainty of the particle displacement estimation for a DP system using the equation:

$$\varepsilon_w = \frac{\varepsilon_z \sqrt{2}}{\Delta z} = \frac{\varepsilon_z \sqrt{2}}{w \Delta t} \tag{3.11}$$

From Eq.(3.11), it is clear that a larger pulse separation time is beneficial for what concerns the accuracy of the measurement. However, as reported by Boillot and Prasad (1996), there are multiple sources of error in a PIV measurement. Between them, two different kinds of error directly depend on the Δt: the *random error*, expressed by Eq.(3.6), and the *truncation error*, given by the acceleration of the flow. Their dependence on Δt is schematically represented in Fig.(3.5a). In this study, between the two mentioned kinds of error, only the random error has been considered, neglecting the truncation error. The valuation of its importance w.r.t. the kind of measurements performed in this project can be indicated as one of the suggested future work

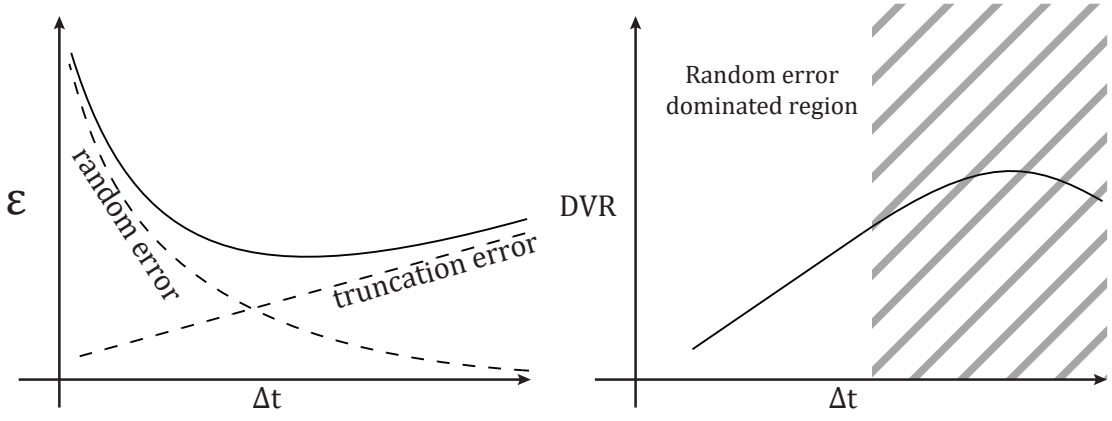

Figure 3.5: Schematic representation of: (a) error on velocity measurement given by *random error* and *truncation error* and (b) considered region in the Δt domain.

Considering a range of Δt for which the assumption on the truncation error is valid, it is possible to obtain the situation depicted by Fig.(3.5b), where is schematically represented the dependence of the DVR on the Δt. For larger pulse separation time, the DVR increases linearly with it. However, if a PTV approach is considered, the pulse separation time Δt has to be limited to assure a robust pairing, limiting spurious bounds that would affect the final velocity measurement. As reported by Maas et al. (1993), if a simple nearest-neighbour pairing algorithm is considered, the percentage of success pairing is close to 100% for synthetic data, with a particle displacement $\Delta x = c\ \bar{r}$, where $\bar{r}$ is the mean inter-particle distance and $c = 0.2$. Since this result is obtained from synthetic data, in this project, the maximum particle displacement allowed for a standard DP-DF measurement has been set to $\Delta x = 0.1\ \bar{r}$. In order to calculate the inter-particle distance, the following formula has been used:

$$\bar{r} = \left(\frac{1}{C_{HFSB}}\right)^{\frac{1}{3}} = 15.66\ mm \tag{3.12}$$

where $C_{HFSB} = 0.26\ cm^{-3}$ as calculated in Chapter 4. This leads to a maximum particle displacement of $\Delta x = 1.6$ mm, that, with a free-stream velocity $U_\infty = 12\ m/s$, corresponds to a maximum time-step of $\Delta t_{max} \approx 130\ \mu s$. If the uncertainty given by Eq.(3.8) is considered with a time-step equal to $\Delta t = 120\ \mu s$, the following uncertainty on the velocity is obtained:

$$\delta_w = \frac{0.00572}{0.00012} \approx 48\ m/s \tag{3.13}$$

It must be remarked that the value obtained by Eq.(3.13) is 400% of U_∞, making the solution unacceptable, as demonstrated furthermore by the result of Eq.(3.16). If the velocity distribution, in the interval given by Eq.(3.10), is hypothetically considered as a normal distribution with the value given by Eq.(3.13) being the correspondent 99% value, it is possible to estimate the standard

deviation of the velocity through the equation:

$$\sigma_w = 0.3\ \delta_w \approx 16 \text{ m/s} \tag{3.14}$$

Consequently, if $w = 10\ m/s$ is considered, it is possible to evaluate the number of uncorrelated samples required for obtaining a prefixed level of uncertainty on the mean flow. If an uncertainty on $\overline{w}$, $\varepsilon_{\overline{w}}$, of 5% is aimed, the following equation can be used:

$$\varepsilon_{\overline{w}} = \frac{2\sigma_w}{\sqrt{N_w}} \tag{3.15}$$

$$N_w = \left(\frac{2 \cdot 48}{0.05 \cdot 10}\right)^2 \tag{3.16}$$

finding a required number of uncorrelated samples equal to $N_w \approx 3 \cdot 10^4$.

If the pulse-separation time increases, subsequently the DVR increases and N_w decreases, therefore being beneficial for the accuracy of the system. However, as explained before, the probability of wrong pairing increases, affecting the final results.

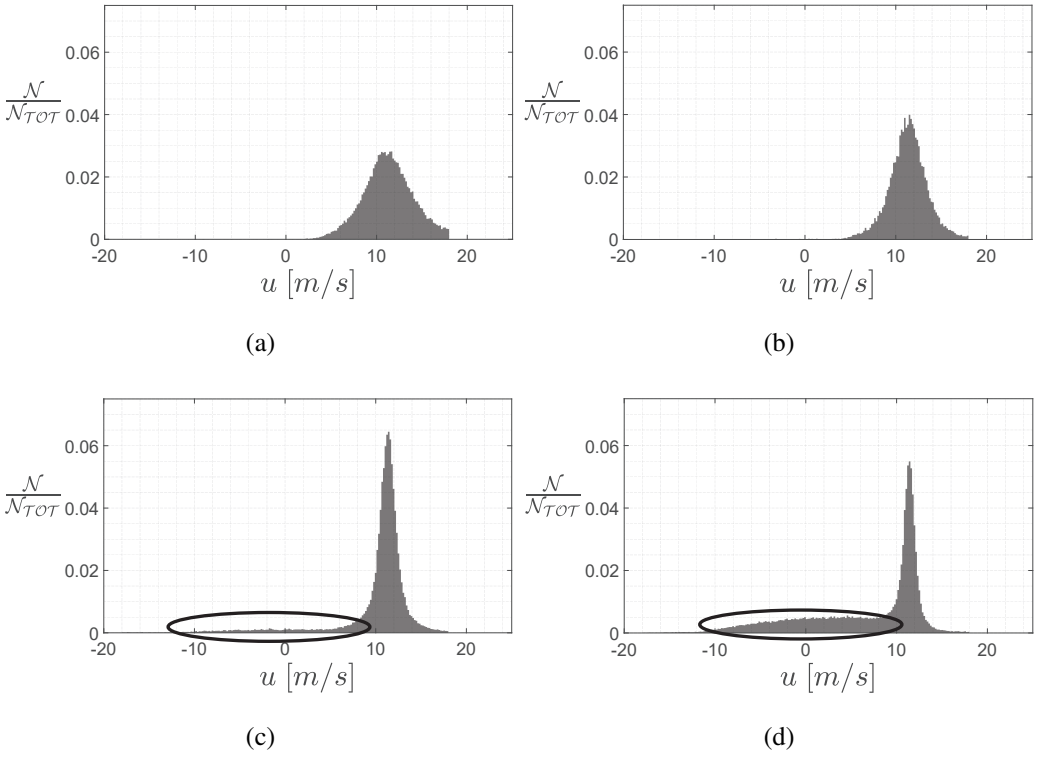

Figure 3.6: Distribution of the u component of the velocity in a $20 \times 20 \times 20$ cm^3 portion of the free-stream region for different pulse separation times: (a) 122 μs, (b) 244 μs, (c) 366 μs and (d) 610 μs. Free-stream velocity: $U_\infty = 12$ m/s.

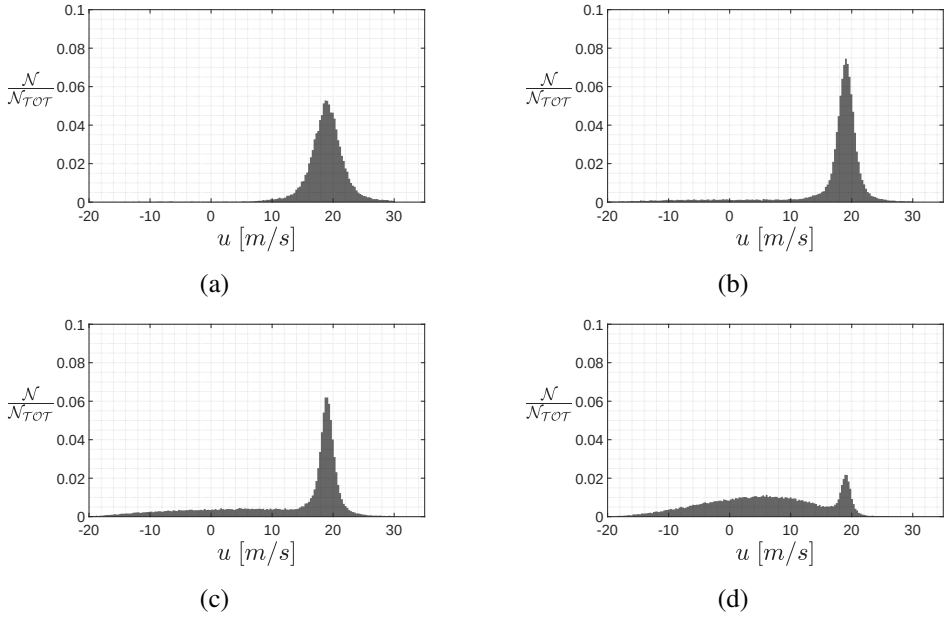

Figure 3.7: Distribution of the u component of the velocity in a $20 \times 20 \times 20$ cm^3 portion of the free-stream region for different pulse separation times: (a) 122 μs, (b) 244 μs, (c) 366 μs and (d) 610 μs. Free-stream velocity: U_∞ = 20 m/s.

This effect can be seen in Fig.(3.6), where the distribution of the u component of the velocity is shown for different pulse separation times Δt. The volume considered is a $20 \times 20 \times 20$ cm^3 portion of a free-stream region with U_∞ = 12 m/s, labelled A in Fig.5.1. With the increase of Δt, two distinct effects are visible. Firstly, due to the longer displacement measured, the uncertainty on the velocity determination reduces, as the thinner and taller gaussian distribution testifies. However, as shown in Fig.(3.6c) and Fig.(3.6d), the increase of the displacement causes spurious paring, leading to the appearance of noise underlined by the black ellipse in the figures. As it is shown in Chapter 5, the application of the designed method permits to obtain a distribution similar to the one presented by Fig.(3.6d), however without the noise given by the spurious pairs.

Fig.(3.7d) shows the velocity distribution in the same volume and for the same pulse separation times when the velocity is ramped up to 20 m/s. Noticing the same behaviour mentioned before is possible. However, due to the higher speed, if Δt = 610 μs is considered, Fig.(3.7d), the pick of the Gaussian distribution around the expected values drops. Furthermore, the signal to noise ratio, defined here as the ratio between the highest value of the Gaussian distribution around the expected value and the highest value of the Gaussian distribution of the noise, drops approximately to 2.

Furthermore, the effect of increasing the pulse separation time can be seen in Fig.(3.8) and Fig.(3.9), where the percentage of correct pairing is shown varying Δt at, respectively, U_∞ = 12 m/s and U_∞ = 20 m/s. For both the cases, the analysis has been performed in the same volume considered before, a $20 \times 20 \times 20$ cm^3 portion of a free-stream region, and only the main component has been considered. In order to build up a reference, the following procedure has been

followed. Knowing that the probability of spurious pairing increases with Δt, for this purpose, only the acquisitions performed with the lowest Δt, between the ones described in Chapter 4, have been considered, respectively, $\Delta t = 122\ \mu s$ for the $U_\infty = 12$ m/s case and $\Delta t = 61\ \mu s$ for the $U_\infty = 20$ m/s case. Analysing all the 8000 images as described in Sec.(3.3.1), with a final ensemble average done with cubic elements with $\Delta_x = 20$ mm, an average velocity $\overline{u}$ has been calculated and considered as reference velocity for the considered volume. At this point, for each Δt, the velocities of all the instantaneous pairings obtained in the same volume are compared with the reference, defining correct a pairing if:

$$\left|\frac{u}{\overline{u}} - 1\right| < \alpha \ \ \& \ \ \frac{u}{\overline{u}} > 0 \tag{3.17}$$

where $\alpha = [0.1, 0.2, 0.3, 0.4, 0.5]$, that corresponds to allow a discrepancy between the instantaneous value and the reference of an amount that varies between 10% and 50% of the particle displacement. For each case, the ratio between the expected averaged displacement and the mean particle distance is evaluated. The expected particle displacement is evaluated by multiplying the velocity $\overline{u}$ with the pulse separation correspondent to the considered case. On the contrary, $\overline{r}$ is evaluated for each case using Eq.(3.12) for the entire considered volume. As introduced before, the results in term of correct pairing are shown in Fig.(3.8) and Fig.(3.9) as a function of the Δt, and in Fig.(3.10) and Fig.(3.11) as a function of the particle displacement Δx normalized with the mean particle distance $\overline{r}$.

A first observation can be made by analysing the two graphs. As expected, it is noticeable the effect of Δt on the accuracy of the measurement. Indeed, if the results that correspond to $\alpha = 0.1$ are considered, initially, the percentage of good pairing increases for larger displacements, and consequently, for larger time-steps. However, it is also clear that this increment of accuracy is stopped when the displacement becomes too large and spurious pairing appears, condition reached for $\Delta t = 366\ \mu s$, that corresponds to $\frac{\Delta x}{\overline{r}} \approx 0.3$, for $U_\infty = 12$ m/s and for $U_\infty = 20$ m/s. These limits are evaluated by selecting the first measured time-step for which the percentage of pairing, considering $\alpha = 0.5$, becomes lower than 90%. These results confirm the expectation that, for what concerns the pulse separation time of a DP acquisition, an upper limit exists.

At this point, the reasons behind the impossibility of applying a standard DP-DF acquisition strategy with the Robotic Volumetric PIV setup are revealed. The high requirements in terms of particle displacement to counterbalance the uncertainty along the coaxial direction are in contrast with the requirements in terms of pulse separation time for a correct pairing. For this reason, in the next section, a method is proposed to permit an increase of Δt, exceeding the limits underlined in this section, without affecting the percentage of success pairing thanks to the adoption of a velocity predictor.

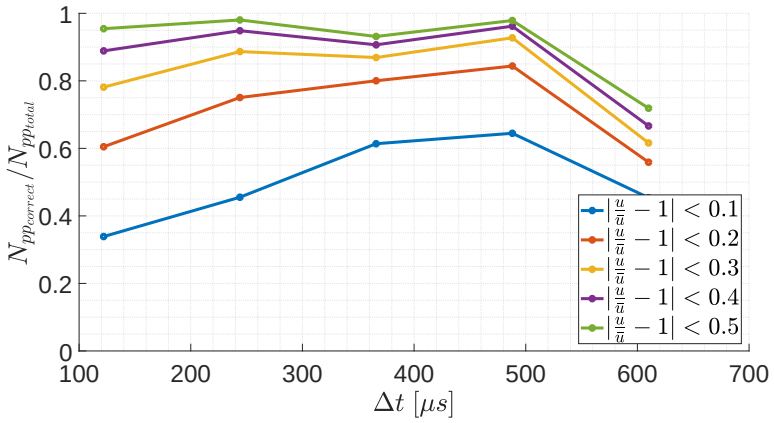

Figure 3.8: Percentage of correct pairing considering a free-stream region of 20x20x20 cm^3 varying the pulse separation Δt, with a free-stream velocity U_∞ = 12 m/s.

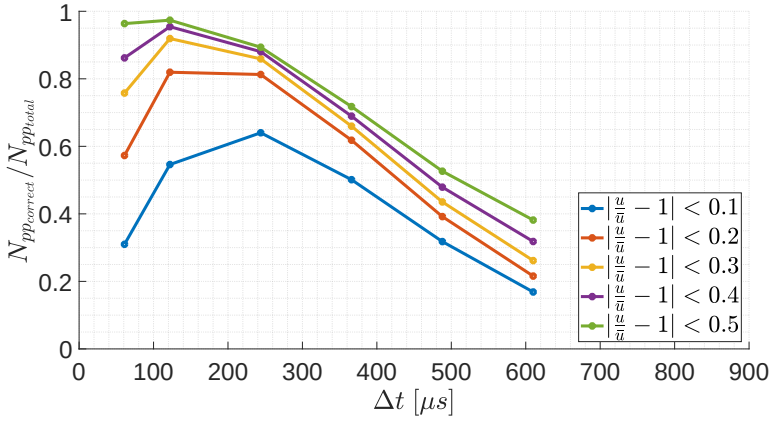

Figure 3.9: Percentage of correct pairing considering a free-stream region of 20x20x20 cm^3 varying the pulse separation Δt with a free-stream velocity U_∞ = 20 m/s.

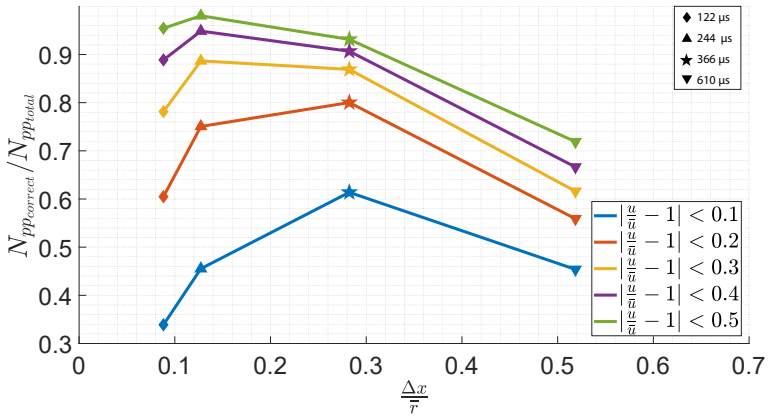

Figure 3.10: Percentage of correct pairing considering a free-stream region of 20x20x20 cm^3 as a function of the parameter $\frac{\Delta x}{\bar{r}}$, with a free-stream velocity U_∞ = 12 m/s.

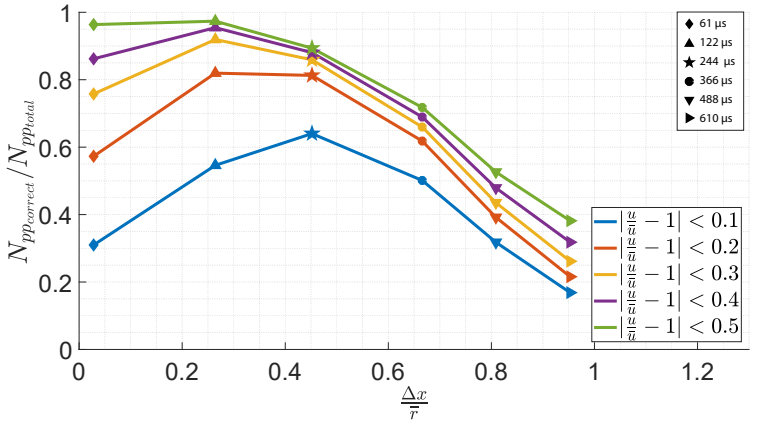

Figure 3.11: Percentage of correct pairing considering a free-stream region of 20x20x20 cm^3 as a function of the parameter $\frac{\Delta x}{\bar{r}}$, with a free-stream velocity U_∞ = 20 m/s.

3.3 Multi-Δt, DP technique

As seen in the previous section, an increase of Δt is beneficial for the accuracy of the measurement, up to the point where incorrect pairing and truncation error (Boillot and Prasad (1996)) start to affect the quality of the velocity evaluation. The increase of the uncertainty on the particle position determination given by the low tomographic aperture of the Robotic PIV system leads to higher requirements in terms of particle displacement, as seen at the end of the last section. As seen in Chapter 2, several methods have been introduced in the last decades to increase the DVR of PIV measurements. In this project, inspiration has been taken from them to develop the method described in this chapter. In order to achieve the prefixed goal, a multi-Δt DP algorithm has been developed and implemented.

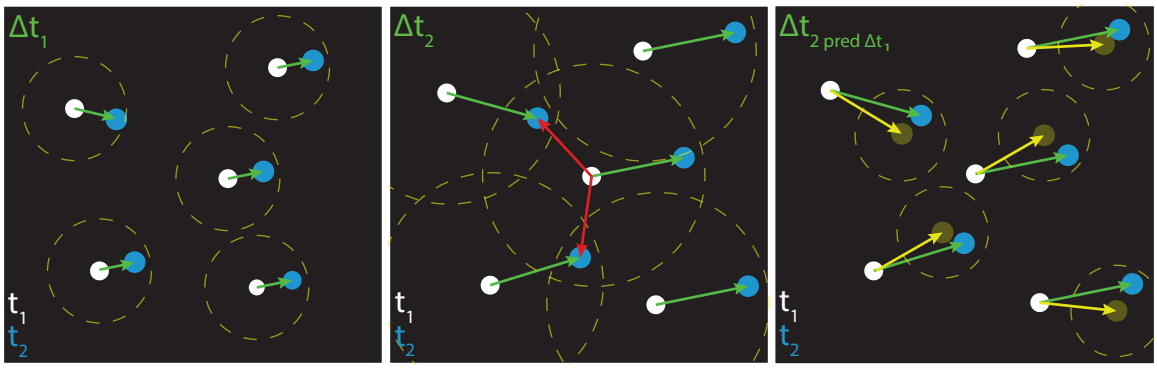

(a) (b) (c)

Figure 3.12: Nearest-neighbour bond assignment. (a) Situation in which $\Delta x \ll \overline{r}$: high probability of good pairing. (b) Situation in which $\Delta x \approx \overline{r}$: the probability increases with the pulse separation time. (c) Nearest-neighbour algorithm with the implementation of a particle prediction.

The principle behind the algorithm is explained in Fig.(3.12), projected to a 2D plane for simplicity. Fig.(3.12a) shows a situation in which the displacement Δx between two subsequent time instances t_1 and t_2 is much lower than the mean particle distance $\overline{r}$. In this case, a simple NN algorithm with radius R_{s_1} can work, producing good pairing represented by the green arrows. As explained in detail in the previous section, if the Δt is increased up to the point in which $\Delta x \approx \overline{r}$, spurious pairings start appearing as shown in Fig.(3.12b), where red arrows represent the incorrect pairs. This result is given by the fact that the radius of research must be proportional to the particle displacement in order to be able to produce correct pairing. On the contrary, if a predictor is available, a particle position at t_2 can be extrapolated by the equation:

$$\vec{x}_{pred} = \vec{x}_1 + \vec{v}_{pred} \cdot \Delta t \tag{3.18}$$

At this point, a NN algorithm can be used, centred in $\vec{x}_{pred}$ and radius $R_{s_{2p}}$, in order to find the particle at t_2 that will be paired with the considered particle at t_1. The introduction of the prediction step is helpful for the system in two different aspects. Firstly, the percentage of correct pairing is enhanced for long Δt, as it will be seen in Chapter 5. Secondly, it permits the reduction of the radius

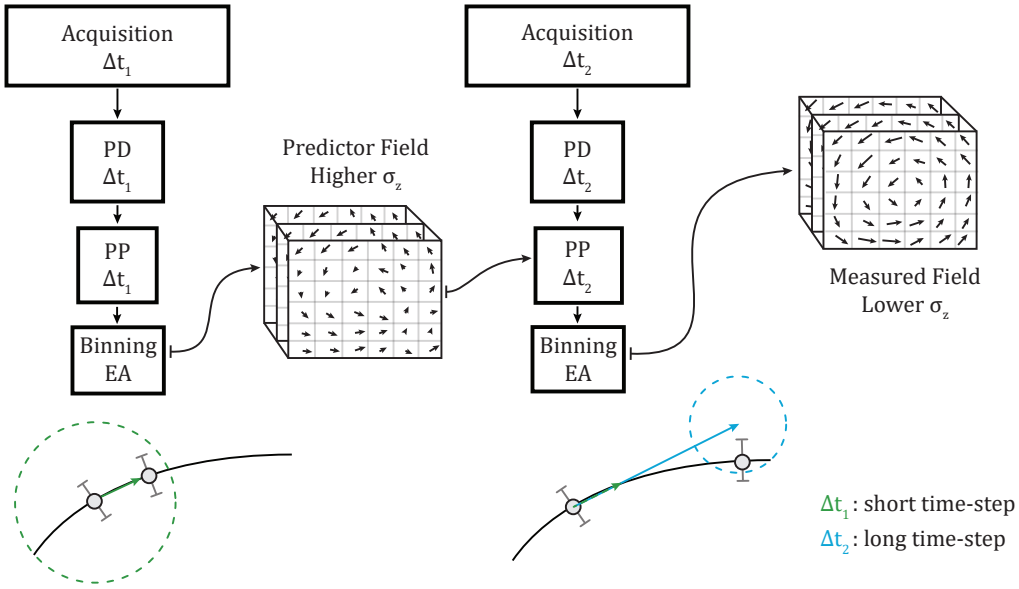

Figure 3.13: Flow chart of MDt-DP algorithm.

of search compared to the one prescribed for a standard DP-DF measurement, obtaining $R_{s_{2p}} < R_{s_2}$. This does not affect the accuracy of the results, since always the nearest particle will be selected, but decreases the computational cost since, for each particle, statistically, less possible pairs have to be evaluated. Based on this approach, a specific algorithm has been developed, whose workflow is described in Fig.(3.13). Its input is a set of raw or pre-processed images acquired by two DP-DF acquisitions, one with a short pulse separation time, $\Delta t = \Delta t_1$, and another one with a longer pulse separation time, $\Delta t = \Delta t_2$.

3.3.1 Short Δt acquisition

In order to build the predictor, a first DP-DF acquisition is performed with a small pulse separation $\Delta t = \Delta t_1$. The acquiring strategy has been already introduced before and is described in Fig.(3.1b). At this point, the data consist of raw images, which have to be pre-processed as discussed in Sec.(4.7.1). *Particle detection* represents the following step, hereafter referred as PD. As shown in Chapter 2, different methods have been developed to obtain 3D particle positions from 2D images. In this project, the advanced method presented by Wieneke (2013), IPR, has been chosen, for its advantages introduced in Sec.(2.3.2). The parameters used for this step are shown in Chapter 4. Having the raw or pre-processed images as input, the output of IPR is a list of particle positions for all the frames considered.

At this point, it is possible to perform the subsequent step, the *particle pairing*, hereafter referred as PP. In literature, for standard DP-DF acquisitions, several methods for particle pairing have been developed and presented. Some of the most common ones are the nearest neighbour, the relaxation

method and the neural network method, described by Pereira et al. (2006). If a single couple of frames, imaged at t and $t + \Delta t$, is considered, all the methods mentioned before are based on a particle distributions that can be represented as:

$$(\vec{x})_i^t = (x_i^t, y_i^t, z_i^t) \quad i = 1, \ldots, N_p^t \tag{3.19}$$

$$(\vec{x})_j^{t+\Delta t} = (x_j^{t+\Delta t}, y_j^{t+\Delta t}, z_j^{t+\Delta t}) \quad j = 1, \ldots, N_p^{t+\Delta t} \tag{3.20}$$

where N_p^t is the number of particles detected at the time-step t and $N_p^{t+\Delta t}$ indicates the number of particles found in the second frame of DP-DF acquisition, at time $t + \Delta t$. Every tracking procedure has the aim of selecting the correct link for each particle between one pulse and the following one. When the link is found, the velocity can be evaluated by using the following first-order finite difference method:

$$\vec{u}_{i,j} = \frac{(\vec{x})_j^{t+\Delta t} - (\vec{x})_i^t}{\Delta t} \tag{3.21}$$

In this project, due to its simplicity of implementation and lower computational cost, the NN algorithm has been selected as pairing method. From now on, in order to explain the used procedure, a single pair of subsequent frames will be considered, where $\vec{x}_i^1$ represents the position of the i-th particle in the first frame and $\vec{x}_j^2$ is the position of the j-th particle in the second frame. Furthermore, the set of all the points will be indicated as Λ_1 and Λ_2, respectively, for the first and second frame. After having detected all the particles in the first frame, each of them is considered singularly. In order to find the particle that has to be linked with the considered one, the NN algorithm uses a criterion based on the minimum distance, selecting j, so that is minimum the amount:

$$\ell_{i,j} = |\vec{x}_i^1 - \vec{x}_j^2| \tag{3.22}$$

where only particles from the second frame that satisfies the condition $|\vec{x}_i^1 - \vec{x}_j^2| < R_{s_1}$ are taken into account, as represented in a 2D form in Fig.(3.14). It is important to notice that the choice of R_{s_1}, as soon as one particle falls into the sphere centred in $\vec{x}_i^1$, does not affect the accuracy of the method, but only the computational cost, varying the number of links that have to be measured and compared. For the analysis of the short pulse separation acquisition, a search radius equal to $R_{s_1} = 2U_\infty \Delta t_1$ is used.

Summarizing the procedure, these are the steps that have been implemented for the PP step:

1. All the particles from the first frame are sorted along the main direction of the flow
2. Considering singularly each particle of the first frame, the particles from the second frame, for which $|\vec{x}_i^1 - \vec{x}_j^2| < R_{s_1}$ is satisfied, are extracted. They form the cloud of points Υ_i
3. For all the particles of Υ_i, $\ell_{i,j}$ is evaluated
4. $\vec{x}_j^2$ for which $\ell_{i,j}$ is minimized is found
5. The velocity is evaluated using Eq.(3.21)
6. $\vec{x}_i^1$ and $\vec{x}_j^2$ are removed, respectively, from Λ_1 and Λ_2 in order to avoid multiple pairings of the same particle

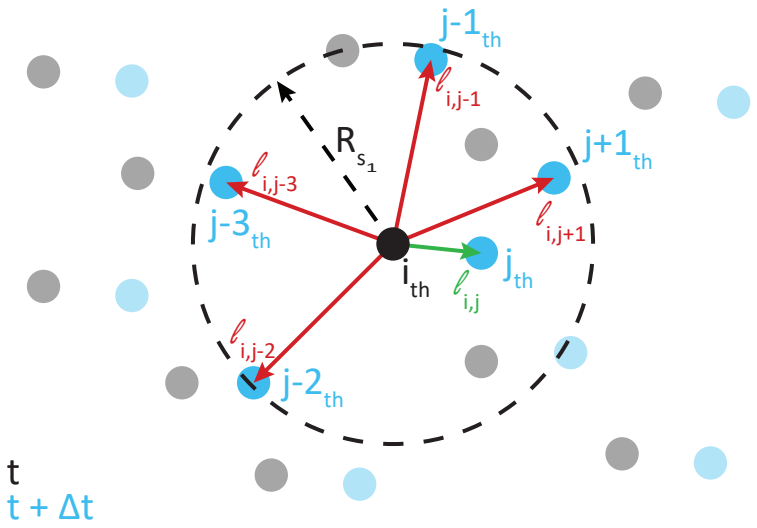

Figure 3.14: Pairing of a single particle of the first frame of a DP-DF acquisition.

7. Finally, the velocity vector is linearly shifted in the position $\vec{x}_{i,j} = \frac{\vec{x}_i + \vec{x}_j}{2}$

This procedure is repeated for $\forall\ \vec{x}^k \in \Gamma_k$ where $k = 1 \ldots N$, with N being the number of acquired pairs of images.

The result of this process is a set of particle positions $\vec{x}_{pp}$ and correspondent velocities $\vec{u}_{pp}$ obtained by each of the image pairs analysed. It must be remarked that, at this point, the information is kept at the particle position, not being structured or equally distributed in the volume. For this reason, in order to produce a predictor field usable for the measurement acquired with $\Delta t = \Delta t_2$, the sparse and unstructured information has to be transferred to a structured grid, through the step that hereafter will be referred as *binning*. This process can be achieved in different ways, for example, through interpolation or ensemble averaging. In this case, due to its lower computational cost and its simplicity of implementation, the ensemble average technique has been chosen. Agüera et al. (2016) is an example of recent work about different ensemble averaging methods dedicated to 3D-PTV. From it, it has been taken the inspiration for the Gaussian filter used in this work, an ensemble weighted average in a volume, or bin, that considers all the particles are passing through the volume during the entire acquisition.

Firstly, the entire measurement volume is divided into small cubic cells, or bins, whose centroids will be the vertices of the isotropic structured grid. The choice of a cubic cell is given by its simplicity, however, in the presence of strong gradients, such as for what concerns boundary layer flows, the usage of anisotropic cells, with the related increase in resolution in one specific direction, can be beneficial for the final results. Similarly to what usually done with PIV, it has been implemented the possibility of overlapping adjacent bins for a certain amount, in order to increase the spatial resolution of the generated grid. In order to assign a velocity to any of the centroids of the grid, two steps have to be done.

Initially, all the resultant particles, whose positions and velocities are given by $\vec{x}_{pp_1}$ and $\vec{u}_{pp_1}$,

are poured into the bins of the structured mesh. This step is performed through a binary search algorithm that finds the particles that fall into each bin. At this point, it is possible to calculate each velocity components that would be assigned to the centroid of the i-th bin through the weighted average:

$$\bar{u}_i = \frac{1}{\sum_{n=1}^{N_p} k_n} \sum_{n=1}^{N_p} k_n (u_i)_n \tag{3.23}$$

$$\bar{v}_i = \frac{1}{\sum_{n=1}^{N_p} k_n} \sum_{n=1}^{N_p} k_n (v_i)_n \tag{3.24}$$

$$\bar{w}_i = \frac{1}{\sum_{n=1}^{N_p} k_n} \sum_{n=1}^{N_p} k_n (w_i)_n \tag{3.25}$$

where:

$$k_n = \exp\left(-\frac{||x||^2}{(\Delta_x/2)^2}\right) \tag{3.26}$$

with $||x||$ being the Euclidean distance of the particle from the cell centroid, N_p the number of particle in i-th cell and Δ_x the cell edge. From this, for each bin, it is also possible to evaluate the weighted standard deviation for each velocity component as:

$$\sigma_{u_i} = \sqrt{\frac{1}{\frac{N_p - 1}{N_p} \sum_{n=1}^{N_p} k_n} \sum_{n=1}^{N_p} k_n \left((u_i)_n - \bar{u}_i\right)^2} \tag{3.27}$$

where the number of non-zeros weights corresponds to the number of particles due to the definition given by Eq.(3.26). The choice of a Gaussian weighting for the mean and standard deviation calculations has been made based on a trade-off between computational efficiency and accuracy of the averaging approach.

If a lower computational cost is required, the Gaussian filter can be substituted with a top-hat filter, assigning to all the particles the same unitary weight. However, as reported by Agüera et al. (2016), this lowers the accuracy of the averaging approach. Furthermore, between the mentioned approaches, another difference has to be highlighted. Due to the Gaussian weighting, given to the particles, based on the Euclidean distance, the effective particle density in each bin is reduced, requiring more samples to reach convergence.

Even if the robustness of the system is high, it is possible that spurious vectors, given by the tracking of ghost particles or tracking of strong noise, survive until the binning process. For this reason, an outlier detection filter that acts during the binning process. Jux (2017) reports a test on several types of filters, finally suggesting the usage of a mean filter. In the present work, the

suggestion is followed, and a mean filter has been added to the binning script. Hereafter, the working principle of the filter is explained. For each bin, when all the particles that fall in it are found, firstly the average and the standard deviation are calculated. Then, only the particles whose velocity is inside the range $u_n = \bar{u} \pm k\sigma_u$, with k=3, are taken into consideration for that specific bin. It must be remarked that, due to the overlap between bins, one particle could be excluded from one bin by the filter, while being still acceptable in another one. This is a situation that can happen in regions of strong shear, for example.

At this step of the algorithm, the instantaneous particle positions and velocities obtained by the acquisition with short Δt have been converted into an averaged velocity field, with the information localized on the vertexes of a structured grid.

3.3.2 Long Δt acquisition

After having built the predictor field as explained in the previous section, the acquisition performed with the longer pulse separation time Δt_2 can be analysed. Also in this case, the particle detection is performed with IPR, using the same settings used for the short Δt acquisition. This is permitted since IPR does not use any temporal information, considering each quadruplet of images independently. Once the particle detection step is finished, the particle pairing starts.

As done before, for explanation purposes, hereafter, particles detected in a single pair of frames, with position $\vec{x}_i^1$, acquired at $T = t$, and $\vec{x}_j^2$, acquired at $T = t + \Delta t_2$, are considered. In order to exploit the availability of the predictor, firstly, the velocity field obtained by analysing the Δt_1 data is linearly interpolated to the particle positions of the first frame $\vec{x}_i^1$. Then, predicted particle positions at the subsequent time-step are evaluated with Eq.(3.18). As introduced before, a NN algorithm centred in $\vec{x}^2_{pred}$ is used to create the pairing. In this case, the search radius is set to be $R_{s_{2p}} = \frac{1}{3}R_{s_2} = \frac{2}{3}U_\infty \Delta t$. When all the particles of the first frame have been analysed, the subsequent pair of frames is considered and the procedure repeated. At the end of the PP step, the result is a set of particle position $\vec{x}_{pp_2}$ and velocities $\vec{u}_{pp_2}$ and the binning procedure described in the previous section is used to create the final velocity field.

3.3.3 Multiple cones analysis

The ability to scan large volumes proper of the Robotic PIV has been already introduced in Chapter 2. This is achieved by the translation of the velocimetry probe, that permits to measure multiple cones that can be afterwards stitched together in order to increase the measurement volume up to the desired dimension. The algorithm presented in this chapter has been designed in order to cope with multiple runs done in different positions. With an selection done by the user, each acquisition can be indicated as *predictor* or *predicted* w.r.t. another one. All the selected runs, where a run consists of a dataset of 8000 images, are then analyses accordingly. Finally, all the particle paired obtained from all the *predicted* runs are binned together using a global mesh, obtaining a velocity field in the entire scanned domain.

3.4 Δt SELECTION CRITERION

As described in this chapter, the proposed algorithm uses a short pulse interval to build a predictor that permits to increase the final Δt reducing the occurrence of false pairing. For this reasons, the choice of the two different Δt has to be made wisely.

For what concerns the shorter pulse separation, Δt_1, its choice is driven by the research of the lowest possible percentage of wrong pairings, selecting a pulse separation which ensures a particle displacement in the free-stream of $0.1\,\overline{r}$.

On the contrary, dealing with the longer Δt_2, a particle displacement in the free-stream equal to approximately 15 pixels has been targeted. In this case, the design choice of the longer Δt_2 is based on the free-stream velocity due to the expectation of no predominant cross-flows or different induces velocities. Similarly to the evaluations done for planar PIV, where the user has to select a proper Δt based on the out-of-plane or in-plane displacement, depending on the flow features, also for the presented method, similar appraisals have to be done.

CHAPTER 4

EXPERIMENTAL SETUP AND PROCEDURES

In order to prove the performances of the new proposed processing method a test campaign has been performed in the Open Jet Facility of the TU Delft. In this chapter, the apparatus of the demonstration test is described, with specific attention to the model description, the tunnel specifications and the Robotic PIV system specifications. The wind tunnel measurements are carried out with a simplified road vehicle model, a scaled version of the Ahmed body, to show the potential of the approach for car aerodynamics investigation. Different PIV measurements have been performed: TR, analysed with the state-of-the-art technique Shake-The-Box, and low speed MT-DP, post-processed with the new developed algorithm presented in Chapter 3. Finally, the processing procedures and the parameters used in the various steps are described.

4.1 Wind tunnel: OJF

In order to perform the described measurements of the wake of the Ahmed body, the model described in Sec(4.2) is placed in the Open Jet Facility at the High Speed Laboratories of TU Delft, shown in Fig.(4.1). This wind tunnel is a closed-loop, open test section with an octagonal exit of $2.85 \times 2.85\ m^2$. The contraction ratio is 3:1, with a horizontal contraction of 1.88 and a vertical one of 1.62. The test section is inserted in a room that spans 13 m wide and 8 m height, equipped at the end with a cooling mesh, not used in this experiment. The flow is accelerated by a fan driven by a 500 kW electrical motor up to 35 m/s; in this experiment the velocity ranges between 12 m/s and 20 m/s. Important factor of a wind tunnel is its nominal turbulence intensity, since it represents the amount of turbulence present into the free-stream, factor that affects the behaviour of the flow around the model. The nominal turbulence intensity of the OJF, as reported by Lignarolo et al. (2014) is 0.5%. However, as demonstrated by Jux (2017), the presence of the seeding rake inside the stream increases the turbulence intensity up to about 2%. In order to reduce the influence of the seeding rake, positioning it inside the settling chamber can help, as stated by Giaquinta (2018).

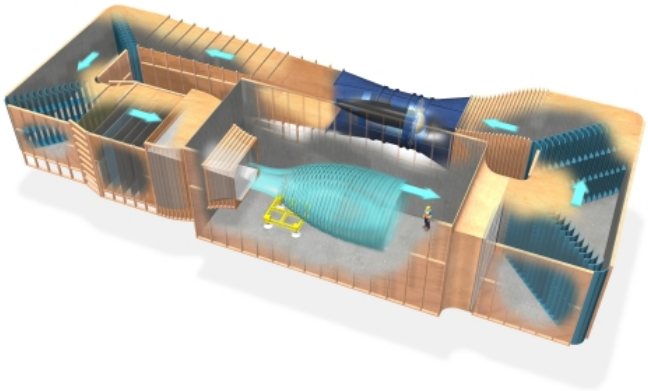

Figure 4.1: Schematic of Open Jet Facility. Reproduced from TU Delft (2017).

4.2 Test object: Ahmed body

As introduced in the first chapter, the Ahmed body appeared in 1984 and became a reference model for road vehicle aerodynamics. The model used in this test is a 50% replica of the original model introduced by Ahmed. The model is made out of wood and painted black in order to reduce reflections issues during the recording done for the PIV analysis. In order to verify the ability of measuring a complex flow system, the geometry has been selected to present vortical structures at the rear of the object. For this reason a rear equipped with a slant angle of 25° has been used. The dimensions are $522 \times 194.5 \times 144\ mm$, respectively, in length, width and height, with a slant length of 111 mm.

Fig.(4.2) shows shapes and dimensions of the described test object. As shown in the figure, the front part of the body is rounded, with a diameter of 100 mm. Four feet are attached to the body, which permit to have a ground clearance of 25 mm from the ground plate. This plate works as a raised floor which extends one characteristic length upstream of the body and three lengths downstream, featuring a rounded leading edge for boundary layer control purposes. In order to force transition to turbulent flow, zig-zig stripes have been positioned around the body just upstream of the front feet, permitting a qualitative comparison with the results presented in literature obtained with bigger scale models, 75% or 100%, at higher Reynolds number.

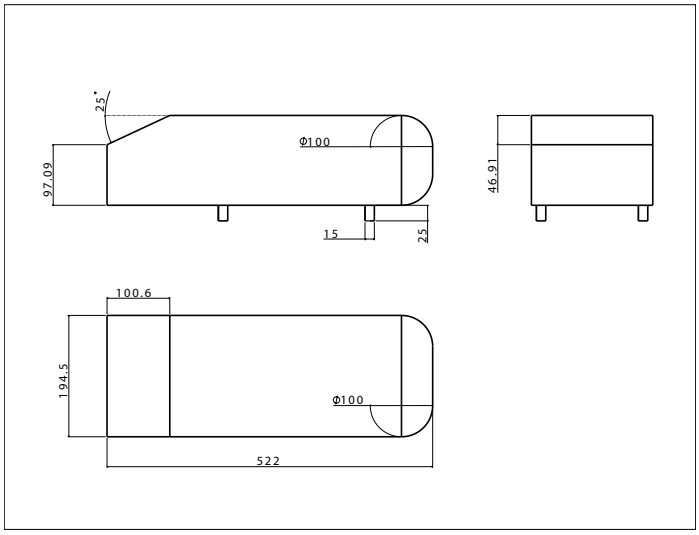

Figure 4.2: Ahmed body replica shapes and dimensions.

4.3 Seeding production and injection

As explained in the introduction, in order to measure the flow feature with PIV, it is necessary to introduce seeding into the stream that will be afterwords illuminated. The system that is used here in order to produce and release the bubbles is formed by two different elements: the seeding rake, where the nozzles are positioned, and the FSU (Fluid Supply Unit), tool that provides the required helium, soap and air at proper flow rates. The seeding rake used in this experiment has been designed and produced by the Aerodynamics Department of the TU Delft and it is the biggest rake ever used to author's best knowledge. It consists of ten parallel wings, each of them equipped with twenty nozzles, reaching a total amount of 200 nozzles. In each wing, four different lines are present: one for the air, one for the helium and two for soap, the delivery and the return. Each nozzle is linked to all the lines through capillaries of different diameter, depending on the fluid that has to pass. Finally, all these lines are in parallel connected to tubes coming from the FSU, which pumps all the fluids with a different pressure varied by pressure valves. This permits to vary the bubbles properties, namely the dimension and density, varying the relative pressures of all the fluid according to what needed. Increasing the helium flow rate, for example, can enlarge the bubbles,

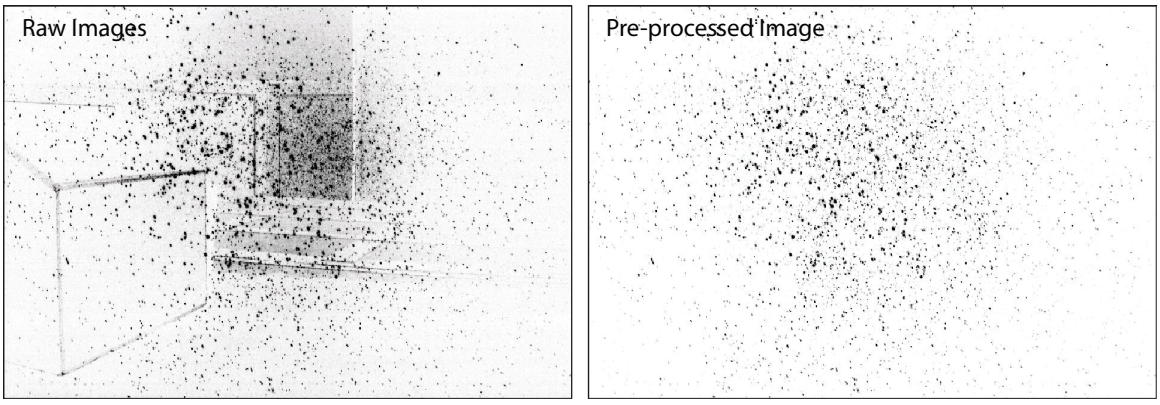

Figure 4.3: Comparison between raw image (inverted) and pre-processed image (inverted).

making them a bit lighter and increasing the amount of scattered light. The length of each wing is 1 m, leading to a spacing between two subsequent nozzles of 5 cm. Furthermore, the distance between two consecutive wings is 5 cm. For this reason, the area that is seeded by the rake is 0.95×0.50 m^2, not taking into account the bubble spreading given by the local fluctuations of the flow. In order to quantify the working rate of the seeding rake a preliminary test has been performed, varying the imposed pressures and verifying the amount of working nozzles. This led to the conclusion that around 25 nozzles were clogged and other 25 were working occasionally. For this reason, in order to evaluate the nominal bubble concentration C_{HFSB}, 150 nozzles have been considered. Even if the production rate of a single nozzle in fully operational condition is around 30000 bubbles/s, being the considered rake a prototype, it is reasonable considers as average production rate of each nozzle equal to 10000 bubbles/s. From this, it is possible to calculate that, for each second, $N_{bs} = 1.5 \cdot 10^6$ bubbles are introduced in an area equal to the frontal area of the seeding rake. At this point, to evaluate the seeding concentration it is necessary to considered the free-stream velocity, which will transport downstream the bubbles. If $U_\infty = 12\ m/s$, it is possible to calculate the volumetric flow rate:

$$\dot{V}_s = A_F \times U_\infty = 4750 \cdot 1200 = 5.7 \cdot 10^6\ \text{cm}^3/\text{s} \tag{4.1}$$

quantity that indicates the volume in which N_{bs} are released every second. For this reason, it is possible to evaluate the bubbles concentration as the ratio between N_{bs} and $\dot{V}_s$:

$$C_{HFSB} = \frac{N_{bs}}{\dot{V}_s} = \frac{1.5 \cdot 10^6}{5.7 \cdot 10^6} = 0.26\ \text{bubbles/cm}^3 \tag{4.2}$$

This concentration can be considered as a theoretical one, since, for example, an assumption on the number of working nozzles has been done. Furthermore, the production rate of the seeder changes in time, since a starting period is needed before having all the nozzles active. For this reason, before any measurement, it has been waited for 120 seconds in order to permit the system to tend to operational conditions.

Fig(4.3) shows a typical raw image acquired during this campaign on the left, with the correspondent pre-processed image on the right. This image has been acquired with the FSU working

with the pressures 2.5, 2.0 and 2.0, for respectively, air, soap and helium, and presents a ppp of about 0.018, far lower then the upper limit imposed to have PTV working, equal to 5% ppp, as shown by Wieneke (2013). For this reason, the same pressures have been used during the entire campaign.

4.4 Robotic PIV system

In this section, the Robotic PIV system is presented in terms of hardware. As anticipated before, the system is made by two distinct element: the CVV probe and the robotic arm. Furthermore, details about the illumination system is given.

4.4.1 Velocimetry probe

The velocimetry probe used in this experiment is a *Lavision Minishaker S*, shown in Fig.(). With dimensions equal to $w \times h \times d = 13 \times 9 \times 8\ cm^3$, it contains four CMOS cameras Basler acA800-510um packed together, characterized by a maximum acquisition frequency of 511 Hz at full sensor. Each camera is equipped with a 4 mm Basler C125 lens, with possibility to vary the $f_\#$ between 1.8 and 16. In order to perform tomographic reconstruction or triangulation, a tomographic aperture is needed between the cameras; for this model, at 40 cm, it is measured to be $\beta_0 = 4°$. The cameras have a $800 \times 600\ px^2$ sensor, with a bit depth of 10 bits. The sensor pitch is equal to $\Delta_{px} = 4.8\ \mu m$, leading to a sensor dimension of $3.84 \times 2.88\ mm^2$. In order to control the cameras, the commercial software Davis 8.4.0 from LaVision GmbH has been used. For what concerns the timing of the cameras and their sync with the laser, a Programmable Time Unit (PTU) integrated in the acquisition PC has been used. For the current experiment, a relative aperture $f_\# = 11$ has been chosen, in order to have the entire measurement volume, that start approximately 25 cm from the lenses, in focus. Furthermore, being the free-stream $U_\infty = 12\ m/s$, the sensor has been cropped to $784 \times 431\ px^2$ in order to reach an acquisition frequency of 0.7 kHz, to permit the usage of STB without encountering tracking issues. In order to obtain the same volume measured, this cropping has been maintained also for the double-pulse acquisitions.

4.4.2 Illumination

In order to illuminate the measurement volume, the light produced by a high-speed laser is convoyed trough an optical fibre from the laser head to the velocimetry probe, conically expanded at that location by two consecutive spherical lenses. The light source used in the experiment is a $QuantronixDarwinDuoNd : YLF$ laser, whose light has a wavelength of $\lambda = 527nm$ and whose maximum power is 25 mJ, when both the cavities shoot simultaneously. The length of the fiber is 4 m, permitting to place the laser head quite far from the measurement region, avoid possible bubble contamination. In order to sync the laser with the cameras, it is triggered by the same PTU cited before. The frequencies at which the laser can work range between 0.2 kHz to 10 kHz. Fig(4.5) shows the coupling system, where the beam exiting from the laser head is focused into the optical fiber trough a 60 mm lens. Adjusting the distance between the lens and the beginning of the fiber permits to vary the solid angle of the cone at the exit of the fiber.

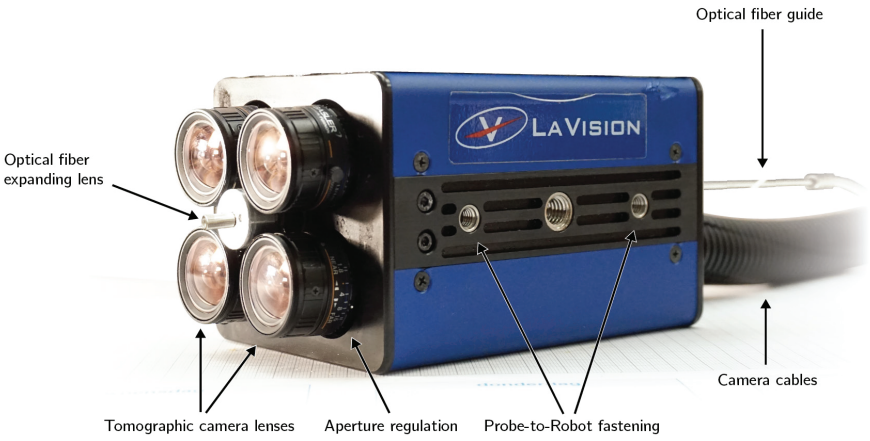

Figure 4.4: Coaxial velocimetry probe. Reproduced from Giaquinta (2018).

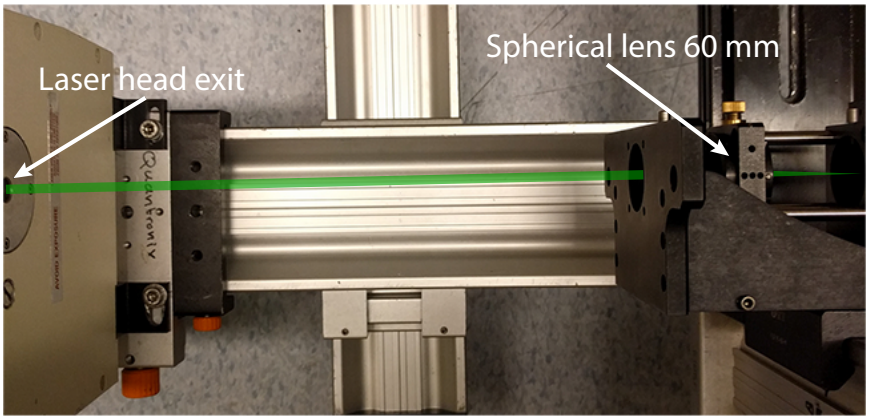

Figure 4.5: Laser coupling system.

4.4.3 Robotic actuation and robot control

One of the main element of the Robotic PIV system is the robot arm which permits to move freely the velocimetry probe in the measurement domain. In this experiment the robotic actuation has been performed by a `Universal Robot UR5` robotic arm, shown in Fig.(4.6) with its control tablet. This six-degree of freedom robotic arm has the ability of moving inside a spherical region of radius 85 cm, permitting to place and rotate the velocimetry probe as desired. At the end of the arm, the free extremity of the robot can be found, which will be referred as `tool` hereafter. At the tool, the `Minishaker` is attached trough four screws. It is important to underline that the robot is able to know simultaneously the position and the orientation of the tool, given as the distance and the rotations between two different coordinate systems, the tool coordinate system XYZ_{tool} and the base coordinate system, XYZ_{base}, kept fixed during the measurement campaign. The position of XYZ_{tool} can be determined and controlled with an accuracy of ±0.01 mm and ±0.01 deg, for what concerns translation and rotation, respectively.

In order to control and move the robot, different strategies can be used. The first that can be cited is controlling the robot arm trough the attached tablet, shown as well in Fig.(4.6). This solution presents many positive aspects, being really intuitive and a fast return time. However, the limited distance between the robot arm and the robot control unit, given by the fixed length of the cable, makes it less versatile, overall if a close test section is considered. Another possibility is to control the robot remotely from a PC, using a script made in house in `Python` or using commercial software as `RoboDK`. Due to its ability of showing a 3D preview of each future movement and saving different robot positions, the last option has been selected. In addition, due to its ability to enter in the so-called *collaborative* mode, the robot can be positioned manually, with the motors following the inputs given by the user. For this reason, if a programmed movement can be useful if a particular sweep has to be performed, the collaborative mode can be used in order to perform large and coarse positioning, from which a position optimization can be performed in order to adjust the region observed by the velocimetry probe.

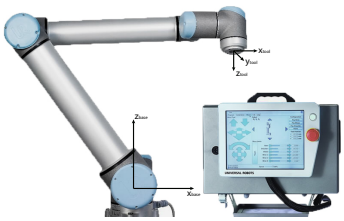

Figure 4.6: Universal Robot UR5

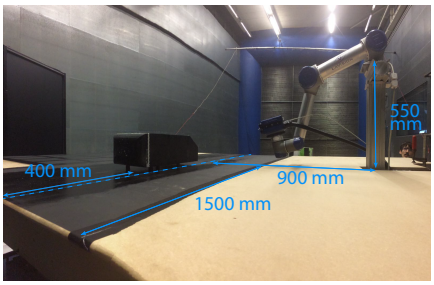

Figure 4.7: Experiment setup with dimensions.

The setup, with related distances, is shown in Fig.(4.7). One of the main advantages given by the usage of the robotic arm is the ability of moving its base, in order to be able to map bigger volumes. However, due to the dimensions of the object and the aim of the test, the robot base position has been kept fixed during the entire experiment. In order to place the robot where needed, X95 beams have been used, placing the base 900 mm from the leading edge of the floor, 550 mm

above the floor and 900 mm outboard w.r.t. the centerline of the Ahmed body. This position ensures the velocimetry probe to be able to scan the entire wake of the Ahmed body, without necessitating of base movement.

4.5 Calibration procedures

As underlined in the theoretical background, PIV is a technique able to measure flow characteristics through the analysis of 2D images. Both for 2D and 3D measurement, a calibration is required in order to map accurately the field of view imaged by the camera. Considering the Robotic PIV system used in the experiment, two different calibrations have to be performed at the beginning of the measurement campaign: the optical calibration and the rotation centre calibration. With respect to the traditional techniques, the usage of Robotic PIV requires only one calibration done a the beginning of the experimental campaign, leading to a noticeable saving in time.

4.5.1 Geometric optical calibration

As state-of-the-art, the optical calibration for volumetric PIV is performed acquiring images of a reference model, a calibration plate Lavision - Type 30 in this case, equipped with markers with prescribed positions, placing the calibration plate at different distances, in order to calibrate the entire measurement volume. Having available the UR5 robot arm, in this case the cameras are moved, with their position that ranges from 150 mm to 550 mm, if the distance between the Minishaker S casing and the plate surface is considered, obtaining pictures similar to the ones shown in Fig.(4.8). In this case, a standard pinhole-model calibration, Soloff et al. (1997), is used. Furthermore, to achieve the needed accuracy in calibration throughout the entire volume, a subsequent self-calibration, Wieneke (2008) is performed considering a free stream acquisition. Due to the application of the self-calibration, the RMS of fit is reduced from 0.31 pixel to values lower than 0.1 across the entire volume. Finally, as last step of the calibration, based on the disparity map created in order to perform the self-calibration, an optical transfer function (OTF) is created, which tries to improve the accuracy allowing a re-projections from 3D-space to 2D-image coordinates. This is one of the ingredients for applying STB algorithm and IPR, so that one of the ingredient to perform all the post processing considered in this work.

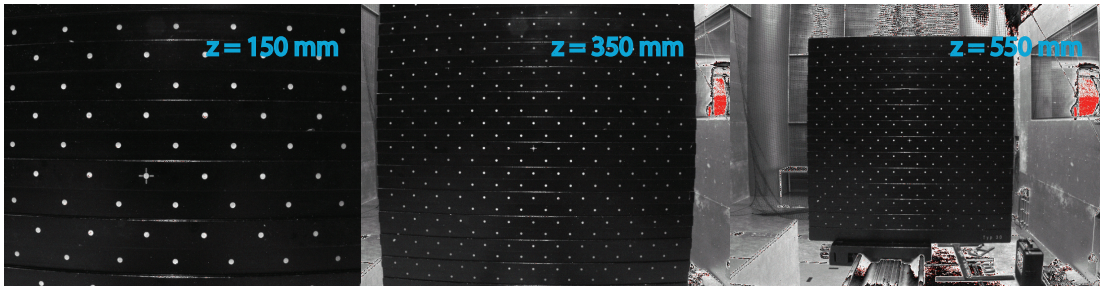

Figure 4.8: Calibration plate seen by three different camera positions, needed for geometrical calibration.

4.5.2 Robotic calibration

The second step needed in order to calibrate the Robotic PIV system, is the evaluation of the camera rotation centre. Fig.(4.9) shows the standard coordinate systems used during a measurement with Robotic PIV. Thanks to the geometric calibration, the system is able to map the space in front of the cameras, creating a coordinate system, XYZ_{camera}, that will be fixed w.r.t. the cameras position until the calibration remains valid. The second coordinate system that must be considered is XYZ_{tool}, the one positioned at the end of the robotic arm, where the Minishaker S is attached. Finally, as introduced before, a coordinate system, XYZ_{base} is positioned at the base of the robot, being the reference for any robot movement.

Due to the fact that, considering the state-of-the-art of the system, any result will be expressed w.r.t. XYZ_{camera}, it is necessary to map the results in a global coordinate system. A first possible choice for the global coordinate system is XYZ_{base}, if the base of the robot is kept fixed during the entire campaign. Taking into consideration this case, in order to pass from XYZ_{camera} to XYZ_{tool}, the vector between the origins of XYZ_{camera} and XYZ_{tool} must be measured. In order to do that, a specific Matlab code has been developed. Starting from different images of a black sheet with white markers, similarly to what done by Jux (2017), their positions are reconstructed using IPR. In order to improve the accuracy of the particle reconstruction, after masking the unnecessary part of the images, a Gaussian smoothing is applied. This helps the particle detection algorithm since it expects a Gaussian intensity distribution, proper of the illuminated particles.

Due to the low tomographic aperture, for every marker, the detection algorithm found several particles distributed along the coaxial axis. An average of their position gives the position considered as the final for the correspondent marker. At this point, a minimization problem is performed aiming to find the correct $\overline{X}_{CT}$ that makes all the points coinciding. The fundamental hypothesis behind this method is the possibility of obtaining XYZ_{tool} from XYZ_{camera} by rotations of angles multiples of 90° and subsequent translation. In order to ensure this, it is really important to acquire the images used for the geometrical calibration keeping the cameras always perpendicular to the plate and moving the robot arm along a path perpendicular to the plate as well.

Using this procedure, the vector found is equal to $\overline{X}_{CT} = [-0.5, -64.3, 417.3]$, where the values are expressed in mm.

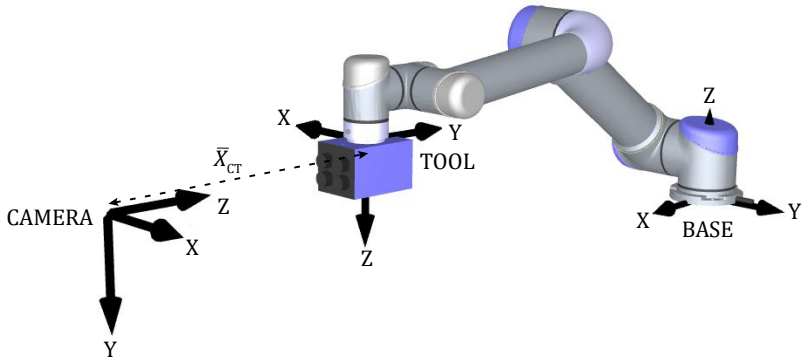

Figure 4.9: Coordinate systems of Robotic PIV.

4.6 Data acquisition procedures

As introduced before, the aim of this experimental campaign is to demonstrate the ability of a multi-Dt, DP technique in extending the velocity range of applicability of Robotic PIV. In order to reach the goal, two different steps have to be achieved. Firstly, results obtained with the new method have to be compared with the ones obtained by the state-of-the-art technique STB. In order to to that, a first measurement at low speed, 12 m/s, has been performed, acquiring data in both the procedures, TR and DP. For the double pulse data, the time separation between the two pulse has been varied between 122 μs and 610 μs, following the guide lines presented in Sec.3.4. This has permitted to obtain a maximum gain Δt^* of 5.

Afterwards, a second measurement has been performed increasing the velocity up to 20 m/s, finally to demonstrate the ability of the new technique. For this case, DP acquisition have been taken with Δt ranging between 61 μs and 610 μs, for a maximum gain Δt^* of 10.

4.6.1 Position of measurement

Since the aim of this experimental campaign was to test the performances of the new technique, it has been decided to acquire only one cone, varying all the required parameter. For this reason, literature has been used as reference in order to find a region of interest with the most useful aerodynamic structures for the aim. As reported in Chapter 2, from literature it is expected that, for a slant angle of 25°, two counter-rotating vortices are created along the slant edges and are convected downstream. Furthermore, two re-circulation bubbles are expected to be created just behind the vertical flat surface at the back of the body, as shown in Fig.(2.5), reproduced from the paper of Ahmed et al. (1984).

For this reason, the position of the cameras has been selected in order to being able to image all the aerodynamic feature just cited. Fig.(4.10a) shows the position of the measurement volume w.r.t. the Ahmed body position, where the expected path of the vortices is represented by dotted lines. Furthermore, Fig.(4.10b) shows a raw image of one of the cameras, from which it can be seen that

the field of view includes the rear of the Ahmed body and the region where the vortices are expected to be.

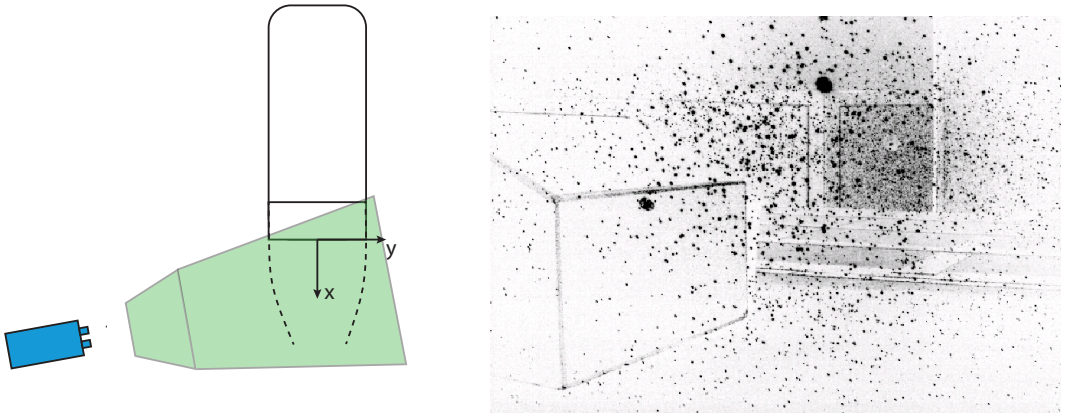

(a) (b)

Figure 4.10: (a) 2D representation of the measurement volume and (b) raw image acquired in that position from one of the cameras (inverted).

4.6.2 List of operations

In this section, the procedure followed for each acquisition done in the experiment is described. As introduced before, the first step is to calibrate the system through the geometrical calibration for the cameras and the robotic calibration, for mapping the results into a global reference frame. After that, the system can be use repetitively to acquire all the data needed, without necessitating of new calibration or particular expertise. The procedure used during this experiment is similar to the ones used by Jux (2017) and Giaquinta (2018), and it is repeated for sake of completeness:

Positioning of the CVV The velocimetry probe is positioned using the commercial software RoboDK. For the main part of the experiment, this action has been done once at the beginning of the measurement.

Acquisition of wind-off image In order to check if reflections or background intensity could affect the raw images, an image is acquire with wind off. The position chosen has been optimized during this stage in order to reduce all the strongest reflections, most from the body edges, introducing small angles in the probe positioning.

Storing of the position As soon as the position found is satisfying the requirements, it is stored into the cited software and also in a spreadsheet that will be used later for the processing. The information stored ranges from

the position of the robot in terms of XYZ_{tool} , wind tunnel velocity and time-step separation.

HFSB generation and injection The flow is seeded with the HFSB through the operation of the FSU, that is controlled remotely from the acquisition PC. The cameras are used in live mode, continuously acquiring, in order to visually assess the amount the seeding concentration.

Data acquisition As soon as the operator judges satisfying the amount of seeding, the prescribed amount of images is acquired. For the TR data, the acquisition frequency is kept at 700 Hz, while for the DP, it is reduced to 200 Hz. Furthermore, for the DP acquisition, before acquiring it has to be chosen also the Δt between the two pulses, that, as introduced before, for this experiment has been varied between 61 μs and 610 μs.

Data Storing and Seeding Stop Once the acquisition is finished, after a quick inspection of the data, if the operator judges satisfying what acquired, the images are stored and the seeding is paused. If DP measurements are being performed, the time-step can be quickly changed and a new acquisition can start from the previous step.

4.6.3 Selection of sampling strategy and required number of images

As introduced before, two kinds of measurement are conducted in this experimental campaign, namely time-resolved acquisitions and double-pulse, double frame acquisitions. Considering the time-resolved acquisitions, given a free-stream velocity of $U_\infty = 12$ m/s, it is necessary to crop the camera sensors in order to reach an acquisition frequency of 700 Hz in order not to encounter tracking issues, as introduced in the previous chapter.

On the other hand, for what concerns the double-pulse, double frame acquisitions, the opposite effect is wanted. Since data from subsequent couples of frames are not used together by the algorithm, a lower acquisition frequency has the positive effect of make them more temporally uncorrelated, improving the statistics of the final averaged result, given a fixed amount of images. For this reason, the acquisition frequency for this kind of measurement has been set at 200 Hz, being the lowest frequency accepted by the high-speed laser used in this experiment.

For what concerns the number of acquired images, a preliminary study on the uncertainty in the vortices region has been used to calculate the amount of samples required.

According to Heft et al. (2011), the Strouhal number of the C-pillar vortices is $St_v \approx 0.3$. Considering the length scale used by the cited work, being $L_{\sqrt{A}} = 167$ mm, it is possible to evaluate the characteristic frequency of the considered vortices:

$$f_v = \frac{St_v \cdot U_\infty}{l_{\sqrt{A}}} = 21.55\ Hz \tag{4.3}$$

Furthermore, according to Lienhart et al. (2003), the standard deviation of the velocity inside the core of the C-pillar, can be estimated to be $\sigma_v \approx 20\%$ of the mean velocity. If it is assumed that the majority of the uncertainty is given by the physical fluctuation of the flow, it is possible to evaluate the amount of images required to theoretically reach 4% of uncertainty on the mean velocity result through the equation:

$$\sigma_U = \frac{2\sigma_v}{\sqrt{N}} \tag{4.4}$$

that leads to $N_{eff} = 100$ uncorrelated samples. Taking into consideration the time scale of the vortices expressed by Eq.(4.3), this yields, according to Sciacchitano and Wieneke (2016), that is necessary to acquire a time equal to:

$$t_{acq} = \frac{2N_{eff}}{f_v} = 9.28\ s \tag{4.5}$$

that in number of images, if $f = 700$ Hz, is translated to $N_{prescr} = 6500$ images. It must be remarked also that, considering the procedures used, due to low seeding concentration given by the HFSB, a larger amount of acquired data helps in order to increase the final spatial resolution. For this reason, considering N_{prescr} as the lowest limit possible, the final number of samples used in this campaign has been $N = 8000$.

N has been used for all the acquisitions performed in this experiment, for both TR and DP data. The reader could argue that, due to the lower sampling frequency of the latter kind of data, N should have been reduced to have the same amount of uncertainty in the mean velocity results. However, it must be considered that since the multi-pass double-frame algorithm does not use temporal information within one dataset, its accuracy is lower than the one of STB, if the same amount of data are taken into account. For this reason, also for this kind of data, N has been used as number of images to be acquired.

4.7 Data reduction technique

In this section the steps taken in order to pass from raw data to velocity data are described. Starting from images of particles illuminated by laser light, the aim is to obtain the flow velocity distribution, from which it is possible to derive other quantities of interest, such as vorticity, pressure and other vortex indicators. Between the raw images and velocity data, multiple paths are available, depending on the characteristics of the fluid and of the hardware used. A theoretical background for the operations discussed here is approached in Chapter 2 and Chapter 3, while this section is more focused on the exact parameter used during the data processing of this experiment. In Sec.(4.7.1) the first step after the image acquisition, the image pre-processing is discussed. Afterwords, in Sec. 4.7.2 the parameters used by the two different tracking techniques, STB for TR data, introduced in Chapter 2, and the new technique introduced in Chapter 3, for DP data, are given. More in details, for what concerns DP data, also parameters used for the particle detection, through IPR, will be discussed. Finally, in Sec.(4.7.3) choice of the dimensions of the grid elements for the conversion from Lagrangian to Eulerian description of the flow field is discussed.

4.7.1 Image pre-processing

As explained in the previous chapters, PIV is based on the analysis of recorded images of illuminated particles. However, not only the particles reflect the laser light, but also everything else that is in the FOV, test object, walls, screens, will reflect a fraction of the laser light hitting them towards the camera. In order to have a robust and reliable measurement, the first condition is that the light intensity of the scattering particles must be higher than the light reflected by the other objects in the FOV. If this condition is not satisfied, the algorithms that try to reconstruct or track the particles will create several false results, increasing the total number of ghost particles, affecting considerably the final results. For this reason, some filters or technique have been developed in order to reduce the amount of the so-called noise, undesired light intensity in the FOV, from the raw images, step that is usually called image pre-processing. Furthermore, depending on the cameras used, the bit depth available changes and, with it, the maximum intensity that can be stored in a pixel varies. This means that, for each camera, if on a line of sight of one pixel there are multiple particles, the final intensity stored into it is the sum of the intensity scattered by the particles. Usually this is not a limitation, if the particle concentration is not too high. However, in the amount of intensity stored in the pixel it must be taken into account the intensity of the background noise and of the reflections. Overall the latter one, if really strong, can bring to the saturation of the pixel, namely exceeding the maximum amount of intensity storable. If this is the case, on that particular line of sight, it will not be possible to reconstruct or triangulate any particle, affecting the final results. For this reason, strong reflections must be completely avoided or limited. Related to this, some precautions can be taken already in the preparation stage of the experiment, such as the painting of the model with not reflecting paints, or during the experiment, avoiding illuminating surfaces perpendicular to the cameras. If in the images there are still reflections or strong noise, as introduced before, the image pre-processing can help.

About pre-processing strategies, several techniques have been proposed in literature. In this project, it has been chosen to use the Butterworth filter, an high pass filter (HPF), proposed by

Sciacchitano and Scarano (2014). This Butterworth filter considers the intensity of each pixel in all the images acquired, or in a subset of them, and decomposes it in the frequency domain. At this point, the high-frequency content of the spectrum is kept, while the low-frequency part is cancelled. The idea behind this is that the intensity that remains in the image in a fixed position or with a slow movement is coming from reflection of objects in the background and, for this reason, it can be eliminated without affecting the light coming from the particles. At this point the importance of not saturating any of the pixels in the FOV can be understood, since the filter applied, as the majority of all the other filters available, due to the constancy of the intensity in a saturated pixel, being always the maximum, would bring the intensity of that pixel in pre-processed image to 0, eliminating every information about particles passing through the line of sight of that pixel.

4.7.2 Tracking procedures

After the image pre-processing, the data has to be analysed in order to produce a velocity field. In this step, from simple 2D data, particle positions and velocities are obtained through different techniques, depending on the type of data. For TR data, the algorithm introduced in the Sec. 2.3.2, STB, has been used, whose parameters are discussed in the Sec. 4.7.2.

For DP data, the algorithm described in Chapter 3 has been used in order to pass from pre-processed images to Lagrangian velocity information. More detailed description of the parameter used is given in Sec. 2.1, for what concerns IPR, and in Sec. 2.1, for what concerns the tracking technique.

TR data: STB

For the TR data, the Lagrangian tracking technique STB (Schanz et al. (2016)) has been used through its implementation in the software Davis 8.4.0, by *LaVision*. While Sec. 2.1 deals with the working principle of STB, this section is focused on listing the choices done for the required parameters. Even if a commercial code has been used, the number of parameters that had to be set was considerable. First of all, it must be remarked that several of the listed parameters are case dependent, meaning that their choice must be guided by the flow or data characteristics. The first choice is about the volume that the algorithm has to use. This is expressed in mm and is related to the coordinate system XYZ_{camera}, introduced in the previous section. In order to analyse the data acquired, a volume 300×300 mm^2 has been chosen along x and y, with the z-component, the coaxial component, varying from 200 to -400, where the positive axis is towards the cameras. Knowing that the center of the calibration is ≈ 400 mm far from the cameras, this means that the measurement volume starts at a distance $z_0 \approx 200$ mm from the cameras.

Another important parameter that has to be set is the threshold for 2D particle detection I_{min}, the minimum intensity that the system has to consider in the input images. For this experiment it has been set $I_{min} = 20$ counts; however, it is easy to understand that it is strongly dependent on the noise level or on the image quality.

The following parameter that has to be set is the allowed triangulation error ε_Δ. Schanz et al. (2016) suggests a working range of $0.5 \leq \varepsilon_\Delta \leq 1.5$ px, depending on the raw data quality. Due to the low resolution of the Minishaker S cameras, it has been selected the maximum value, $\varepsilon_\Delta = 1.5$

px. This parameter is also important for the speed of the process, affecting all the particle searches in the initialization phase. Finally, the last main parameter is the maximum particle shift $\Delta_{p_{max}}$, given in voxel units, heredity of the tomographic reconstruction techniques. For the used setup, each voxel is equal to 0.27 mm. For this reason, considering a free-stream velocity of 12 m/s and an acquisition frequency of 700 Hz, at each time-step, the particle in the free-stream move of 17.14 mm, that, converted to the cited voxel unit, is equal to 66 voxel. For this reason, a maximum particle shift of $\Delta_{p_{max}} = 80$ vox has been considered, allowing an increase in velocity of 20%. Furthermore, additional parameters can be set, more specifically about the shaking procedure, the OTF interrogation and the export of the data. Fig.(4.11) shows the selection done for the post-processing done in this project. For further information about their meaning and effects, information can be found in the literature (Schanz et al. (2016)).

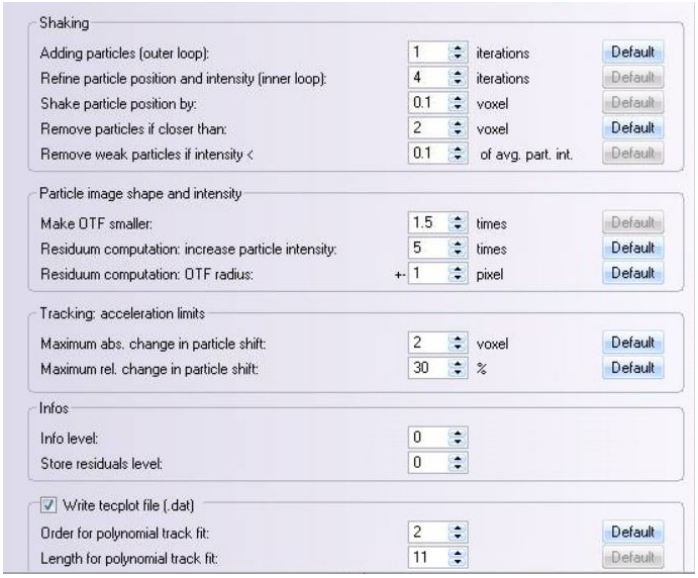

Figure 4.11: Shake the Box window of advanced settings, DAVIS 8.4.0 LAVISION.

DP data: particle detection through IPR

Considering the algorithm presented in Chapter 3, the particle detection is one of the fundamental steps required to achieve the velocity measurement. In this project, the advanced algorithm IPR has been used, as presented in Sec.(2.3.2), as implemented in DAVIS 8.4.0 IPR RELEASE. Being the input of IPR the pre-processed images, the algorithm is able to detect the particles in the volume selected by the user, giving as output a list of the positions in XYZ_{camera} of all the particles in each of the frames and their intensity. Fig.(4.12) shows the parameters used in this experiment. Some of the parameters can be recognized within the one already cited for STB in the previous section. This is led by the fact that STB uses IPR coupled with a NN algorithm as initialization in the first steps. Also in this case, a threshold for 2D particle detection I_{min} has to be selected. It can be noticed that it has been reduced, w.r.t. the one considered for STB, of 5 counts. This difference is required since,

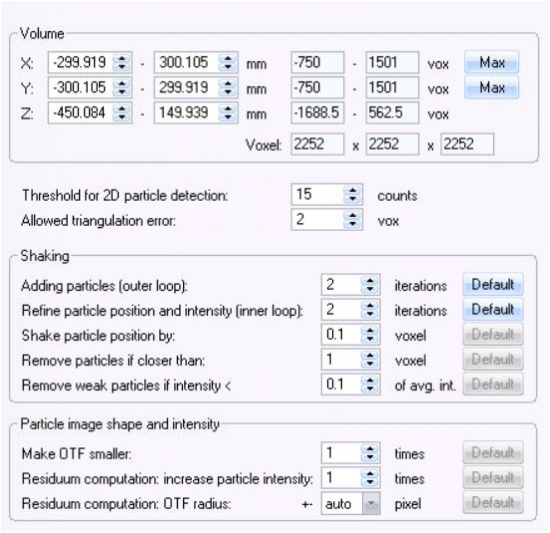

Figure 4.12: IPR settings window, DAVIS 8.4.0 LAVISION.

in DP acquisitions, the laser light for each of one the frames comes from only one of the cavities, reducing so the available power. For a more advanced discussion of the parameters, literature is pointed as the source where information can be found (Wieneke, 2013).

4.7.3 Binning: conversion to structured grid

Results obtained by STB and by the tracking algorithm proposed in Chapter 3 are both unstructured, having the information at the particle position and at the midpoint of lines connecting the same particle at two subsequent frames, correspondingly for STB and for the proposed method. In order to analyse the data, it is often useful to bring the information onto a structure mesh or grid, changing the type of description of the flow field from Lagrangian to an Eulerian. Reasons behind this are multiple. First of all, if multiples runs have to be merged together, something that happens often if Robotic PIV is used, it is useful to define a global grid, in which data from multiple runs can be poured in. Furthermore, for comparison between different run, a comparable grid is important to avoid misunderstanding of the flow feature given by a not uniform distribution of the particles in the volume in each measurement. Lastly, if gradient-based quantities, as vorticity, have to be calculated, so that spatial gradients are needed, having a structured grid yields to much simplified calculations. For these reasons, several techniques to interpolate or average scattered results on a structured grid have been developed along the years. Due to the big amount of data produced by 3D PTV algorithms with the particle concentration considered in this experiment, and the industrial aim behind this project, elevating the computational cost as one of the main cost function to be taken into account in the decision process, the conversion method shown in Sec(3.3) has been considered the best option to achieve a good trade-off between computation cost and accuracy. Being the final data an average of instantaneous data, represented by the particles with associated their velocities, it is possible to evaluate the statistics, such as the uncertainty on the mean value. In order to evaluate this uncertainty it is possible to use the following formula:

$$\varepsilon_u = \frac{k\sigma_u}{\sqrt{N}} \tag{4.6}$$

where N represents the number of uncorrelated sample per bin. For this reason, it is clear that, for a given amount of particles, an increase in spatial resolution due to smaller bins, leads to an increase of uncertainty due to the smaller amount of particle per bin. For this reason, a balance between these two quantities must be found, overall based on the concentration of the experiment.

CHAPTER 5

RESULTS AND DISCUSSION

In this chapter, the results obtained by the application of the technique described in Chapter 3 are presented. Firstly, the analysis of the performance of the method is reported in terms of velocity distribution and percentage of correct pairing in the $20 \times 20 \times 20$ cm^3 volume considered in Chapter 3. Secondly, the data acquired in the near wake of the Ahmed body with $U_\infty = 12$ m/s are presented, comparing the obtained results with the ones given by DP-DF acquisitions and TR acquisitions, processed, respectively, as described in Chapter 3 and Chapter 4. Finally, the data of the near wake of the Ahmed body with $U_\infty = 20$ m/s are shown and commented.

5.1 Pairing analysis

As seen in Chapter 3, if a DP-DF measurement coupled with a PTV approach is considered, the choice of the pulse separation time Δt affects the accuracy of the results directly, in terms of DVR and percentage of correct pairing. If a longer pulse separation, and consequently a more extended particle displacement, helps to diminish the relative error on the velocity determination, as proven in Chapter 3, it can lead to a reduction of correct particle pairing percentage, causing a degrade of the final velocity measured. Applying the method described in Chapter 3, it is aimed at being able to stretch the pulse separation time without affecting the percentage of correct pairing.

In order to establish the performances of the method, different evaluations have been performed. Fig.(5.1) shows time-averaged velocity field along the free-stream axis on a YZ plane placed at x/H = 1, where H represents the total height of the Ahmed body. Similarly to what done in Chapter 3, firstly, a 20x20x20 cm^3 portion of free-stream has been considered, labelled as region A in Fig.(5.1). The choice of this volume is driven by the awareness that the regions with the highest velocities are the ones most affected by spurious pairing, due to the increase in the ratio $\Delta x/\overline{r}$.

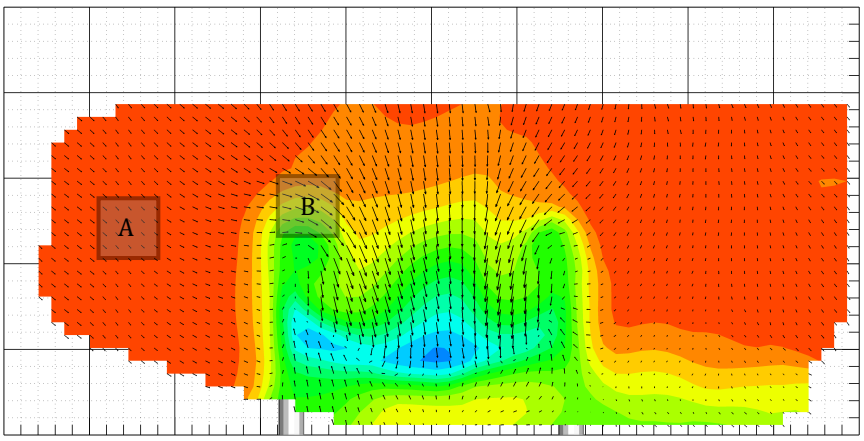

Figure 5.1: Streamwise velocity plotted for the plane x/H = 0.1. Region considered to evaluate the velocity distribution are highlighted and labelled.

Fig.(5.2) shows the distribution of the main component of the velocity u in the considered volume. Fig.(5.2a) and Fig.(5.2b) show results obtained by standard DP-DF acquisitions with, respectively, $\Delta t = 122\ \mu s$ and $\Delta t = 610\ \mu s$. Fig.(5.2c) presents the results obtained by the MΔt-DP method proposed, with $\Delta t_{Short} = 122\ \mu s$ and $\Delta t_{Long} = 610\ \mu s$. For all the figures, the distribution of the velocity is plotted in terms of relative frequency N/N_{TOT}. As discussed in Chapter 3 for the DP-DF acquisition done with the short Δt the distribution of the velocity is represented by a Gaussian distribution, as expected. If the effect of the increase of Δt is given by the narrowing of the Gaussian distribution around the expected values of 12 m/s, the effect of the predictor is to strengthen the particle pairing robustness as testified by the reduction of the noise represented by the second peak of the velocity distribution noticeable in Fig.(5.2b). In order to compare the results of Fig.(5.2a) and Fig.(5.2c) can be useful to consider the standard deviation of the **u** component

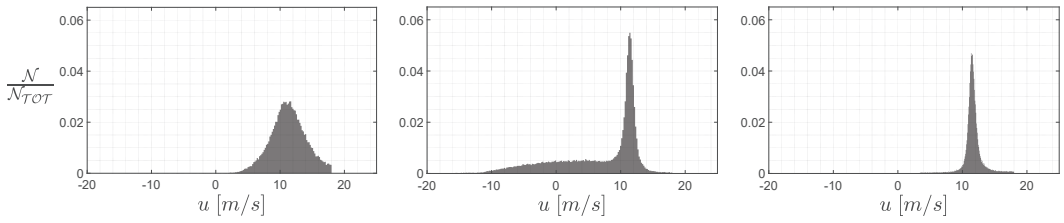

(a) (b) (c)

Figure 5.2: Distribution of the **u** component of the velocity in a $20 \times 20 \times 20$ cm^3 portion of the free-stream region obtained by DP/DF acquisitions for different pulse separation times (a) 122 μs, (b) 610 μs, and by MΔt-DP with (c) Δt_{Short} = 122 μs and Δt_{Long} = 610 μs. Free-stream velocity: U_∞ = 12 m/s.

in the considered volume. The application of the Multi-Δt DP strategy brings a reduction of $\mathbf{u}'$ of about 53 % w.r.t. the one obtained by applying a standard DP-DF strategy with Δ_{Short}. This result testifies an increment of the accuracy of the final averaged value.

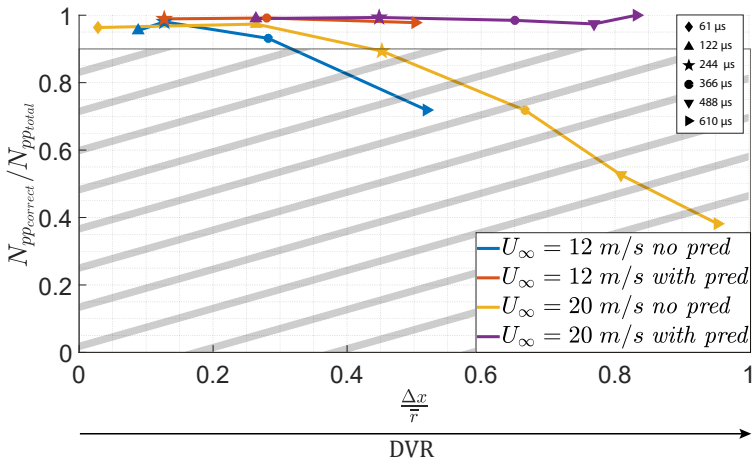

Figure 5.3: Percentage of correct pairing considering a free-stream region of 20x20x20 cm^3 varying the pulse separation Δt and comparing simple DP-DF pairing with MΔt-DP strategy.

At this point, considering the same volume, with the methodology described in Sec. 3.2, the amount of correct pairings has been evaluated for data acquired with the Multi-Δt, DP technique at different free-stream velocities. For low velocity, U_∞ = 12 m/s, the short pulse separation time has been set to Δt_{Short} = 122 μs, with the long Δt_{Long} varying from 244 μs to 610 μs. For high speed acquisitions, U_∞ = 20 m/s, Δt_{Short} = 61 μs and Δt_{Long} varies from 122 μs to 610 μs. Fig.(5.3) shows the results obtained. With respect to the figures of Sec.3.2, only results obtained with α = 0.5 are shown. In order to evaluate the position along the horizontal axis of each measurement, the actual particle concentration of each run has been considered to evaluate the mean particle distance $\overline{r}$. The minimum accepted percentage of correct pairing has been set to 90%. The region

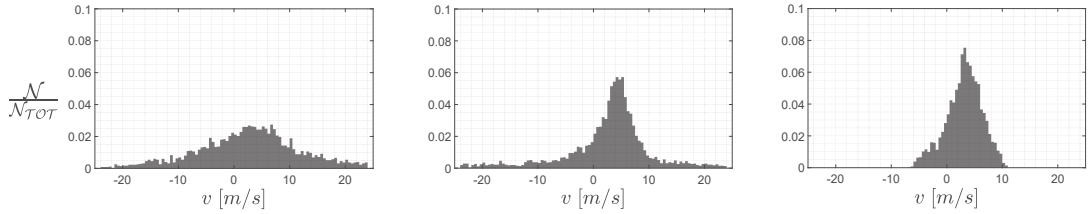

(a) (b) (c)

Figure 5.4: Distribution of coaxial **v** component of the velocity in a $20 \times 20 \times 20$ cm^3 portion of C/pillar region obtained by DP/DF acquisitions for different pulse separation times (a) 122 μs, (b) 610 μs, and by MΔt-DP with (c) Δt_{Short} = 122 μs and Δt_{Long} = 610 μs. Free-stream velocity: U_∞ = 12 m/s.

characterised by unacceptable pairing capability are shaded in the considered figure. As discussed in Chapter 3, the increase of the pulse separation time Δt, that corresponds to a rise of the ratio $\Delta x/\overline{r}$ for a constant particle concentration, causes a loss of pairing robustness for a standard DP-DF acquisition strategy, as testified by the blue and yellow lines of Fig.(5.3). In fact, considering the results obtained with U_∞ = 20 m/s, already with a Δt = 244 μs the percentage of correct pairing becomes lower than the selected threshold.

On the contrary, from the purple line, it is possible to notice that applying the Multi-Δt DP strategy, the percentage of correct pairing stays constant around 95% even for $\Delta x/\overline{r} > 0.3$, up to displacements equal to 95% of the mean particle distance. It must be underlined that, as represented in Fig.(5.3), the stretch of the particle displacement achieved with a longer Δt has the effect of increasing the DVR. This brings to an enhancing of the accuracy of the final velocity determination, as it will be shown in the next section.

If the free-stream region is expected to be the most critical for what concerns the maximum achievable displacement, the component along the coaxial direction, y for the considered experiment, is expected to be the one most affected by random errors due to the low tomographic aperture as introduced in Chapter 3. For this reason, a second $20 \times 20 \times 20$ cm^3 volume has been considered, more precisely, region B shown in Fig.(5.1). The choice of this regions is driven by the fact that it is expected to be the portion of the flow in which the highest coaxial velocity is achieved, on the upper border of one of the flow structures called C-pillars. In this case, the distribution of the v component has been evaluated and plotted in Fig.(5.4), where each bin of the histogram has a width of 0.5 m/s. Here a different behaviour w.r.t. the one shown in Fig.(5.2) can be noted. The large error induced by the low tomographic aperture is seen in Fig.(5.4a), where a wide Gaussian distribution represents the velocity distribution. However, contrary to what seen for the main velocity in the free-stream, stretching the Δt and analysing the results with a standard DP-DF approach, shown in Fig.(5.4b), does not introduce visible pairing errors. This behaviour is due to the fact that, even if the displacement of the particle in the free-stream becomes too large to ensure an acceptable percentage of correct pairing, as seen in Fig.(5.2a), since the velocities along the coaxial direction are lower, even considering the longest δt, the displacement Δy remains under the threshold that ensure an acceptable percentage of correct pairings. Fig.(5.4c) shows the velocity distribution obtained by the application of the MΔt-DP strategy. The application of the predictor leads to the reduction of

the uncertainty on the velocity determination, testified by the disappearance of the tails. However, the standard deviation of the **v** component remains higher than the one showed for the free-stream, comparing Fig.(5.2c) and Fig.(5.4c). However, this behaviour can be explained by the position of the volumetric probe. It is natural to expect higher values of velocity standard deviation in regions where a vortical structure is present than in a portion of the free-stream flow.

5.2 Ahmed body headwind flow field at $U_\infty = 12$ m/s

In this section, the results in terms of flow features obtained by the MΔt-DP strategy are compared to the ones obtained by STB and by DP-DF. Furthermore, all of them are compared to the results presented by Giaquinta (2018), considered as the reference. In all the results reported in this section, the axes represent the dimensions scaled with respect to the total height of the Ahmed body H, while the velocities are normalised by the free-stream value U_∞.

Fig.(5.5) and Fig.(5.6) show the results in terms of **u** component given by, respectively, STB, DP-DF with $\Delta t = 122\ \mu s$, DP-DF with $\Delta t = 610\ \mu s$ and MDt-DP with $\Delta t_{Short} = 122\ \mu s$ and $\Delta t_{Long} = 610\ \mu s$, at $x/H = 0.45$. Firstly, Fig.(5.6a) confirms the results obtained in Chapter 3 for what concerns the data acquired with a DP-DF strategy with $\Delta t = 610\ \mu s$. In this case, the pulse separation time is too large to permit a correct pairing, overall in the region characterised by large velocities. Furthermore, due to the non-uniform magnification, the region further from the cameras are more affected by false pairings due to the larger image particle displacement. The error given by false pairings leads to an underestimation of the flow velocity. This effect can be explained looking at noise shown in Fig.(5.2b) that affects the average done during the binning process. Due to the low quality of the results given by the analysis of the data acquired with DP-DF and $\Delta t = 610\ \mu s$, this case is not considered in the next results.

A quick analysis of the other data shows a good agreement for what concerns the **u** component. Comparing STB, DP-DF with $\Delta t = 122\ \mu s$ and the MΔt-DP results, the main flow features are detected in all the cases. More specifically, if the regions with $u/U_\infty < 0.1$ are considered, in all the three cases they are bounded within the domain $[-0.5 < y/H < 0.5, -0.2 < y/H < 0.5]$. This result is in line with the one obtained by Giaquinta (2018). The similarity between the data acquired with DP-DF, with the lowest pulse separation time, and the MΔt-DP, for what concerns the main component **u**, can be explained looking at Fig.(5.2). Even if the data are more spread around the averaged value, the binning process produces an average that close to the expected value, since no false pairings affect the result.

However, the difference between the two methods can be noticed in Fig.(5.7), where the standard deviation of the main component **u** evaluated during the binning phase is plotted. As expected, STB is the method that guarantees the lowest $\mathbf{u'}$ thanks to the usage of temporal information. For what concerns the other two considered methodologies, data acquired with the MΔt-DP method presents a standard deviation in the free-stream region between the cameras and the Ahmed body in average four times higher than the one given by STB, while, for what concerns the measurement done with the DP-DF, $\mathbf{u'}_{DP\_DF}/\mathbf{u'}_{STB} = 15$. Proved the limitations of a standard DP-DF approach, for the next results the analysis is performed comparing only the results obtained by STB and MΔt-DP only.

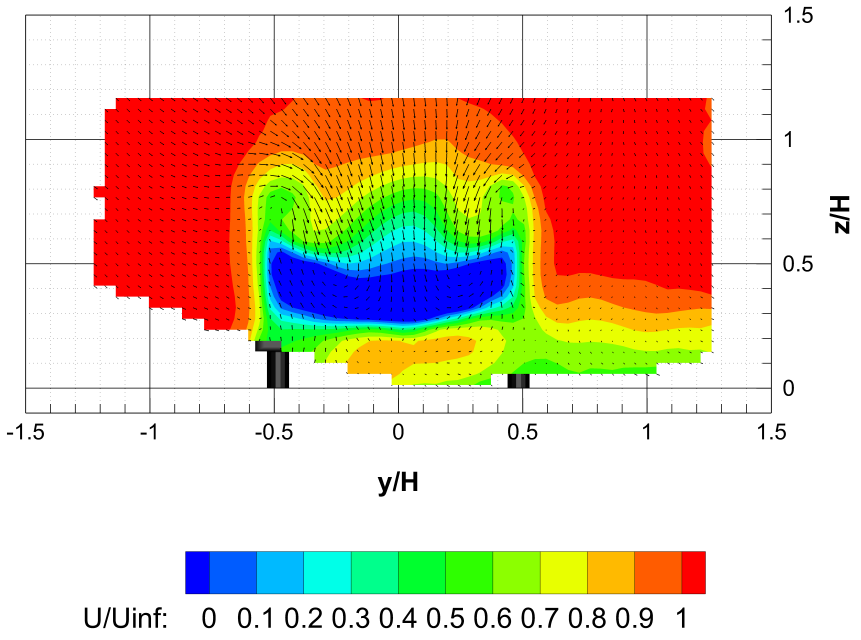

(a)

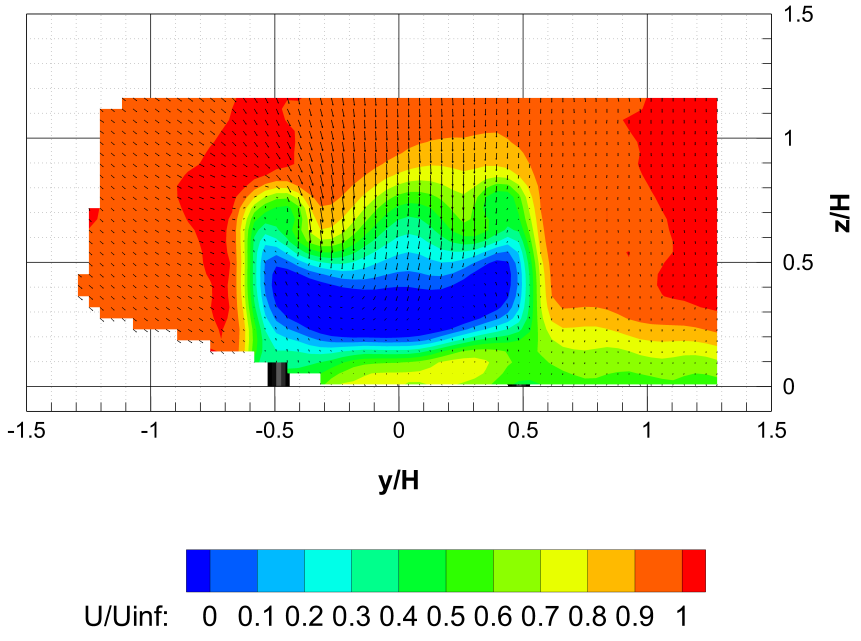

(b)

Figure 5.5: Normalised velocity component **u** downstream the model on plane x/H=0.45, (a) STB (b) DP-DF with $\Delta t = 122\ \mu s$.

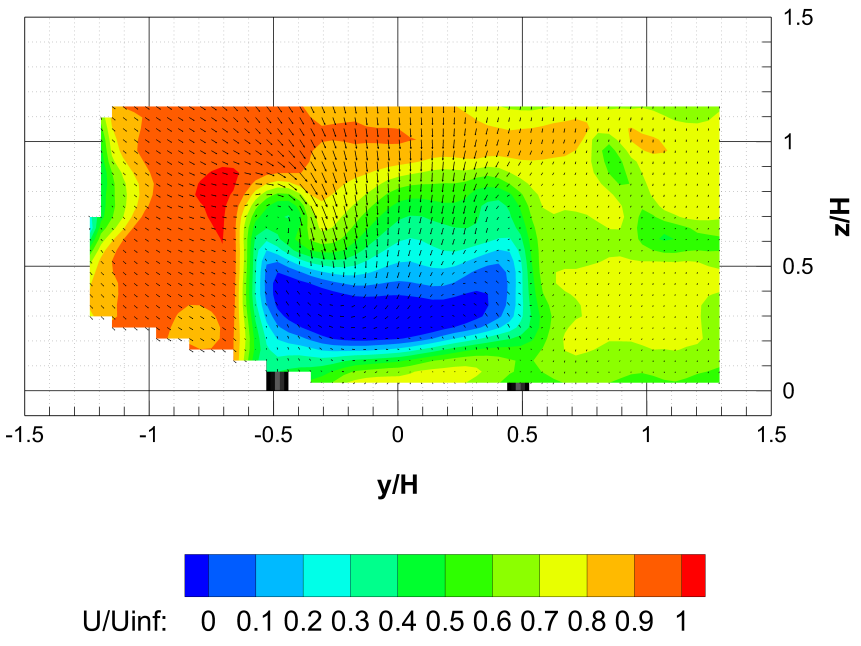

(a)

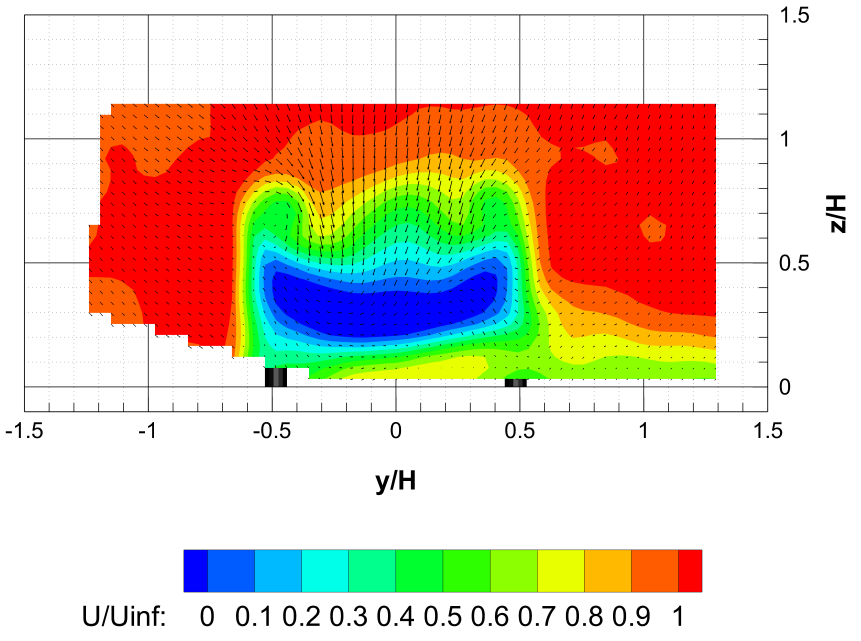

(b)

Figure 5.6: Normalised velocity component **u** downstream the model on plane x/H=0.45, (a) DP-DF with Δt = 610 μs (b) MΔt-DP with Δt_{Short} = 122 μs and Δt_{Long} = 610 μs.

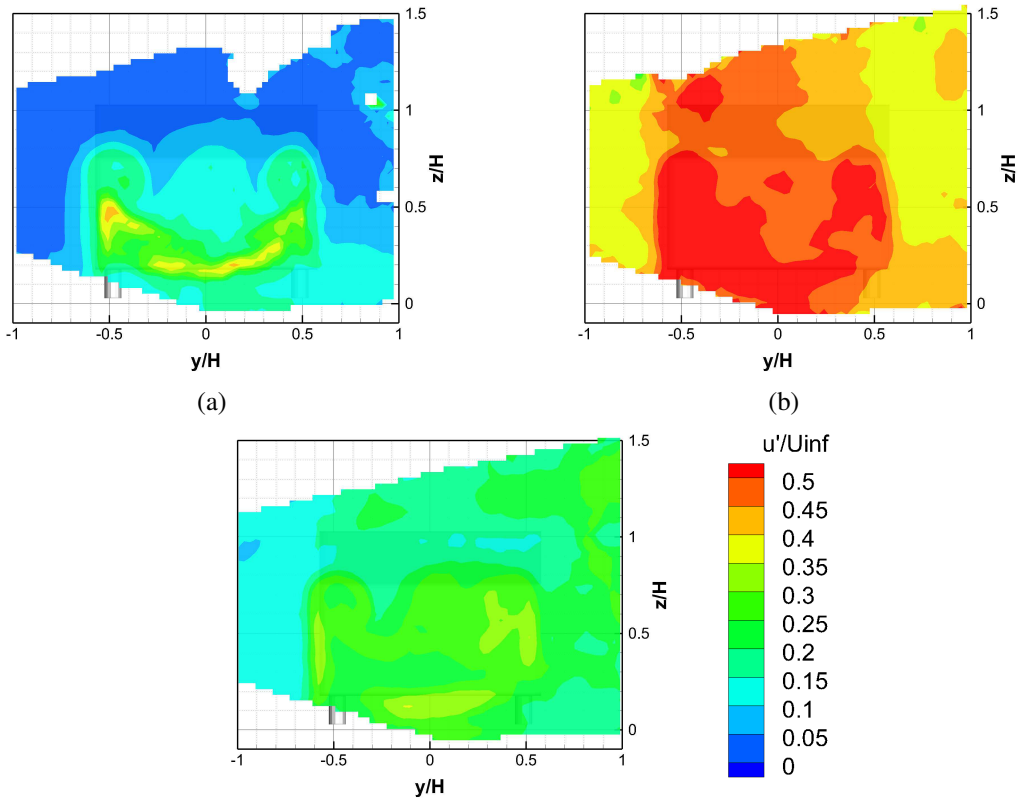

Figure 5.7: Normalised standard deviation of the velocity component **u** downstream the model on plane x/H=0.45, (a) STB (b) DP-DF with Δt = 122 μs (c) MΔt-DP with Δt_{Short} = 122 μs and Δt_{Long} = 610 μs.

In order to continue the present analysis, the flow topology on the symmetry plane has been evaluated to assess the performances of the MΔt-DP method compared to the reference given by STB. As Fig.(5.8) shows, the results obtained by the presented method are comparable to the ones given by STB. The recirculation region behind the Ahmed body, consisting of two vortices, as shown by Giaquinta (2018), extends until x/H = 0.5 for both the methodologies. Looking at the data obtained by applying the Mdt-DP strategy, the recirculation bubble on the slant seems to reattach before the end of the slant surface, a fact also underlined by Giaquinta (2018) for the same φ. Looking at Fig.(5.8) a difference in behaviour close to the surface of the model is noticeable. One possible explanation of this effect is given by the different laser power used by the two methods. Indeed, while STB uses for each acquisition two cavities contemporary, the MΔt-DP method uses only one cavity per image. This brings to a reduction of the reflections on the model, improving the quality of the data close to the surface. Finally, in Fig.(5.9) three contour lines produced by the two methods are overlapped, showing an acceptable level of correspondence.

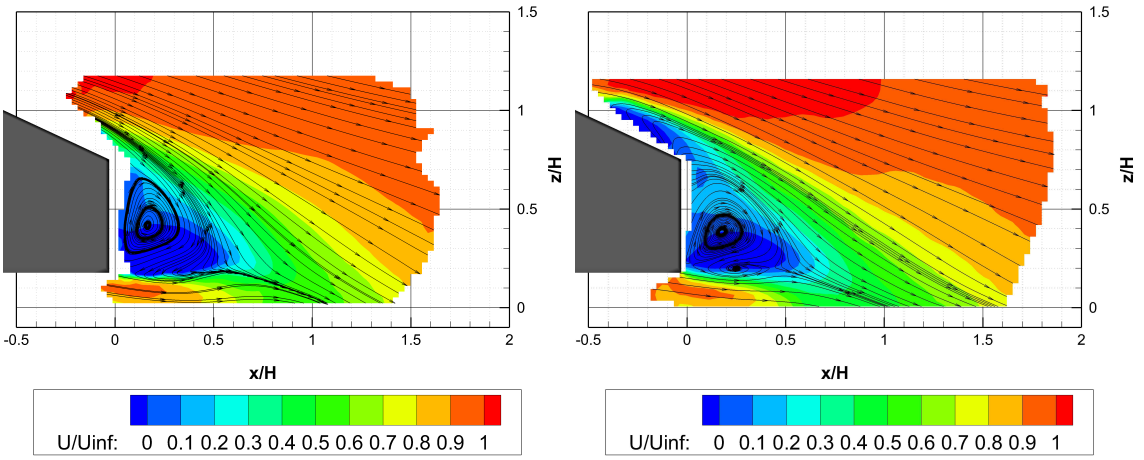

Figure 5.8: Nondimensional streamwise velocity **u** and strealines on the symmetry plane y/H = 0. (a) STB (b) MΔt-DP.

As expressed in Chapter 3, an important factor that describes the performances of a PIV system is the DVR, the ratio between the maximum measurable velocity and the minimum resolvable one (Adrian (1997)). If time-averaged measurements are considered, Schneiders (2017) derived a formula in which the lowest measurable velocities are represented by the velocity uncertainty. If the free-stream value is taken as the maximum velocity measurable, it is possible to define the $\overline{DVR}$ for time-averaged measurement as

$$\overline{DVR} = \frac{u_{max}}{\sigma_{\overline{u}}} \tag{5.1}$$

Considering the time-resolved data acquired, processed with STB, the $\overline{DVR}$ can be expressed

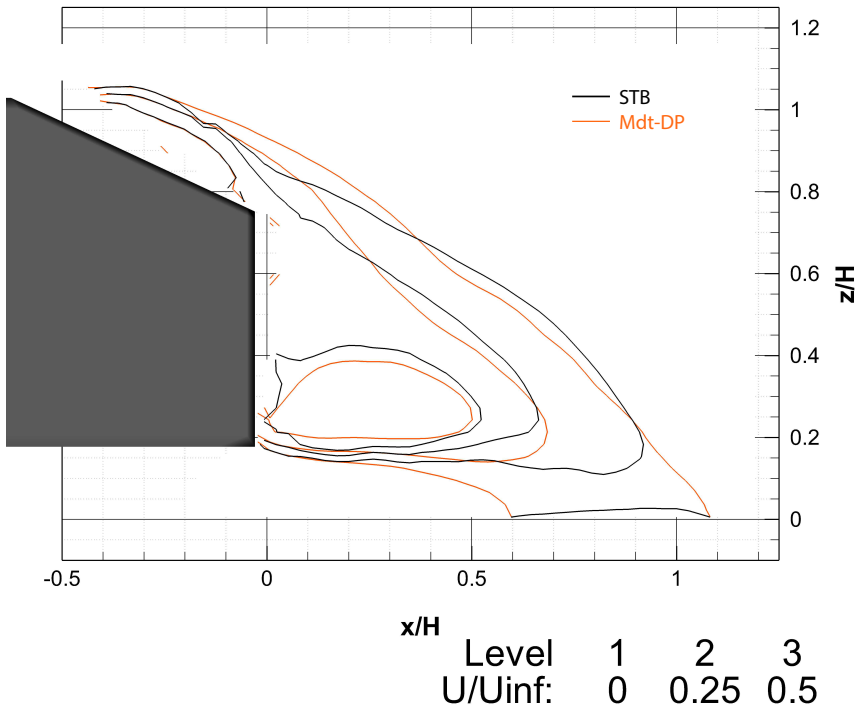

Figure 5.9: Comparison between contour level of the streamwise velocity component **u** produced by STb and MΔt-DP on the symmetry plane y/H=0.

with the following expression:

$$\overline{DVR} = \frac{12}{0.15} = 80 \tag{5.2}$$

where, for evaluating the standard deviation of the velocity, the vertical in-plane component of the velocity has been considered. This choice is driven by the awareness that the uncertainty on the vertical component in the free-stream can be considered produced by only measurement system and not by physical behaviours. For the DP-DF measurement, the uncertainty increases to $\sigma_{\overline{w}} = 0.6\ m/s$, giving a $\overline{DVR} = 20$.

As expected, the application of the MΔt-DP method gives higher dynamic velocity range w.r.t. the level achievable with the DP-DF at the longest time-step that does not suffer from errors given by wrong pairing. Indeed, the uncertainty measured in the free-stream for the measurement performed with the MΔt-DP strategy is $\sigma_{\overline{w}} = 0.3\ m/s$, which brings to $\overline{DRV} = 40$.

Up to this point, the presented results confirm the ability of the MΔt-DP of detecting the flow characteristics along the stream-wise component.

Fig.(5.10) shows the normalised velocity along the coaxial direction on the x-plane x/H = 0.45. As expected, this is the component where there are the larger differences between the MΔt-DP method and STB. More specifically, the velocity peak found by STB in the upper part of the vortices is underestimated by both the DP-DF and the MΔt-DP. For what concerns the DP-DF this can be

explained by the low accuracy given by the short pulse separation used. On the other hand, a possible explanation for the underestimation done by the MΔt-DP method is given by the truncation effect brought by the predictor. Indeed, the predictor has everywhere a curvature radius equal to ∞. For this reason, where the curvature radius decreases, the truncation error introduced by the predictor increases.

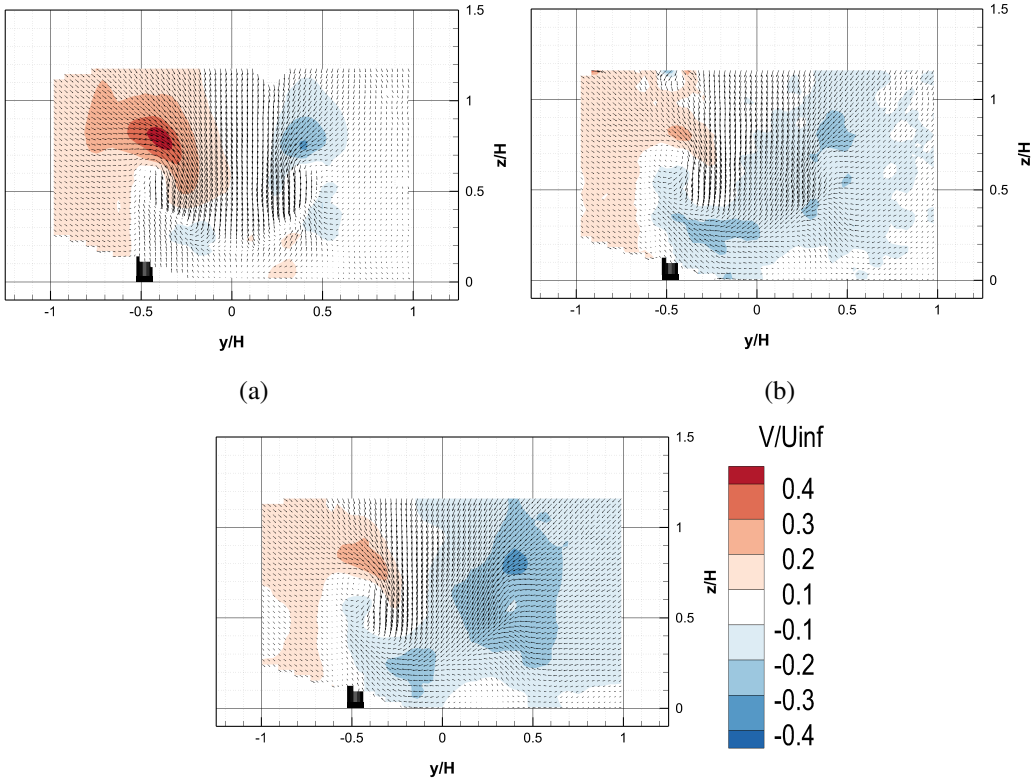

Figure 5.10: Normalised velocity component **v** downstream the model on plane x/H=0.45, (a) STB (b) DP-DF with Δt = 122 μs (c) MΔt-DP with Δt_{Short} = 122 μs and Δt_{Long} = 610 μs.

In order to evaluate the capability of vortex detection of the proposed method, the position and the intensity of the two C-pillar vortices have been evaluated and compared for the three considered methods. Fig.(5.11) shows the measured axial vorticity ω_x at the plane x/H = 0.24. For what concerns the position of the main vortices, a good agreement can be found between the results given by STB and by the Mdt-DP. This is also confirmed by Fig.(5.12), where the paths of the two main vortices obtained by the different methods are shown. On the contrary, the vorticity intensity is clearly underestimated by the DP-DF and Mdt-DP method, as shown in Fig.(5.13).

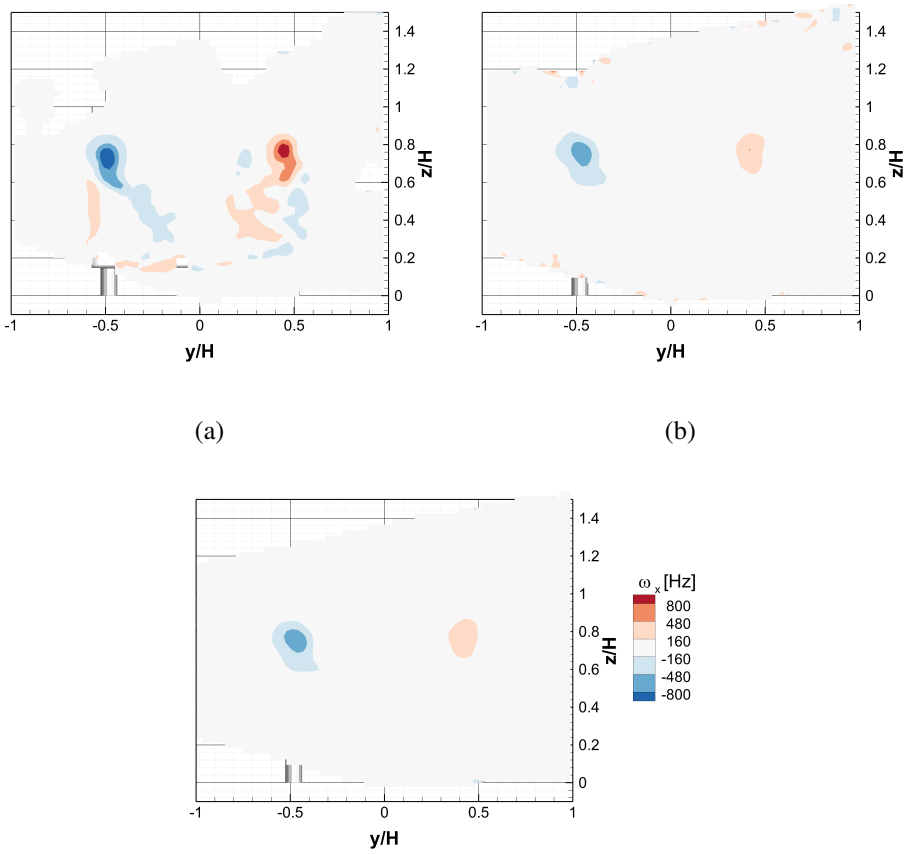

Figure 5.11: Axial vorticity ω_x downstream the model on plane x/H=0.24, (a) STB (b) DP-DF with Δt = 122 μs (c) MΔt-DP with Δt_{Short} = 122 μs and Δt_{Long} = 610 μs.

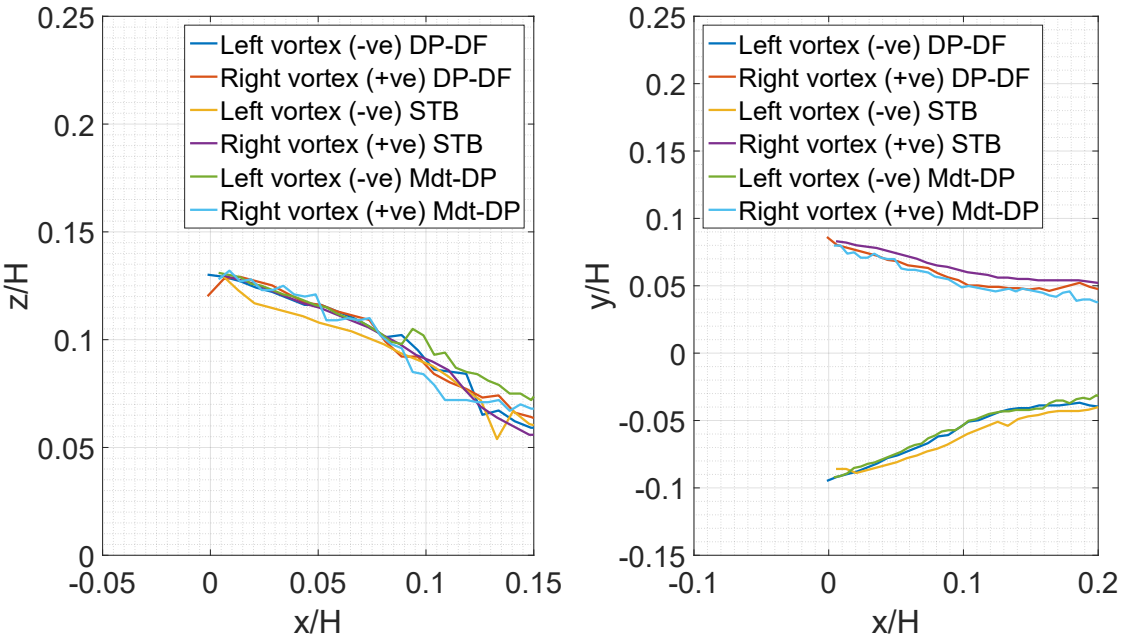

(a) (b)

Figure 5.12: Vortices position measured with the methods: STB, DP-DF and MΔt-DP. (a) side view (b) top view.

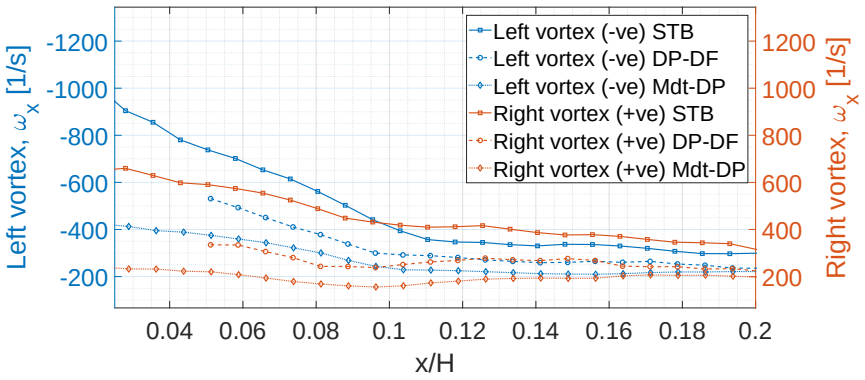

Figure 5.13: Vortices strength measured with the methods: STB, DP-DF and MΔt-DP.

Finally, Fig.(5.14) shows the iso-surfaces of streamwise vorticity $\omega_x = \pm 200\ Hz$ obtained by applying the three different strategies. All the methods are able to identify the main structures, the counter-rotating vortices called C-pillars, that are created from the slant lateral edges and

travel downstream converging towards the centre-line, as remarked in Fig.(5.12b). As shown in Fig.(5.12a) the C-pillars also move towards the ground while they are convected downstream. Considering Fig.(5.14b), another reason for the need of the Mdt-Dp becomes clear. Even if the DP-DF can detect the main structures, its results are noisier if compared to the ones produced by the method proposed in this work due to the lower accuracy that is given by the shorter final pulse-separation time.

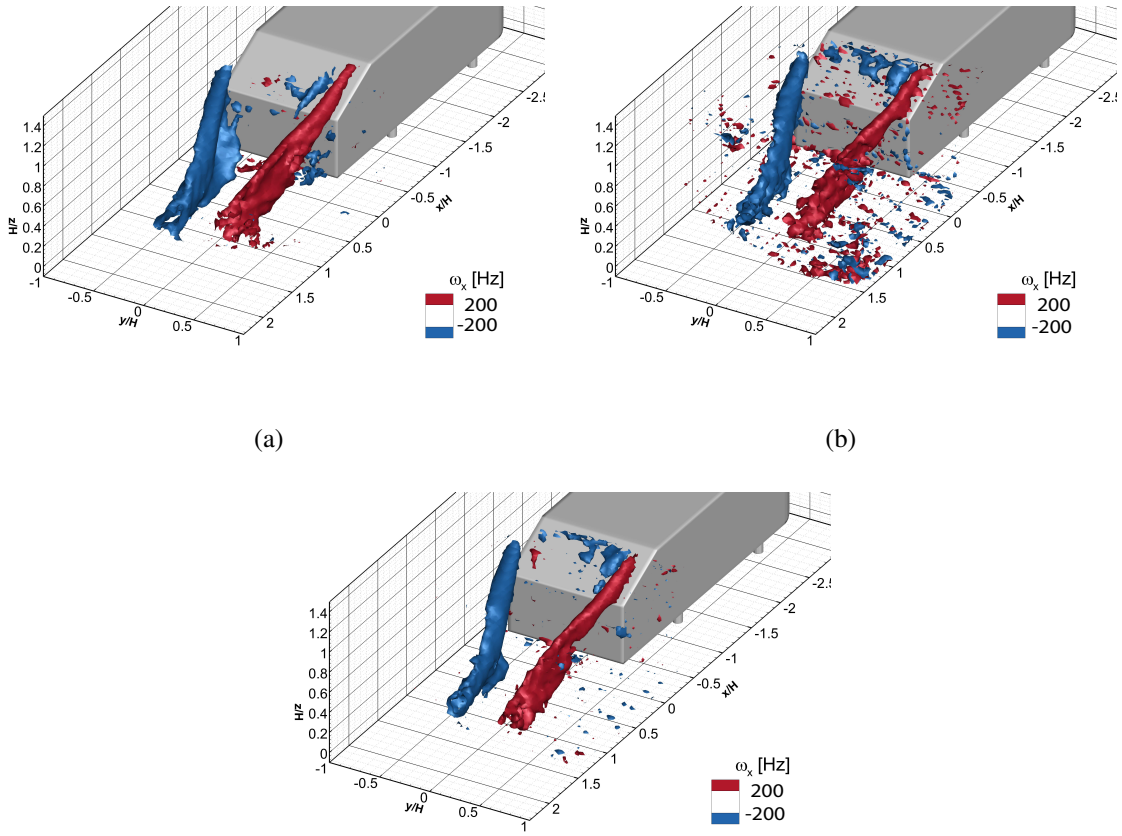

(a) (b)

(c)

Figure 5.14: Iso-surfaces of streamwise vorticity $\omega_x = \pm 200\ s^{-1}$. (a) STB (b) DP-DF with $\Delta t = 122\ \mu s$ (c) MΔt-DP with $\Delta t_{Short} = 122\ \mu s$ and $\Delta t_{Long} = 610\ \mu s$.

5.3 Ahmed body headwind flow field at U_∞ = 20 m/s

In order to demonstrate the ability of the proposed technique to cope with flows at higher velocities, the Mdt-DP strategy has been used to investigate the flow feature of the near wake of the Ahmed body for a free-stream velocity $U_\infty = 20\ m/s$. Fig.(5.15a) shows the normalised streamwise component of the velocity in the plane x/H=0.45. The vectors in the image represent the velocity tangent to the plane. Also in this case, the flow filed shows all the expected characteristics, with the two main vortices detectable by their rotation and the separation bubble behind the back of the body. The recirculation behind the rear part of the model can be more specifically investigated in Fig.(5.15b), where the normalised streamwise component of the velocity is plotted on the symmetry plane. Here two distinct counter-rotating vortices are visible, as also shown by Giaquinta (2018).

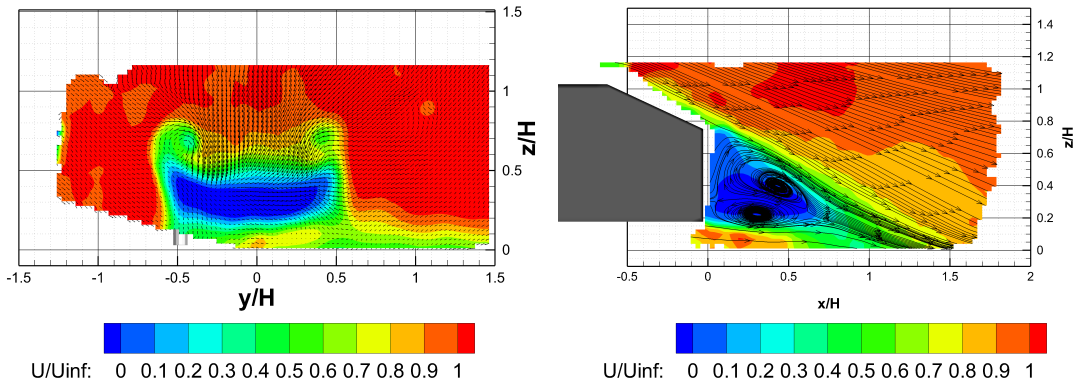

(a) (b)

Figure 5.15: Results obtained by application of MΔt-DP with $\Delta t_{Short} = 61\ \mu s$ and $\Delta t_{Long} = 610\ \mu s$ to the case with $U_\infty = 20\ m/s$ (a) Normalised velocity component **u** downstream the model on plane x/H=0.45 (b) Normalised velocity component **u** on the simmetry plane y/H=0.

The iso-surfaces of streamwise vorticity $\omega_x = \pm 250\ Hz$ are plotted in Fig.(5.15). Also in this case, the two biggest structures, the C-pillars vortices are detected by the technique. However, the result presents more noise than the one obtained at lower velocities (Fig.(5.14c)). This could be explained by the lower statistical convergence reached by the measurement done at higher velocities. Due to the higher speed, the concentration of bubbles in the flow decreases. For this reason, for a certain amount of samples acquired, the number of measured velocity for each bin decreases, lowering the quality of the final averaged data.

Fig.(5.17) shows a comparison of the position of the vortical structures obtained from the TR data acquired at 12 m/s and processed with STB and from the data acquired and processed with the Mdt-DP approach at 20 m/s. A good agreement of the position and of the path is found, demonstrating the low Reynolds dependency of the vortical structures formed at the rear of the Ahmed body, as reported in literature.

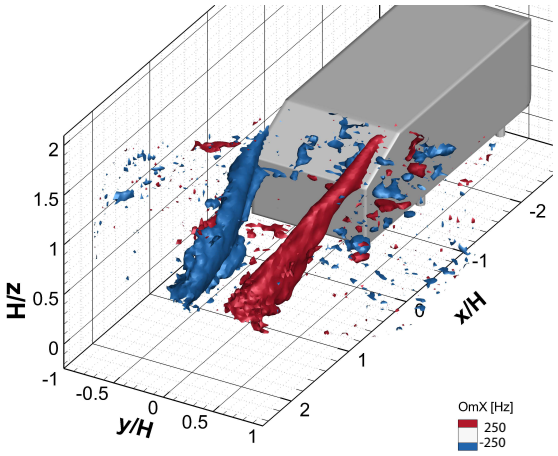

Figure 5.16: Results obtained by application of MΔt-DP with $\Delta t_{Short} = 61\ \mu s$ and $\Delta t_{Long} = 610\ \mu s$ to the case with $U_\infty = 20\ m/s$. Iso-surfaces of streamwise vorticity $\omega_x = \pm 250\ s^{-1}$.

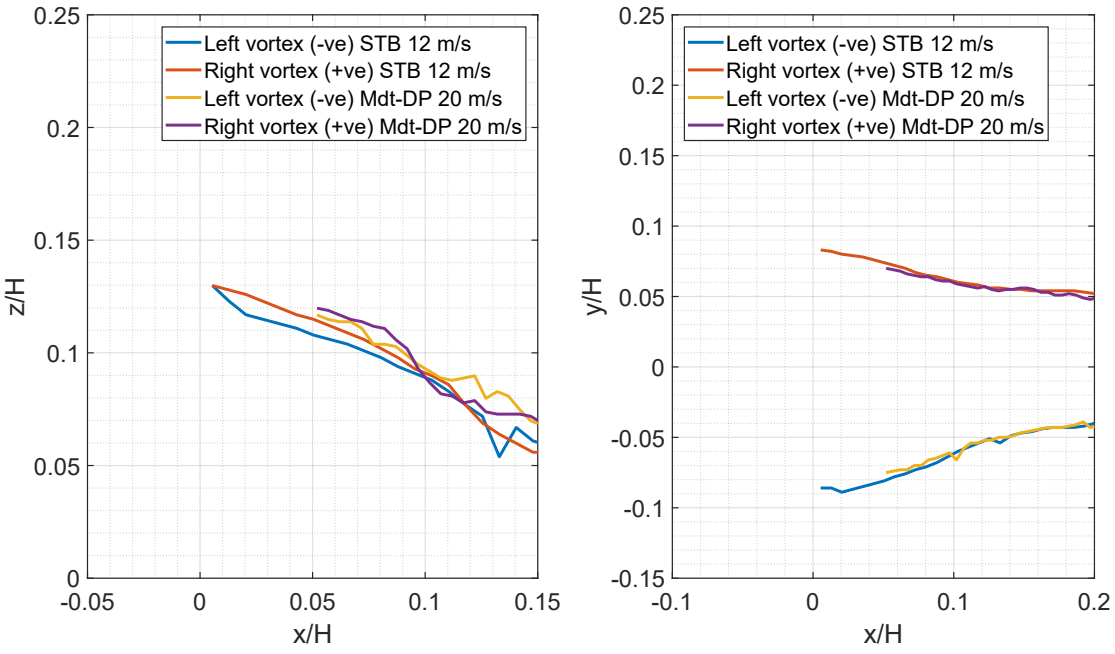

(a) (b)

Figure 5.17: Vortices position measured with the methods: STB (12 m/s) and MΔt-DP (20 m/s). (a) side view (b) top view.

CHAPTER 6

CONCLUSIONS AND RECOMMENDATIONS

In this chapter, the findings produced by the present investigations are briefly summarised, with respect to the performances of the novel strategy. Following, some recommendations are proposed, which aim at suggesting possible future developments concerning both the acquisition and processing strategy and the application of Robotic PIV in general.

6.1 Conclusions

The advent of Robotic volumetric PIV has introduced a possible solution to perform 3D PIV measurement at industrial scales, reaching even cubic meter scales. As shown by Jux (2017), in literature there are several studies in which, in the last decade, repetition of planar or stereoscopic measurements has been used to investigate the flow feature on industrial scales. Jux (2017) indicates two main reasons for the preference for multiple planar measurements w.r.t. standard tomographic PIV: the size of the measurement reachable and the system complexity. As introduced before, the advent of Robotic PIV has made possible to overcome these two limitations of the standard volumetric technique mainly by the alignment of illumination and imaging axes and by the adoption of a robotic manipulation of the measurement probe. However, the compactness of the system is achieved by lowering the tomographic aperture, characteristic that leads to a poor positional accuracy along the coaxial direction. In order to deal with this issue, the standard acquisition technique used in Robotic Volumetric PIV is based on the substantial increment of the time interval along which the particles are followed. This requires the capability of imaging the same particle multiple times while it passes through the measurement volume.

Considering the industrial environment, another specific requirement appears: the flow velocities typically investigated in industry, either automotive or aeronautic, are two or three times higher than the ones resolvable by the state-of-the-art of the Robotic PIV at the beginning of this project. Indeed, if the flow velocity increases, the acquisition frequency has to increase accordingly, in order to image the same particle the required amount of times and be able to apply the smart tracking algorithm STB. For this reason, considering a specific hardware, the maximum resolvable velocity is limited by the maximum acquisition frequency. The straightforward solution is to change the hardware, more specifically the cameras, selecting a solution with higher f_{max}. However, nowadays it has not been possible due to high requirements in terms of the dimension and costs of the system, that has to be compact to allow the robotic manipulation and not too expensive. For this reason, it has been necessary to develop a new acquisition and processing technique that permitted the actual Robotic PIV system to cope with velocities proper of the industrial world.

Taking inspiration from the classical planar PIV, a double-pulse, double-frame technique can be used to increase the velocity range of the Robotic Volumetric PIV. The pulse separation time between two pulses can be really short, with a long time between two subsequent pairs. This strategy permits to measure high-velocity flows, overcoming the frequency limitations that, as mentioned, would appear if a time-resolved strategy is used. The lack of temporal information, however, reduces substantially the velocity dynamic range of the final measurement. Increasing the pulse separation time can be an option to increase the accuracy of a DP-DF strategy, however, if truncation errors are neglected, the maximum Δt usable is limited by the appearance of pairing errors. Analysing the success pairing percentage, it can be stated that the wrong pairing error starts to corrupt the measurement for $\Delta x/\overline{r} > 0.3$.

To enlarge the measured particle displacement, the technique described in Chapter 3 has been designed and implemented. The proposed approach, abbreviated Mdt-DP, relies on the acquisition of two datasets with increasing Δt. The results obtained with the short pulse separation time are used as the predictor for the pairing phase for the data acquired with a longer Δt. The usage of a

predictor guarantees an acceptable percentage of correct pairing for all the pulse separation times considered in the performed analysis.

To assess the performances of both the mentioned methods, DP-DF and Mdt-DP, the near wake of a 50% replica of the Ahmed body has been investigated. Firstly, a free-stream velocity of 12 m/s has been selected in order to be able to performed time-resolved measurements and analyse them with the state-of-the-art technique, STB. The results show that both DP-DF and Mdt-DP manages to detect the main flow feature, such as the position of the C-pillar vortices and recirculation bubble behind the base of the body. As expected, the lack of temporal information decreases the accuracy of the measurements, reducing the DVR of, respectively, two and four times compared the one characteristic of the time-resolved measurement. The lower accuracy affects mainly the coaxial direction, leading to an underestimation of the correspondent velocity component. If the vorticity fields obtained by DP-DF and Mdt-Dp are compared, it is noticeable that the latter produces cleaner results thanks to the longer final pulse separation time. Judging the results obtained by the two different methods, as expected, the Mdt-DP has proven to increase the accuracy of the results w.r.t. DP-DF, but still to be far from the accuracy level of the state-of-the-art strategy, time-resolved data coupled with STB. However, this result is obtained at the cost of a higher complexity and experiment time. Indeed, to use the Mdt-DP strategy, for each position of the velocimetry probe, two consecutive measurements with increasing Δt have to be performed, doubling the total acquiring time.

The ability of the proposed method of fulfilling the thesis objective:

> *"evaluate the feasibility and design a method to increase the velocity range of application of a Robotic PIV system"*

is demonstrated through a study of the near wake of the Ahmed body at 20.0 m/s, a velocity at which the standard acquisition and processing strategy cannot be used. The results, evaluated in terms of vorticity and velocity fields, prove the capability of the proposed strategy to detect and measure the main flow filed features, permitting the usage of the Robotic PIV system at the considered velocity.

Considering the results obtained, for the actual state of the hardware, a possible criterion to select the appropriate acquiring and processing strategy can be outlined. For measurement with $U_\infty < 15$ m/s, the acquisition of time-resolved data with the subsequent application of the tracking technique STB is suggested. For higher free-stream velocities, it is possible to apply both DP-DF and Mdt-DP strategies, with the latter that guarantees a higher accuracy at the cost of a longer acquisition time.

6.2 Recommendations

Even if the method proposed has demonstrated the ability to extend the velocity range that the Robotic PIV setup can cope with, several future developments can be thought of. Firstly, the results reported in Chapter 5 highlight the limitations of the choice of determination of the two different pulse separation times Δt_{short} and Δt_{long} based on global assumptions. As demonstrated in Chapter 3, if truncation errors are neglected, the choice of the different pulse separation times is

influenced by different factors, such as flow speed, consequently particle displacement, and particle concentration. Since both the factor mentioned are strongly varying locally, an approach that considers local characteristic could increase furthermore the DVR achievable.

One of the main disadvantages of the proposed technique is the necessity of doubling the time of measurement, due to the two different pulse separation times that have to be acquired. In order to avoid the need of performing multiple measurements, specific pulsing strategies can be thought of. For example, considering a double-frame approach, three pulses can be used to replicate the Mdt-DP method with only one acquisition. Following this idea, the first pulse would be inserted at the end of the first frame, with the second pulse at the very beginning of the second frame. Always on the second frame, the last pulse would be shot at the end of the aperture time. In this way, the particle would be illuminated three times, once in the first frame and twice in the second one. Due to the really short distance in time between the first and the second pulses, the pairing could not be affected by the presence of the third pulse under specific circumstances, such as a significant separation in time between the second and the third pulses and an appropriate seeding concentration. Indeed, in the second frame, the imaged particle concentration is doubled. Furthermore, since the first and the second pulses are imaged in different frames, the direction ambiguity is avoided. Thus, a stretching of the pulse separation time would be achieved performing only one acquisition. Finally, a second-order fitting of the particle position and velocity would be possible as the information from three instants would be available.

All the analyses done in the present work have been performed neglecting the truncation error. In order to quantify the effect of the predictor on the final results in the presence of accelerated flow correctly, a proper study is encouraged.

Another possible improvement regards the binning process. Even if compared to the previous works done with data obtained by Robotic Volumetric PIV, Gaussian weighting has been introduced, a further step forward can be done. As suggested by Agüera et al. (2016), a polynomial fitting would increase the accuracy of the final result, also enhancing the final spatial resolution.

BIBLIOGRAPHY

Adrian, R. J. (1984). "Scattering particle characteristics and their effect on pulsed laser measurements of fluid flow: speckle velocimetry vs particle image velocimetry". In: *Applied Optics* 23.11, p. 1690.

— (1991). "Particle-Imaging Techniques for Experimental Fluid Mechanics". In: *Annual Review of Fluid Mechanics* 23.1, pp. 261–304.

— (1997). "Dynamic ranges of velocity and spatial resolution of particle image velocimetry". In: *Measurement Science and Technology* 8.12, pp. 1393–1398.

— (2005). "Twenty years of particle image velocimetry". In: *Experiments in Fluids* 39.2, pp. 159–169.

Agüera, N. et al. (2016). "Ensemble 3D PTV for high resolution turbulent statistics". In: *Measurement Science and Technology* 27.12, p. 124011.

Ahmed, S.R., G. Ramm, and G. Faltin (1984). "Some salient features of the time-averaged ground vehicle wake". In: *SAE Technical paper* 840300.

Boillot, A. and A. K. Prasad (1996). "Optimization procedure for pulse separation in cross-correlation PIV". In: *Experiments in Fluids* 21.2, pp. 87–93.

Brücker, C. (1995). "Digital-Particle-Image-Velocimetry (DPIV) in a scanning light-sheet: 3D starting flow around a short cylinder". In: *Experiments in Fluids* 19.4, pp. 255–263.

Cardano, D., G. Carlino, and A. Cogotti (2008). "PIV in the Car Industry: State-of-the-Art and Future Perspectives". In: *Particle Image Velocimetry*. Vol. 112. Berlin, Heidelberg: Springer Berlin Heidelberg, pp. 363–376.

Caridi, G. C. A. et al. (2016). "HFSB-seeding for large-scale tomographic PIV in wind tunnels". In: *Experiments in Fluids* 57.12.

Caridi, G. C. A., A. Sciacchitano, and F. Scarano (2017). "Helium-filled soap bubbles for vortex core velocimetry". In: *Experiments in Fluids* 58.9.

Cornic, P. et al. (2014). “Tomo-PTV with sparse tomographic reconstruction and optical flow”. In:

Elsinga, G. E. et al. (2006). “Tomographic particle image velocimetry”. In: *Experiments in Fluids* 41.6, pp. 933–947.

Fincham, A. and G. Delerce (2000). “Advanced optimization of correlation imaging velocimetry algorithms”. In: *Experiments in Fluids* 29.7, S013–S022.

Giaquinta, D. (2018). “The Flow Topology of the Ahmed Body in Cross-Wind”. Master thesis. TU Delft.

Hain, R. and C. J. Kähler (2007). “Fundamentals of multiframe particle image velocimetry (PIV)”. In: *Experiments in Fluids* 42.4, pp. 575–587.

Issakhanian, E. et al. (2010). “An Experimental Study of the Flow Around a Formula One Racing Car Tire”. In: *Journal of Fluids Engineering* 132.7, p. 071103. ISSN: 00982202.

Jux, C. (2017). “Robotic Volumetric Particle Tracking Velocimetry by Coaxial Imaging and Illumination”. Master thesis. TU Delft.

Katz, J. (1986). “Aerodynamic Model for Wing-Generated Down Force on Open-Wheel-Racing-Car Configurations”. In:

— (1995). *Race car aerodynamics: designing for speed*. Cambridge, MA, USA: R. Bentley. 270 pp.

Kähler, C. J., S. Scharnowski, and C. Cierpka (2012). “On the resolution limit of digital particle image velocimetry”. In: *Experiments in Fluids* 52.6, pp. 1629–1639.

Lignarolo, L.E.M. et al. (2014). “Experimental analysis of the wake of a horizontal-axis wind-turbine model”. In: *Renewable Energy* 70, pp. 31–46.

Lourenco, L. M., S. P. Gogineni, and R. T. LaSalle (1994). “On-line particle-image velocimeter: an integrated approach”. In: *Applied Optics* 33.13, p. 2465.

Lynch, K. and F. Scarano (2013). “A high-order time-accurate interrogation method for time-resolved PIV”. In: *Measurement Science and Technology* 24.3, p. 035305.

— (2014). “Material acceleration estimation by four-pulse tomo-PIV”. In: *Measurement Science and Technology* 25.8, p. 084005. ISSN: 0957-0233, 1361-6501.

Maas, H. G., A. Gruen, and D. Papantoniou (1993). “Particle tracking velocimetry in three-dimensional flows: Part 1. Photogrammetric determination of particle coordinates”. In: *Experiments in Fluids* 15.2, pp. 133–146.

Meinhart, C. D., S. T. Wereley, and J. G. Santiago (2000). "A PIV Algorithm for Estimating Time-Averaged Velocity Fields". In: *Journal of Fluids Engineering* 122.2, p. 285.

Novara, M. et al. (2016). "Lagrangian 3D particle tracking in high-speed flows: Shake-The-Box for multi-pulse systems". In: *Experiments in Fluids* 57.8.

Pereira, F. et al. (2006). "Two-frame 3D particle tracking". In: *Measurement Science and Technology* 17.7, pp. 1680–1692.

Persoons, T. (2015). "Time-Resolved High-Dynamic-Range Particle Image Velocimetry Using Local Uncertainty Estimation". In: *AIAA Journal* 53.8, pp. 2164–2173.

Persoons, T. and T. S. O'Donovan (2010). "High Dynamic Velocity Range Particle Image Velocimetry Using Multiple Pulse Separation Imaging". In: *Sensors* 11.1, pp. 1–18.

Raffel, M. (2007). *Particle Image Velocimetry*. Experimental Fluid Mechanics. Berlin, Heidelberg: Springer Berlin Heidelberg. DOI: 10.1007/978-3-540-72308-0.

Scarano, F. (2013). "Tomographic PIV: principles and practice". In: *Measurement Science and Technology* 24.1, p. 012001.

Scarano, F., K. Bryon, and D. Violato (2010). "Time-resolved analysis of circular and chevron jets transition by TOMO-PIV". In:

Scarano, F. et al. (2015). "On the use of helium-filled soap bubbles for large-scale tomographic PIV in wind tunnel experiments". In: *Experiments in Fluids* 56.2.

Schanz, D., S. Gesemann, and A. Schröder (2016). "Shake-The-Box: Lagrangian particle tracking at high particle image densities". In: *Experiments in Fluids* 57.5.

Schneiders, J. F. G. and A. Sciacchitano (2017). "Track benchmarking method for uncertainty quantification of particle tracking velocimetry interpolations". In: *Measurement Science and Technology* 28.6, p. 065302.

Schneiders, J.F.G. (2017). *Bridging PIV spatial and temporal resolution using governing equations and development of the coaxial volumetric velocimeter*. Delft University of Technology, pp. –.

Schröder, A. et al. (2015). "Advances of PIV and 4D-PTV "Shake-The-Box" for Turbulent Flow Analysis –the Flow over Periodic Hills". In: *Flow, Turbulence and Combustion* 95.2, pp. 193–209.

Schroder, A. et al. (2013). "Dual-volume and four-pulse tomo-PIV using polarized light". In:

Sciacchitano, A. (2014). "Uncertainty quantification in particle image velocimetry and advances in time-resolved image and data analysis." PhD thesis. S.l.: [s.n.]

Sciacchitano, A. and F. Scarano (2014). “Elimination of PIV light reflections via a temporal high pass filter”. In: *Measurement Science and Technology* 25.8, p. 084009.

Sciacchitano, A. and B. Wieneke (2016). “PIV uncertainty propagation”. In: *Measurement Science and Technology* 27.8, p. 084006.

Sciacchitano, A., F. Scarano, and B. Wieneke (2012). “Multi-frame pyramid correlation for time-resolved PIV”. In: *Experiments in Fluids* 53.4, pp. 1087–1105.

Soloff, S. M., R. J. Adrian, and Z. C. Liu (1997). “Distortion compensation for generalized stereoscopic particle image velocimetry”. In: *Measurement Science and Technology* 8.12, pp. 1441–1454.

Spoelstra, A., W. Terra, and A. Sciacchitano (2018). “The Ring of Fire for in-Field Sport Aerodynamic Investigation”. In: *Proceedings* 2.6.

Westerweel, Jerry (1993). “Analysis of PIV interrogation with low-pixel resolution”. In: ed. by S. S. Cha and J. D. Trolinger, pp. 624–635.

Wieneke, B. (2008). “Volume self-calibration for 3D particle image velocimetry”. In: *Experiments in Fluids* 45.4, pp. 549–556.

— (2013). “Iterative reconstruction of volumetric particle distribution”. In: *Measurement Science and Technology* 24.2, p. 024008.

Willert, C. E. and M. Gharib (1991). “Digital particle image velocimetry”. In: *Experiments in Fluids* 10.4, pp. 181–193.

Wright, P.G. (1982). “The influence of aerodynamics on the design of Formula One racing cars”. In: *Vehicle Design* 3.4, pp. 383 –397.

Zhang, X. and J. Zerihan (2003a). “Aerodynamics of a Double-Element Wing in Ground Effect”. In: *AIAA Journal* 41.6, pp. 1007–1016.

— (2003b). “Off-Surface Aerodynamic Measurements of a Wing in Ground Effect”. In: *Journal of Aircraft* 40.4, pp. 716–725.

— (2004). “Edge Vortices of a Double Element Wing in Ground Effect”. In: *Journal of Aircraft* 41.5, pp. 1127–1137.

Zhang, X., A. Senior, and A. Ruhrmann (2004). “Vortices behind a bluff body with an upswept aft section in ground effect”. In: *International Journal of Heat and Fluid Flow* 25.1, pp. 1–9.

Zhang, X., W. Toet, and J. Zerihan (2006). “Ground Effect Aerodynamics of Race Cars”. In: *Applied Mechanics Reviews* 59.1, p. 33.